Università degli Studi dell'Insubria

Dipartimento di Scienza e Alta Tecnologia - Como

MASTER DEGREE IN PHYSICS

A novel dose delivery system for cell irradiations with conventional and FLASH dose rates at the Bern medical cyclotron

TUTORS
Prof. Saverio Braccini
AEC-LHEP, University of Bern

Prof. Michela Prest
Università degli Studi dell'Insubria

AUTHOR
Maria Vittoria Rossi

COTUTOR
Dr. Eva Marie Kasanda
Postdoctoral Researcher
University of Bern

Academic Year 2022-2023

We must believe that we are gifted for something,
and that this thing, at whatever cost, must be attained.
Maria Skłodowska Curie

A Cristina, Mario e Santi

Contents

Introduction

Radiation therapy stands as a primary approach for controlling, curing, and providing palliative care for cancer. This therapeutic technique is used for about half of the patients diagnosed with cancer.

In the last two decades, there have been significant developments and innovations in the field of radiation therapy aimed at enhancing the effectiveness of the radiation treatment of the tumor target while minimizing damage to non-malignant tissues.

One such case is the diffusion of hadron therapy, which uses accelerated protons or ions to perform external beam radiation therapy treatments. The advantage in using heavy charged particles lies in the particular shape of the depth dose distribution. In comparison to the more commonly used electrons and photons, protons and ions deliver a minimal almost constant quantity of energy at the body surface, and then, near the end of their range, they release most of their energy. By adjusting the position of this peak of energy deposit, called the "Bragg peak", it is possible to precisely target the tumor for treatment.

Another possible significant advancement in minimizing the toxicity of radiation on healthy tissues is the so-called "FLASH effect". Several animal studies have shown that administering an ultra-high dose rate irradiation in an extremely short pulse of less than a second enhances the normal tissue control probability while maintaining the same tumor control level. Although these preliminary results are extremely promising, the transition to FLASH radiation therapy is limited by the need of a real-time dosimeter suitable for this new technique. Additionally, further pre-clinical and clinical studies must be performed to confirm the advantages of FLASH radiation therapy.

Pre-clinical studies are essential to introduce a new technique into clinical use. They are can be performed on a living organism (in-vivo), or on cell cultures (in-vitro).

This master thesis was accomplished in the framework of the SEMP-Erasmus+ Traineeship student exchange program, established between the Laboratory of High Energy Physics (LHEP) at the University of Bern and the

Physics Department (DiSAT) at the University of Insubria. This program allowed me to carry out a six month internship in Bern.

As part of a collaboration between the Medical Applications of Particle Physics group at LHEP and the Institute of Anatomy at the University of Bern, an ongoing project aims at establishing a cell irradiation beamline at the Bern medical cyclotron. In this context, my master thesis focused on novel methodologies for cell irradiation studies in both conventional and FLASH regimes at the Bern medical cyclotron.

A preliminary set of cell irradiations has been performed using conventional dose rates, and future experiments will concentrate on FLASH dose rates. Comparing the resulting cell survival curves will enable the first test of the FLASH effect at this facility. To perform studies at FLASH dose rates, a novel dosimetry system based on a scintillator connected to an optical fiber was tested during this master work.

In the first chapter of this thesis, a brief introduction to radiation therapy is presented, specifically focusing on external beam therapy with photons and protons, underlying the differences between these two techniques. The new approach for cancer therapy, FLASH-RT, is defined, and the main results of pre-clinical studies on the improvements introduced by this technique are presented. The second part of Chapter 1 outlines the reasons for the development of a dosimetry system for both clinical uses and pre-clinical studies, also for FLASH-RT. Additionally, the in-vitro pre-clinical experiment called Clonogenic Cell Survival Assay is briefly described.

The first part of Chapter 2 is dedicated to the Bern Medical Cyclotron facility, describing its Beam Transfer Line and the requirements to adapt it for pre-clinical in-vitro studies. The second part of the chapter is dedicated to the final setup developed for cell irradiations at conventional and FLASH dose rates, along with the steps taken to optimize the beamline for this purpose.

Chapter 3 describes the development of a dose and dose rate readout system for cell irradiations at our facility. To this end, Gafchromic EBT-3 and HD-V2 films were calibrated at different external facilities using several radiation sources, following the procedures outlined at the beginning of this chapter. In the second half of the chapter, the procedure to characterize the dose rate, delivered by the proton beam with the optimized setup, using a ionization chamber is detailed. At higher dose rates, the novel dosimeter based on a scintillating fiber was also tested.

The last chapter is dedicated to the experimental results, beginning with the assessment of the final uniformity of the beam coming out from the optimized setup. Then, the curves obtained from the calibrations of Gafchromic films are presented, along with the conversion of pixel values to dose. The lin-

earity of the ionization chamber and the scintillating fiber detector with the dose rate is discussed for all the experiments. A series of improvements and experiments to be performed in the future to complete the characterization of the scintillating fibers are suggested. The procedure for cell irradiation using this novel setup, the outcomes of the first preliminary tests, and a cell survival curve derived from these results are also illustrated.

Chapter 1

Cancer radiation therapy

Cancer is a condition in which cells within a particular region of the body undergo uncontrolled growth and replication, giving rise to tumors that impact nearby tissues and organs and can extend to other areas of the body. In Italy, in the year 2023, 395,000 new cancer diagnoses were estimated [1]. With respect to the year 2020, the increase is of over 18 thousand diagnoses. Typical methods for treating cancer include surgery, radiation therapy, chemotherapy and hormone therapy [2].

Radiation therapy (RT) is a cancer treatment technique capable of inducing necrosis, leading to the death of tumor cells, through the use of high-energy radiation known as ionizing radiation. The term ionizing radiation refers to electromagnetic waves or particles that have enough energy to remove electrons from the atoms of the materials they interact with, causing ionization. Ionization damages cells, either through direct harm to the DNA by breaking hydrogen bonds or indirectly by causing cell death through the generation of free radicals. This damage affects both malignant and non-malignant cells; therefore, the main goal of research in radiation therapy is to maximize the dose deposited in the target tumor while shielding healthy tissues from the effects of radiation itself.

There are several different types of ionizing radiation that can be used for radiation therapy. The most common modality is based on high-energy photons, but charged particles such as electrons, protons, and heavy ions are also employed clinically [3]. RT can be used alone for treating localized tumors and tumor types that are sensitive to radiation, but also as a palliative cure to alleviate symptoms caused by cancer [4].

This technique may be used prior to, during, or following surgery, together with other treatment modalities such as chemotherapy or immunotherapy [5]. If employed after surgery, RT can be used as an adjuvant treatment, especially when the resection is not complete [4].

Radiation treatment is recommended as an integral part of the treatment for more than 50-60% of cancer patients [5].

Radiation therapy can be divided in three main branches [4]:

- Targeted Radionuclide Therapy (TRT)

- Internal Radiation Therapy (IRT);

- External Beam Radiation Therapy (EBRT).

Targeted Radionuclide Therapy is performed with the injection of radioactive substances that specifically target tumor cells, reducing the side effects to the healthy tissues. These substances, called radiopharmaceuticals, are composed of a radionuclide, that can be produced in a medical cyclotron, eventually bound with other biological molecules able to target specific organs [6].

Internal Radiation Therapy or Brachytherapy refers to treatments in which the source of radiation is internal to the body. The radioactive sources are enclosed in catheters or seeds and target directly the tumor site [7]. With this solution a high radiation dose can be delivered locally to the disease.

The most common method for clinical radiation treatment is EBRT that uses a machine external to the body to produce a focused high-energy beam of ionizing radiation. The beam is centered in the area to be treated and can be shaped according to the size and geometry of the target tumor.

Several sophisticated EBRT techniques have been developed over the years, including Intensity-Modulated Radiation Therapy (IMRT), Image-guided radiotherapy (IGRT), and Stereotactic Body Radiation Therapy (SBRT) [5]. EBRT can be delivered using different types of radiation, from photons and electrons to protons in the case of the hadron therapy.

1.1 Radiation therapy with photons and protons

Conventional EBRT was implemented in the clinical practice shortly after the discovery of X-rays by Roentgen in 1895 [3]. The mechanism of photon absorption in the patient body results in the highest dose being delivered near the surface, followed by an exponential decrease in dose as a function of the tissue depth, as shown in Figure 1.1. The three main modes of photon interaction with matter are the photoelectric effect, the Compton effect, and pair production.

Protons were first used in clinical treatment in 1954 at the Lawrence Berkeley Laboratory [8], following Wilson's suggestion of their use in cancer therapy due to their specific dose profile. Over the last few decades, hadron therapy has become more popular as a radiation therapy method, thanks to its advantages in terms of dose distribution when compared to conventional radiation therapy.

First of all, photons suffer scattering that causes the deposit of the dose far from the trajectory of the beam. On the other hand protons, because of their mass, when colliding with other particles experience a smaller deflection with respect to photons, proceeding in an almost linear path. This allows to define very precise treatment plans.

Moreover protons, being charged particles, mainly lose energy via Coulomb interactions with atomic nuclei [3], which results in different dose distributions in matter.

In fact for protons (red curve in Figure 1.1), the energy deposit is minimal and quasi constant in the superficial layers of the body. As protons decelerate along their path, the probability of interaction with matter increases. This leads to a sharp, non-linear rise in dose deposit as protons approach the end of their trajectory. This region of high dose deposit, known as the Bragg peak, is the one where the stopping power, describing the particle energy loss per unit length, is at its maximum. After reaching the Bragg peak, the particles come to a complete stop.
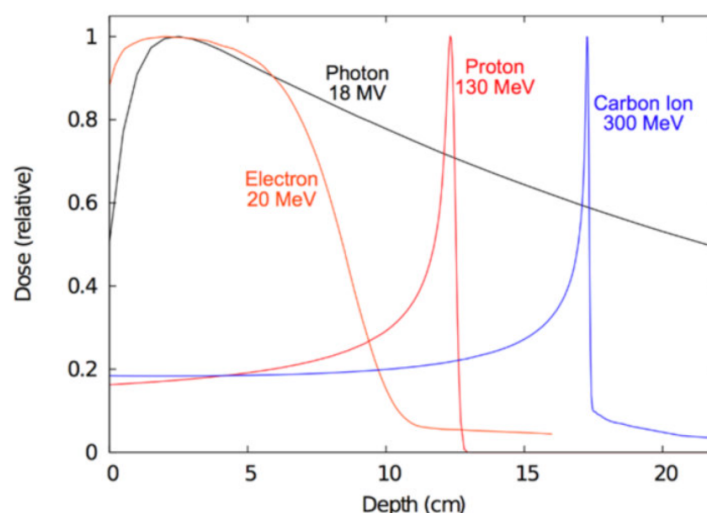
Figure 1.1: Depth dose distributions of the main radiations employed in cancer therapy [9].

Shaping the treatment beam such that the Bragg Peak overlaps with the

treatment volume ensures that the vast majority of the delivered dose is deposited in the target tissue. The position of the Bragg peak depends on the energy; a more energetic proton beam will penetrate deeply in the tissues.

The Bragg peak of a mono-energetic proton beam is not large enough to cover the whole tumor; in the range 60-200 MeV the typical width of the peak is around 3 to 20 mm [10]. For this reason, hadron therapy employs a broadened beam that can be achieved by expanding the range of used energies, enabling the treatment of a broader range of depths. The resulting dose distribution is referred to as Spread Out Bragg Peak (SOBP).

In Figure 1.2, a comparison of different treatment plans with proton and photon Intensity-Modulated Radiation Therapy (IMRT) is presented [11]. In the case of protons, the entrance dose is lower than photons, and since the beam is completely stopped inside the patient, the dose deposited following the Bragg Peak is typically negligible. In comparison, photons deposit a larger dose all over the treated slice of the body. In the image on the right it is possible to see the excess of dose delivered using a photon beam instead of protons; in this specific case, 50% more dose was absorbed by the patient in the photon treatment.
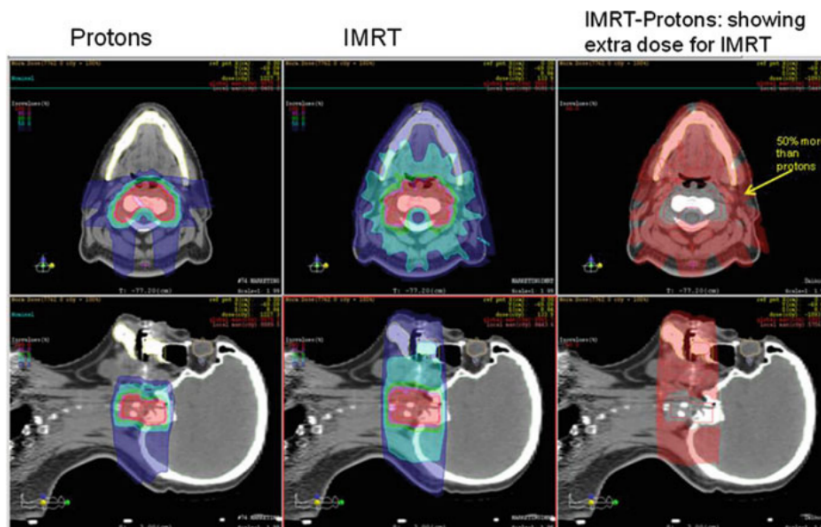
Figure 1.2: Dose distributions for a treatment plan with protons (left) and IMRT using photons (center) [11]. The right panel highlights the excess of dose that is delivered using photons instead of protons.

Due to its localized dose deposit, hadron therapy features a significant reduction in the radiation dose reaching the surrounding healthy tissue by 50–70% while delivering an equivalent dose to the tumor target volume as conventional RT [12].

Protons and photons have a similar biological effectiveness, that represent the number of ionized biomolecules produced by the ionizing radiation per unit dose. The Relative Biological Effectiveness index (RBE) is evaluated to be 1.1 for protons and 1 for photons [11]. However, this factor is influenced by the Linear Energy Transfer (LET) that is the amount of energy absorbed per unit length by the matter crossed by a ionizing particle. This factor determines the damage caused by radiation.

Protons are classified as high LET particles, thus they cause more harm in a biological system than radiations with a lower LET like photons. The region of maximum LET for protons corresponds to the Bragg peak; therefore, in the target area corresponding to the peak, the biological effectiveness of the particles is at its maximum [8].

Despite these important qualities, the diffusion of hadron therapy is still limited by the costs of a proton therapy facility [11]. In March 2023, the operational proton radiotherapy centers were 106 globally, while the conventional X-ray radiotherapy centers worldwide were over 8,000 [12]. As a consequence, proton therapy is received by less than 1% of patients undergoing radiotherapy, despite conservative estimates indicating that 15–50% of these patients could potentially benefit from it [12].

In EBRT applications the photon beam is usually produced by a linear accelerator (linac) while hadron therapy is based on the use of circular accelerators like a cyclotron [13].
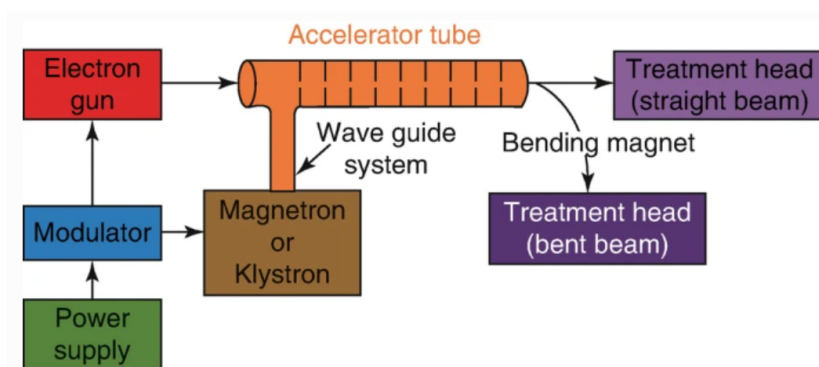
Figure 1.3: Scheme of a typical clinical linac [14]. The electron gun produces the electrons that are accelerated via electromagnetic waves generated by a klystron or a magnetron.

A scheme of a linac accelerator is presented in Figure 1.3 [14].

The clinical linac produces high energy electrons or photons with typical energies in the range 5-25 MeV. Electrons are accelerated in a vacuum tube by high-frequency electromagnetic waves. The accelerated electron beam can

then be used directly to treat the patient (especially for superficial tumors) or focused on a target to produce high energy photons for deep-seated tumors. The production of photons is caused by the Bremsstrahlung phenomenon. Before reaching the body of the patient, the beam is shaped using collimators that replicate the geometry of the tumor.

The linac is calibrated to deliver a precise and uniform dose to the patient, that must be known with high accuracy. The precision of the linac in delivering a known dose was exploited in this project using the Bern University Hospital (Inselspital) clinical linac to calibrate Gafchromic EBT-3 films. A picture of this machine and of a typical treatment room is shown in Figure 1.4.
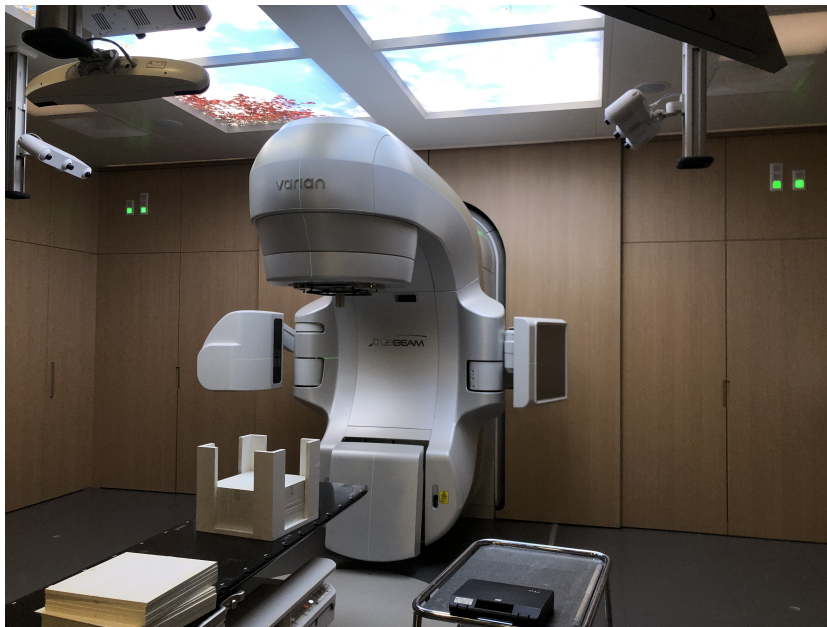
Figure 1.4: Photograph of the clinical linac of the Radiation Oncology department of the Bern University Hospital. The accelerator was used in this project to calibrate Gafchromic EBT-3 films with photons (Section 3.1.2).

In a cyclotron, the ions are produced by an ion source at the center of the machine and are accelerated by a high frequency electric field generated by specific electrodes called dees. A high magnetic field is present inside the machine and forces the particles to move on a circular trajectory. The acceleration causes the particle energy to increase while their rotational frequency stays constant. Therefore the diameter of the particles orbit increases each round till they can be extracted from the machine. For applications in hadron therapy, the protons produced by the cyclotron must have an energy

in the 70-250 MeV range.

A scheme of the cyclotron structure is depicted in Figure 1.5 [15].
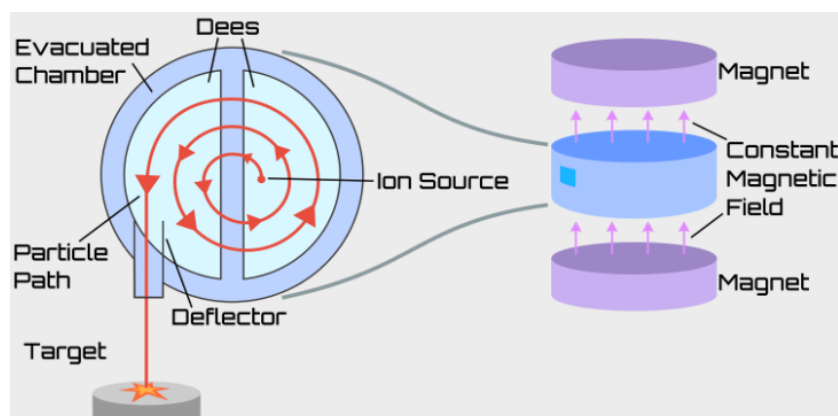
Figure 1.5: Scheme of a cyclotron [15]. Charged particles generated by the ion source undergo acceleration through an oscillating electric field applied to the dees. A constant magnetic field causes the particle to follow a circular path, and with each round, the diameter of the path increases until the particles can be extracted and focused on a target.

The cost of a single-room treatment unit for hadron therapy ranges from 30 to 50 million dollars, while conventional photons systems have typically a cost of approximately 6 million dollars [12]. However, when comparing the costs of proton therapy to photon therapy, it is important to evaluate the savings resulting from the reduced irradiation of healthy tissues in hadron therapy.

The decrease in the dose deposit in normal tissues is expected to decrease the need for medical treatments addressing side effects and lower the risk of developing secondary malignancies and the need to treat radiation induced cancers. Furthermore, cyclotrons have a considerably longer lifespan (30-50 years) compared to a linear accelerator (10 years) and enable the treatment of a significantly higher number of patients per day compared to a single linac [11].

In conclusion, proton therapy represents a promising frontier in cancer treatment. Its unique ability to deliver precise doses of radiation to tumor tissues while minimizing the damage to surrounding healthy cells makes it a valuable option in the fight against cancer.

In this thesis project, pre-clinical studies were performed using a 18 MeV proton beam. In our facility, the beam was produced using a medical cyclotron employed daily for radioisotope production; the accelerator is briefly described in Chapter 2.

1.2   Conventional and FLASH regimes

Over the past two decades, there have been revolutionary developments in the field of radiation therapy technology. These improvements in research have mainly focused on maximizing the dose deposited in the target volume while shielding healthy tissues.

A novel radiation therapy technique, known as FLASH radiation therapy (FLASH-RT), has been demonstrated to reduce radiation-induced damage in healthy tissues without compromising the anti-tumor effectiveness [16].

This technique consists of a single fast ultra-high dose rate (> 40 Gy/s) delivered in fractions of a second (< 500 ms) [17]. A comparison with the conventional RT in terms of dose rates is presented in Figure 1.6; this last technique uses dose rates in the range 0.01-0.40 Gy/s.
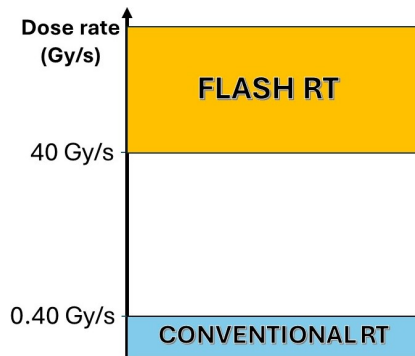
Figure 1.6: Dose rate ranges for conventional and FLASH regimes. The term FLASH identifies dose rates larger than 40 Gy/s.

What emerges from pre-clinical studies with FLASH-RT is that this newer technology expands the therapeutic window, defined as the range of doses between the curves of Normal Tissue Complication Probability (NTCP) and Tumor Control Probability (TCP) [18]. Specifically, it was observed that the effect on tumor tissues is similar between conventional and FLASH therapy, while the FLASH-RT technique demonstrates a reduced toxicity to non-malignant tissues (Figure 1.7).

The mechanism of this phenomenon, called the "FLASH effect", is still unclear, and further investigations are required to fully understand this behavior [16].

The "FLASH effect" was initially reported in 1959 by Dewey and Boag, demonstrating that ultra-high dose-rate irradiation appeared to protect bacteria compared to conventional dose rates [19]. Subsequent experiments with mammalian and hamster cells confirmed this phenomenon [16].
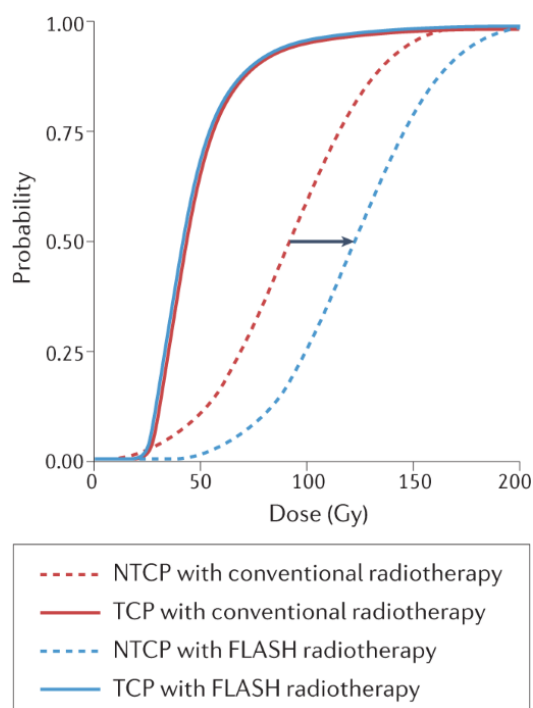
Figure 1.7: Comparison between the normal tissue complication probability (NTCP) and tumor control probability (TCP) curves for conventional and FLASH radiotherapy [18]. FLASH-RT features an increased therapeutic window with a similar TCP but increased NTCP.

In 2014, Favaudon reported that using FLASH-RT for treating lung tumors could result in a complete response and minimize early and late toxicity in normal lung tissues [20]. This groundbreaking finding has sparked significant interest in radiation research. Follow-up studies consistently demonstrated significantly reduced adverse effects in the healthy tissues of mice, mini-pigs, and cats [16].

Finally, in 2018, the first human patient with multiple skin tumors received FLASH-RT using a linac specifically designed to safely accelerate electrons in a "FLASH" mode. The treatment resulted in a rapid, complete and durable tumor response with fewer side effects than expected compared to conventional radiotherapy [21].

Pre-clinical evidence indicates that the administration of radiation through the FLASH technique diminishes the DNA damage in non-malignant tissues. Conversely, this is not observed for malignant tissues that equally react to conventional and FLASH dose rates [18].

In general, previous researches have assessed that FLASH-RT induces local oxygen consumption at a significantly faster rate than tissue oxygenation,

leading to a transient state of hypoxia [18]. The presence of oxygen in tissues is responsible for the formation of free radicals that cause biological damage to tissues. Therefore the state of hypoxia of non-malignant tissues improves the NTCP [16].

Another hypothesis is that the DNA damage sites in FLASH-RT are fewer than conventional RT for non-malignant tissues [16].

In general all the pre-clinical studies demonstrate a different response to radiation of healthy tissues and tumors.

The treatment time of FLASH radiotherapy is significantly reduced compared to conventional radiotherapy (RT); in the first clinical use of this technique, the therapy lasted only 90 ms [16]. The capacity to reduce the time required for FLASH-RT is an additional benefit, allowing for the treatment of a greater number of patients in a day.

The aforementioned results demonstrate that FLASH-RT is a promising technique. However, before this new technique can be implemented in clinical practice, further studies on cells and animals must be performed to investigate the FLASH effect and determine its underlying causes.

Once the results from animal studies are assessed, the same effect must be demonstrated and confirmed in human subjects, taking into consideration the differences between animal models and patients. At this point, the optimal doses required to treat each type of cancer will be redefined for this specific therapy, given the unique characteristics of FLASH-RT [16].

To support the clinical transition to FLASH-RT, it is essential to establish official protocols for dosimetry at FLASH dose rates and define a real-time dosimeter that is reliable for operation in this regime [22]. The absence of real-time in-beam detectors in these preliminary researches can introduce uncertainties on the results [22]. Until now, pre-clinical studies investigating the FLASH effect have only used passive dosimeters [23].

Moreover, research in FLASH radiation therapy is certainly limited by the machines available to deliver this ultra-fast high dose rate radiation beam.

During this thesis project, the Bern medical cyclotron was adapted to deliver FLASH dose rates and a system for ultra short pulses, based on a rotating wheel, was developed (Chapter 2). The aim of this modification was to perform pre-clinical studies on cells at FLASH dose rates with a proton beam.

1.3   Real time dosimetry

The absorbed dose is the most crucial physical parameter influencing the efficacy of radiation therapy. Defined as the energy deposited by ionizing

radiation in a volume per unit mass, it is measured in Gray (Gy).

This quantity must be defined in radiation therapy to examine the effects of radiation on the tumor, ensuring that the patient receives the necessary radiation dose for treatment while minimizing potential health hazards. Additionally, it is crucial to assess the dose delivered by the clinical machine as part of the quality controls.

Dosimetry is the measurement or calculation of the quantity of radiation dose absorbed by matter. The procedures for accurately measuring and calculating this value are outlined in standardized recommendations, such as the TRS 398 IAEA protocol [24].

In conventional radiation therapy the ionization chamber (IC) is considered the standard for absolute and reference dosimetry [25]. It consists of an air-filled cavity with two electrodes: a negative cathode and a positive anode. A voltage applied to the electrodes generates an electric field in the chamber. Ionizing radiations induce ionization in the gas, producing ion-electron pairs, that migrate towards the electrodes because of the electric field. This mechanism generates a current collected by an electrometer, representing the ionization chamber output.

In this project, a parallel plane ionization chamber was used as a reference to monitor the dose rate delivered by our facility. Additionally, a cylindrical Farmer-type ionization chamber was employed to measure the dose delivered by a clinical linac during the calibration of a batch of Gafchromic films.

When moving to the FLASH regime, standard detectors commonly used for conventional RT cannot accurately record signals due to the high dose rates and extremely short irradiation time.

The ionization chamber response is affected by ion recombination effects and cannot be used in FLASH-RT without modification and correction factors [22]. To mitigate ion recombination issues in ionization chambers, the chamber design must be optimized to enhance collection efficiency.

Ultra-thin gap parallel plane chamber prototypes have been tested, illustrating their potential as secondary standard dosimeters for ultra-high dose rate irradiations [26].

Figure 1.8 summarizes the characteristics of several detectors used for dosimetry and beam monitoring [22].

In general, the requirements for a detector suitable for FLASH-RT can be summarized as follows [22]:

- High temporal resolution: the time response of the detector must be fast enough to record the ultra-short pulse;

- Well-known behavior in response to dose;

- Resistance to ultra-high dose rates in terms of saturation;

- Radiation hardness: detectors are integrated into the delivery system and consistently exposed to radiation;

- Transparency to radiation: detectors should not perturb the beam;

- Near tissue equivalence to accurately measure the absorbed dose in tissues;

- High spatial resolution for beam flatness and symmetry measurements;

- Energy independence.

Semiconductors, similarly to ionization chambers, exhibit substantial dose-rate dependency and can suffer radiation damage, making them less optimal for FLASH dosimetry [22].

Thermoluminescent dosimeters (TLDs) and optically stimulated luminescent dosimeters (OSLDs) have been proven to be dose-rate independent up to ultra-high dose rates [22]. However, these detectors are read hours after the irradiation and not in real-time. Real-time beam monitoring systems are highly desirable for quality assurance in FLASH radiotherapy, as well as for assessing beam flatness and symmetry.

In the same way, radiochromic films despite possessing high spatial resolution, being cost-effective, easy to use, and tissue-equivalent cannot be used for real-time measurements.

Calorimeters and Fricke-type dosimeters have demonstrated a dose-rate-independent behavior. However, using these dosimeters is not straightforward and demands sophisticated equipment [22]. A potential solution can be found in portable compact calorimeters that are currently under development.

The Faraday cup measures the total charge of a particle beam and converts the integrated charge into dose. This process requires precise knowledge of the energy spectrum of the beam. Therefore, despite the detector feature of not being affected by the high dose rates, this type of dosimeter requires an independent precise measurement of the beam energy spectrum.

A promising alternative for dosimetry in the FLASH regime is represented by scintillator dosimeters [23]. Scintillation is the property of luminescent materials to emit light when they absorb ionizing radiation [27]. The quantity of light produced by the scintillator is proportional to the dose rate of the incident radiation [23].

Dosimeter	Real time	In vivo dosimetry	Absolute/ reference dosimetry	Beam monitoring	Spatial resolution	Temporal resolution
Ion chamber	Yes	No	Yes	Yes	Several mm	10–200 µs
Semiconductor	Yes	Yes	No	Yes	Sub-mm (or µm)	1–10 ns
TLD	No	Yes	Yes	No	Several mm	N/A
OSLD	No	Yes	Yes	No	Sub-mm to mm	N/A
Scintillator	Yes	Yes	Potentially	Potentially	Sub-mm to mm	ns to µs
Gas scintillator	Yes	No	No	Yes	Sub-mm	N/A
Calorimeter	Yes	No	Yes	No	cm to several mm	ms–10 ms
Film	No	Yes	Potentially	No	Tens of µm	N/A
Fricke	No	No	Yes	No	cm to sub-mm	N/A
Faraday cup	Yes (for charge measurements)	No	Yes	No	N/A	<µs

Figure 1.8: Summary of the characteristics of different types of dosimeters [22]. TLD is the abbreviation for Thermoluminescent Dosimeter and OSLD stands for Optically Stimulated Luminescent Dosimeter.

Optical fibers coupled with scintillating materials have proven to be suitable for applications in radiation therapy dosimetry [28]. Scintillators demonstrate energy and dose rate independence in conventional dose rates, as well as real-time dose assessment capabilities [23]. They can be produced in small sizes, ensuring high spatial resolution and minimizing perturbation to the radiation field [23]. Because of their compact size, they are compatible for in-vivo dosimetry [28].

Recent studies have demonstrated the linearity well above the conventional regime of a novel detector based on a scintillator connected to an optical fiber [29], [30].

Two versions of this novel dosimeter for FLASH-RT, one based on an inorganic scintillator and the other on an organic scintillator, were tested at our facility as part of this work.

1.4 Cell irradiations and the survival curve

Pre-clinical studies are essential to assess the feasibility of the introduction of new radiation therapy techniques into the clinical use. These studies can either be "in-vitro", referring to studies outside of a living organism involving cell cultures, or "in-vivo" for studies performed within the organism. For

pre-clinical stages, only animals can be used "in-vivo".

For in-vitro radiation therapy studies, cells from humans or animals are seeded onto a container and exposed to radiation. The impact of radiation on the cells is quantified through a survival curve, which assesses the cells capacity to maintain reproductive integrity and form colonies after irradiation. This clonogenic assay is a valuable and widely used tool for predicting the efficacy of a particular therapy.

The survival curve describes the relationship between the dose of radiation absorbed by a group of cells and the fraction of cells that survive to form colonies. The test aims at assessing the reproductive cell death following irradiation for both normal and tumor cells; the success of a radiation therapy treatment lies in eradicating cancer cells while minimizing damage to normal cells.

Variations in the survival curve can be observed if the irradiation is performed under different conditions, such as using different types of radiation or altering the environment, including the introduction or removal of oxygen.

In the Clonogenic Cell Survival Assay, live cells are extracted from various species and cultured in flasks. Some containers serve as control samples and remain un-irradiated, while others are exposed to different doses of radiation [31]. Following irradiation, both the irradiated cells and the control ones are released from the flask, counted, and a known number of cells are plated onto a Petri dish. Careful consideration is given to seeding in a uniform and sparsely distributed manner to prevent the overlap of colonies during growth. The Petri dishes are then incubated under appropriate environmental conditions for some time to allow surviving cells to grow into colonies. After incubation, cells are fixed and stained for counting. Each colony is assumed to originate from a single cell and is clearly visible to the naked eye.

A scheme of the procedure described for the Clonogenic Cell Assay is depicted in Figure 1.9.

By counting the number of colonies formed for control and irradiated cells it is possible to determine the plating efficiency (PE) and the survival fraction (SF) that are defined by the following equations:

$$PE = \frac{\text{nr. of colonies formed for un-irradiated cells}}{\text{nr. of seeded cells}} \tag{1.1}$$

$$SF = \frac{\text{nr. of colonies formed after irradiation}}{\text{nr of seeded cells} \cdot \dfrac{PE}{100}} \tag{1.2}$$
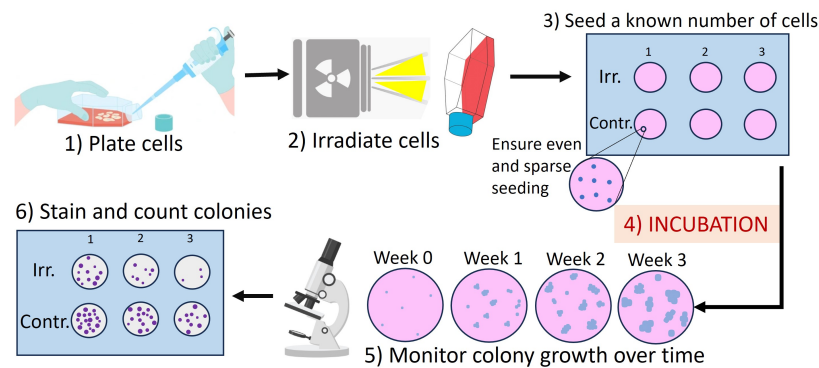
Figure 1.9: Summary of a typical protocol for the Clonogenic Cells Survival Assay. The cells are seeded, treated, incubated for a fixed period of time and then counted [31].

In order to build the cell survival curve, the survival fraction of the various irradiated cells is plotted against the treatment dose. An example of a plot of the survival fraction as a function of increasing doses of radiation is shown in Figure 1.10.
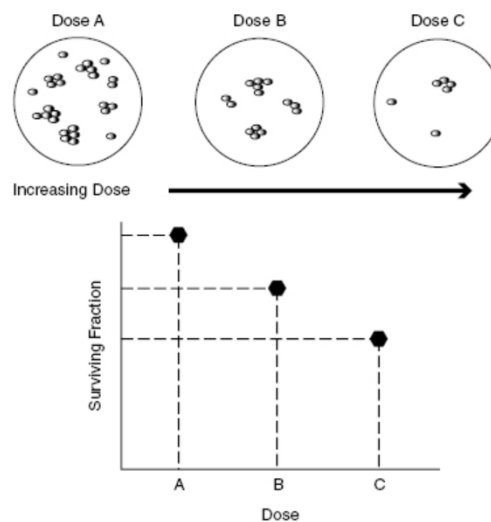
Figure 1.10: Example of a survival curve.

A survival curve extracted from the experimental results of the Clonogenic Cell Survival Assay performed at our facility during this thesis project is presented in Chapter 4.

Chapter 2

Apparatus for cell irradiations at the Bern medical cyclotron

The Bern medical cyclotron, situated in SWAN-Haus [32] at the Bern University Hospital (Inselspital), is regularly used for the production of Positron Emission Tomography (PET) radionuclides. Thanks to a dedicated beamline, the cyclotron is concurrently used for multi-disciplinary scientific activities. The facility is briefly described in the first part of this chapter.

To design and characterize an apparatus suitable for pre-clinical proton therapy cell irradiations, stringent requirements regarding the beam delivery must be met. In the second part of the chapter, the optimization process for the uniformity of the beam and the alignment of the beamline will be discussed.

2.1 The Bern medical cyclotron and its Beam Transfer Line (BTL)

The Bern cyclotron laboratory comprises an underground section that accommodates the cyclotron, the beamline, and a physics laboratory, as well as an elevated level hosting three GMP (Good Manufacturing Practice) laboratories focused on radiotracer production. The University of Bern AEC-LHEP (Albert Einstein Center for Fundamental Physics - Laboratory of High Energy Physics [33]) group, specializing in the medical applications of particle physics (MAPP), is actively involved in research across various fields. Some examples include particle detectors [30], radiation hardness [34], new radioisotopes for medical applications [35] and recently radiation biology.
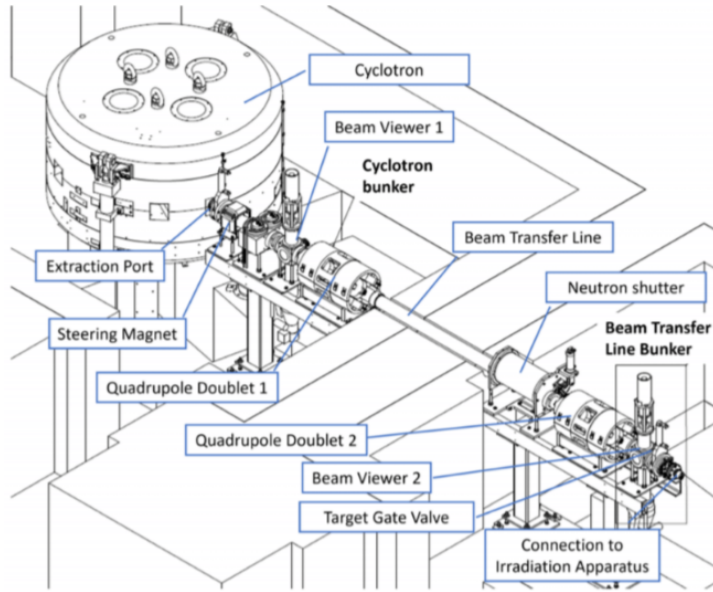
Figure 2.1: Sketch of the Bern medical cyclotron and its BTL. The main elements of the facility are highlighted [36].

Two adjacent bunkers, one housing the cyclotron (referred to as the cyclotron bunker) and the other housing the apparatus for research activities (referred to as BTL bunker) are connected via the Beam Transfer Line (BTL). The BTL extends through a 1.8 m concrete wall and the two rooms can be accessed independently. An additional movable cylindrical neutron shutter is located inside the beam pipe when the BTL is not in use to shield the BTL bunker from the neutron field generated around the cyclotron during the radioisotope production.
A schematic view of the facility is shown in Figure 2.1.

The Bern medical cyclotron, shown in Figure 2.2, is a Cyclone 18/18 HC manufactured by Ion Beam Applications (IBA). The main technical characteristics presented in this chapter are summarized in Table 2.1 [36].

The cyclotron is equipped with two H^- ion sources, ensuring the efficiency of daily radioisotope production in the event of a failure of one of the two sources. The cyclotron is able to provide beam currents of up to 150 µA to its target ports for radioisotope production. The average magnetic field is 1.4 T and the cyclotron frequency is 21 MHz.

Since the machine is outfitted with two dee electrodes, only the radiofrequencies (RF) that represent even harmonics of the cyclotron frequency result in acceleration. The operating RF for this facility is 42 MHz that is the sec-
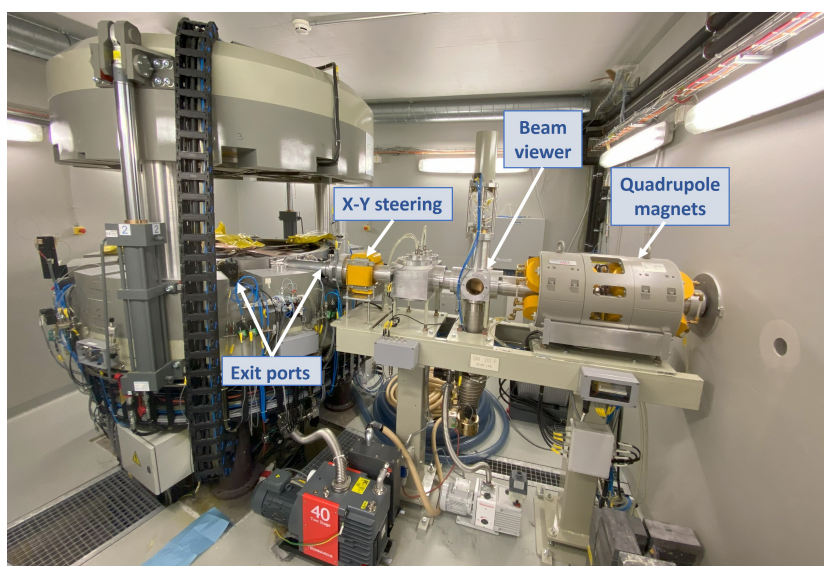
Figure 2.2: The Bern medical cyclotron Cyclone 18/18 HC by IBA and its BTL. The key components of the system, such as the X-Y steering magnets, the beam viewers and the focusing magnets are highlighted.

Constructor	Ion Beam Applications (IBA), Belgium; Type Cyclone 18/18 HC
Accelerated particles	H^- (D^- on option)
Energy	18 MeV (9 MeV for D^-)
Maximum current	150 µA (40 µA for D^-)
Average magnetic field	1.4 T
Radio frequency	42 MHz
Ion sources	2 internal PIG H^-
Extraction ports	8 (one connected with the BTL)
Extraction	Carbon foil stripping
Beam Transfer Line (BTL)	6.5 m long; two quadrupole doublets XY steering magnet; 2 beam viewers; neutron shutter

Table 2.1: Main characteristics of the Bern cyclotron and its Beam Transfer Line.

ond harmonic for H^- ions. After about 300 turns the ions reach the outer edge of the accelerator with a nominal energy of 18 MeV and are extracted by stripping the negative ions using pyrolytic carbon foils.

The angle of the stripper with respect to the beam can be adjusted to optimize the extraction. The energy of the beam was shown to be dependent on

the stripper angle ([37], [38], [39]). The working energy for our application was determined to be 17.90 ± 0.20 MeV using the plot presented in Figure 2.3 [38].
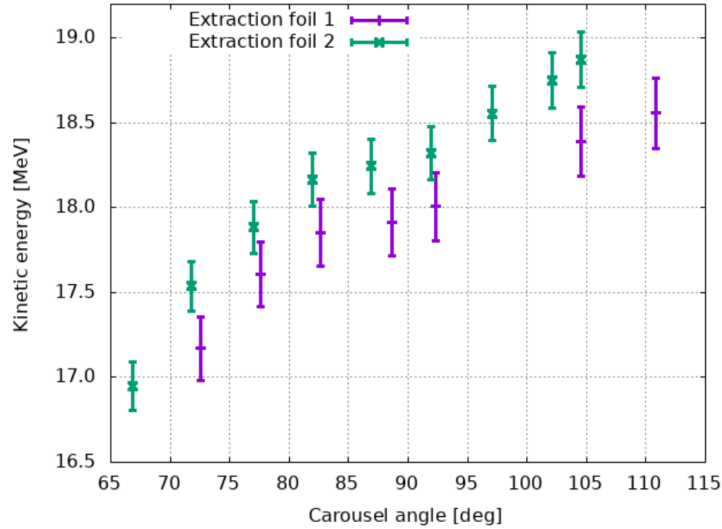
Figure 2.3: Proton beam energy as a function of the angle of extraction for the Bern medical cyclotron [38].

The BTL is 6.5 m long and carries the proton beam from one of the eight beam ports on the cyclotron to the BTL bunker. Customized solutions have been implemented in order to achieve an extraction efficiency of 95% with beam currents ranging from nA to the maximum value of $150\,\mu$A [40].

The BTL is equipped with XY steering magnets (shown in Figure 2.2) to center the proton beam exiting from the extraction port. The maximum achievable deflecting angle is ± 7 mrad in either the vertical or horizontal direction [40]. To obtain a well-centered beam, the mechanical alignment of all the BTL elements was ensured using lasers. Two quadrupoles, one situated in the cyclotron bunker and the other in the BTL bunker, can focus the beam to a minimum of one millimeter or disperse it to several centimeters [41]. For precise real-time monitoring of the beam position, intensity, and shape during data takings, a non-destructive beam monitoring detector developed by the MAPP group is implemented. This detector, called UniBEaM (Universal BEam Monitor), is based on two scintillating fibers moving vertically and horizontally through the beam by means of a high-precision motor [40]. The UniBEaM can be operated remotely from the control room during irradiations.

2.2   Beam constraints for cell irradiations

In the context of this thesis, cell irradiations had to be performed at conventional dose rates. The medical cyclotron typically operates at high currents for radioisotope production ($> 10\,\mu A$). Therefore, adapting the BTL to deliver steady currents within conventional dose rates posed a challenge.

The setup was subsequently optimized to deliver FLASH dose rates, as will be discussed in Section 3.3, with the goal of providing a facility for proton cell irradiations in this regime as well.

This section will present the constraints to be met in order to adapt the proton beam produced by a medical cyclotron for pre-clinical proton therapy studies.

The preliminary in-vitro studies performed throughout the project involved the irradiation of several cell strains of varying radiation sensitivities. The goal of the research is to compare the cell lines response to protons relative to X-rays in terms of cell survival. Each of the three cell lines was exposed to the same dose points, keeping the dose rate as constant as possible.

A fundamental factor to be investigated for the proper performance of the facility is the uniformity of the beam over the surface area of the cell culture to be irradiated. The cells were deposited on the proximal wall of a plastic flask, shown in Figure 2.4.

Figure 2.4: Example of a plastic flask. The cells are deposited on the front face which consists of a 1.5 mm-thick polystyrene layer. The area of the deposition is $12\ \mathrm{cm}^2$.

The area of the layer is $12\ \mathrm{cm}^2$, with the axes measuring 3 cm and 4 cm, respectively. To properly characterize the survival fraction, all the cells within a single flask must receive the same dose during irradiation. Hence, a sig-

nificant portion of our optimization process was dedicated to maximizing the uniformity of the delivered beam. Together with optimizing the beam uniformity, multiple energy and stopping power simulations were performed. Since the energy of the medical cyclotron proton beam is low with respect to the typical energies employed in proton therapy (Section 1.1), we had to carefully calibrate the system to this value. After any significant variation in the setup during the optimization process, an energy check was performed. Furthermore, since the cells are deposited after a thick layer of plastic, we had to ensure that the beam was not completely absorbed by this material. The beam energies emerging from each component of the instrumentation are listed in Section 2.5.1.

Finally, it was important to thoroughly characterize the dose rate to ensure the delivery of a precise and accurate dose to each cell flask. For this reason a Ionization Chamber was included in the setup and multiple calibrations were performed to define a solid calculation of the delivered dose.

2.3   Experimental setup for conventional irradiations

To summarize the previous section, the optimization steps performed to adapt the beamline to our application are the following:

1. Optimization of the uniformity of the dose deposited in the cell layer;

2. Maximization of the proton energy at the target level;

3. Reliable calculation of the dose delivered to each flask.

The optimal setup conceived to fulfill these requests is shown in Figure 2.5.

Immediately after the UniBEaM, a current measuring device was positioned. The device was composed of a collimator attached to an outer ring, all enclosed in a steel tube (Figure 2.6a). The outer ring made of PAI, a plastic material that exhibits notable strength under high temperatures, served as a support for the collimator and electrically insulated it from the beam pipe to enable the current readout. The collimator, featuring a 1 mm diameter pinhole aperture, absorbed any portion of the beam that did not pass through the opening. The current deposited by the impinging beam was measured by an electrometer directly connected to the collimator.

To disperse the beam after collimation, a scatterer was fixed over the 1 mm aperture on the distal face of the collimator as shown in Figure 2.6a. Then, the scattered beam was allowed to drift in vacuum through a 139.60 cm
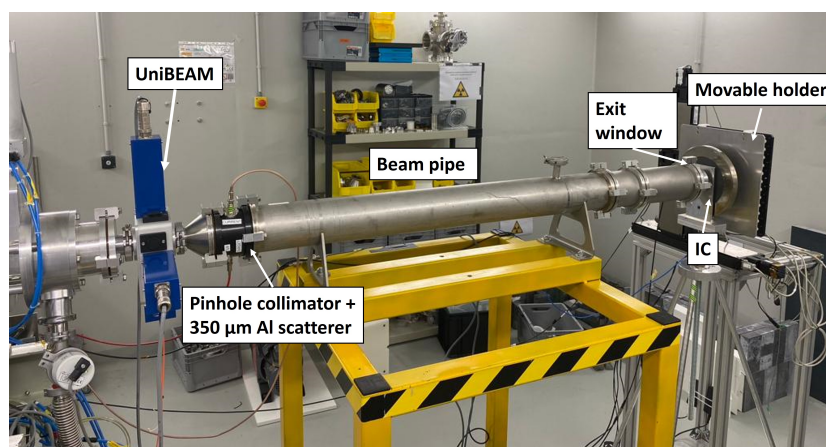
Figure 2.5: Picture of the experimental setup used for cell irradiations, consisting of a current measuring device with a pinhole collimator and an aluminium scatterer, linked to a 139 cm long beam pipe closed with an extraction window made of aluminium. After the exit window an IC and a movable stage to hold the flasks were located.

(a) *Collimator*   (b) *Exit window*   (c) *IC and holder*
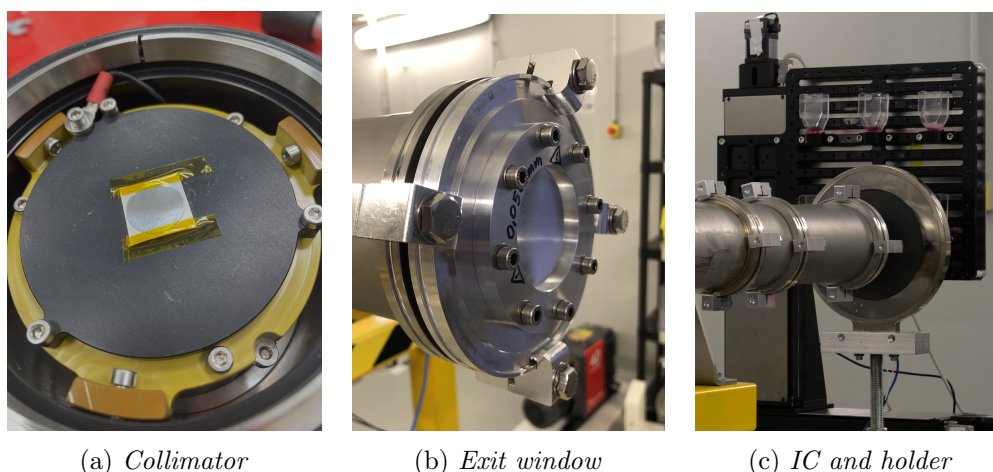
Figure 2.6: Details of the instrumentation composing the final setup. (a) The pinhole collimator (1 mm diameter) equipped with a 350 μm scatterer. The piece is part of the current measuring device. (b) The exit window composed by an aperture of 5 cm diameter with a 50 μm aluminium foil. (c) The IC and the remotely movable stage for the flasks.

long beam pipe. The beam pipe ends with an aluminium window of 5.5 cm in diameter to extract the beam in air (Figure 2.6b). The protons scattered at larger angles were completely absorbed by the pipe wall while the portion of the beam travelling with smaller scatter angles proceeded. The result was

a significant reduction of the proton flux and enhanced uniformity.

This solution was necessary to ensure a stable dose rate in the conventional regime.

A sketch of the evolution of the beam inside the tube is presented in Figure 2.7. The whole system including the collimator, the scatterer, and the pipe, was maintained under vacuum, as outlined in the figure, using a pump.

The pipe was supported by a large table of adjustable height, which allowed the position and angle of the beam pipe relative to the beam to be finely tuned.
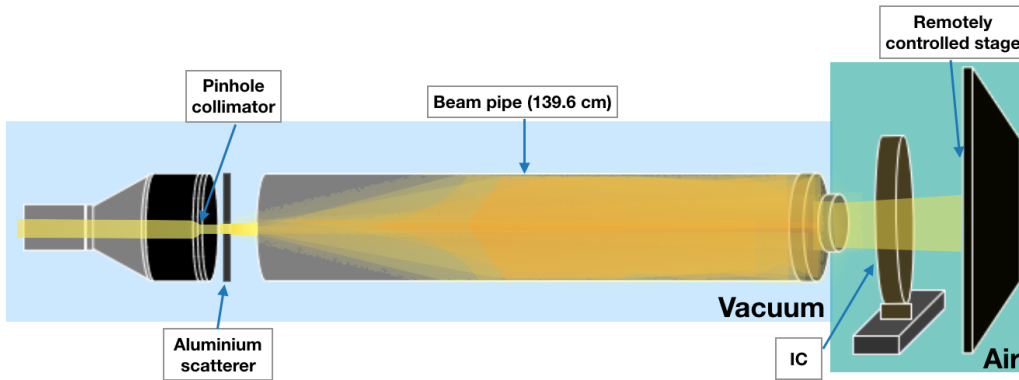
Figure 2.7: Scheme of the apparatus for cell irradiations. The evolution of the beam from the pinhole collimator to the target is outlined in yellow.

An in-beam ionization chamber was placed immediately after the extraction window to provide a real-time measurement of the proton current extracted from the exit window. Since the dose rate is directly proportional to the proton fluence, a linear calibration can be performed to obtain a real-time dose rate readout from the ionization chamber. This calibration was done using Gafchromic films, and is detailed in Section 3.2.

The ionization chamber used for this project is the circular plane-parallel monitor chamber type 786 manufactured by PTW dosimetry [42]. The chamber structure, depicted in Figure 2.8, consists of three electrodes made of a polyimide layers graphite coated on both surfaces. The outer electrodes each contribute 50% of the signal, while the central electrode provides the high voltage to enable the charge collection. The chamber is vented and operated at atmospheric pressure with a nominal voltage of $+400$ V.

A stage with remotely controlled stepper motors was positioned directly downstream of the ionization chamber (Figure 2.6c). The stage was used as a support for the flasks during the cell irradiations, and for Gafchromic films and scintillating fibers during the calibrations and setup optimizations.
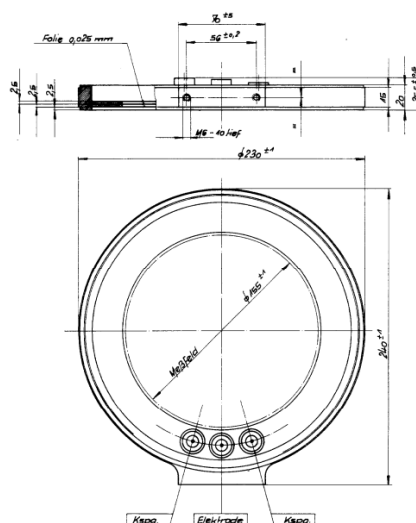
Figure 2.8: Sketch of the structure of the IC type 786 by PTW. The chamber is made up of three polyimide electrodes graphite-coated on both sides. The distance in air between each electrode is 2.5 mm.

Thanks to this system, multiple irradiations could be performed without entering the bunker each time a new target was required.

Due to the low energy of the protons extracted from this setup, scattering and energy loss in air can be significant. Since the dose rate is directly related to both the proton fluence and the proton energy, it is important to ensure that the proton path through air is kept consistent between different measurements.

2.4 Adaptation of the setup for dose delivery at FLASH rates

The future application of this project will involve repeating the cell irradiation study at the Bern medical cyclotron using FLASH dose rates. To adapt the facility to this purpose, a precise characterization of the setup at FLASH dose rates is necessary, and a dedicated dosimeter suitable for operations in this range has been developed. As described in Section 1.2, FLASH radiotherapy refers to irradiations with ultra-high dose rates delivered in a very short time of less than 500 ms. In addition to calibrating the facility at high dose rates, a mechanism to allow for very short irradiation times has been developed. The solutions adopted to implement an ultra-high dose rate detection system and to deliver very short irradiation pulses will be described

in detail in this subsection.

The ionization chamber is the standard detector in radiation therapy dosimetry. However, according to the PTW ionization chamber type 786 manual, the maximum dose rate for continuous irradiation at nominal voltage to reach 99% saturation is 18 Gy/s. This restriction limits its application in dosimetry at ultra-high dose rates.

The demands for a FLASH radiotherapy dosimeter, listed in Section 1.3, are well satisfied by scintillation-based dosimeters.

An innovative scintillator-based detection system, developed by the AEC-LHEP team for FLASH applications as part of the PRecision dOsimetry in FLASH radiotherapy with Optical Fibers (PROOF) project, was tested within this thesis. A schematic of the detector is presented in Figure 2.9.

In order to adapt the setup for FLASH rates, the ionization chamber was paired with the scintillator-based detection system to ensure a linear response, and a chopper wheel was mounted on the setup to precisely deliver the prescribed dose.
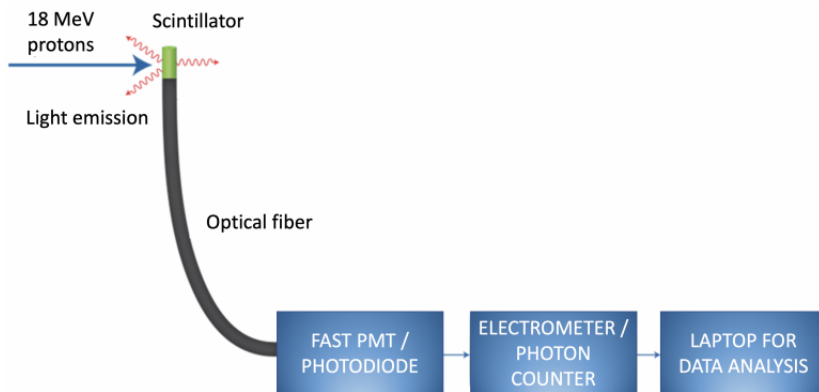
Figure 2.9: Schematic of the innovative FLASH detection system [30] developed as part of the PROOF project. The scintillator emits photons as a consequence of the radiation interaction; the light is then transported by the optical fiber to the readout system composed of a photodiode and a photon counter.

In this thesis, two different scintillator materials were evaluated: a plastic scintillator made of polystyrene (hereafter referred to as PS) and a Gadolinium Aluminium Gallium Garnet fiber doped with Cerium ($Gd_3Al_2Ga_3O_{12}$) (hereafter referred to as GAGG).

The PS features a fast decay time of 2.4 ns with an emission peak at 415 nm and a light yield of 8700 photons/MeV [43]. The GAGG crystal has a higher light yield of 30000 photons/MeV with an emission peak at 520 nm and a decay constant of 50 ns [44].

The crystal can be produced in extremely small dimensions (< 1 mm^3), ensuring a very good spatial resolution [45]. Both the PS and the GAGG had a size of $0.5 \times 0.5 \times 2$ mm^3.

The scintillator was mechanically coupled to an optical fiber cable with optical glue: the Norland optical adhesive 68 for the PS [46], and the Norland optical adhesive 63 for the GAGG [47]. The scintillator was covered with a layer of reflective paint and kept inside a light-tight rubber housing to minimize noise contributions from visible light. The fiber was connected through a patch panel to a laboratory located outside the bunker, in which the data acquisition system was set up to avoid exposing it to excessive radiation damage. The data acquisition system comprises a single-photon detector module to convert the optical signal into a digital signal and a Multi Channel Pulse Counting system (MCPC) to count the output digital signals. The single-photon detector used in our setup was the ID100-MMF100-UL by ID Quantique [48] based on a silicon avalanche photodiode (SPAD), with a 350-900 nm sensitivity range and a photon detection peak at 500 nm. This specification was fundamental to ensure maximum efficiency in detecting the emission peak of the scintillators. The ID100 features a high speed recovery time of less than 45 ns with a maximum count rate of 20 MHz. The output is an electric signal with an amplitude of 2.0 V.
The MCPC is a PhotoniQ model MCPC618 by Vertilon Corporation [49]. It features eight independent counting channels that enable the simultaneous readout of both the GAGG and PS fibers. The MCPC618 maximum count rate is higher than 250 MHz, enabling its use even with a large proton fluence.
The signal of the fibers was acquired using the Vertilon software in deterministic mode, with a rate of 100 Hz and an integration time of 9 ms.

In the framework of the PROOF project, multiple calibrations were performed using the 18 MeV proton beam produced by the cyclotron at the Bern University Hospital. The response of the PS was shown to be linear in the dose rate range from 30 to 780 Gy/s [30]. Another work [29] investigated the response of the GAGG scintillator, finding it to be linear in the 4-120 Gy/s range.

Based on these results and knowing the high time resolution stated by the manufacturer [44], scintillating fibers were tested to build an apparatus for cell irradiations at FLASH dose rates.

The measurements made using the new detection system will be presented in Section 3.3. The results will be discussed in Section 4.3.2.

To adapt the facility at the Bern medical cyclotron to deliver extremely short irradiation pulses we developed a mechanism based on a rotating wheel (hereafter referred to as chopper wheel).

The wheel, shown in Figure 2.10, was designed by the mechanical workshop of the LHEP. Its movement was driven by a PD-1021 stepper motor [50], which was controlled remotely via a python code. The wheel was mounted directly onto the distal end of the beam pipe such that the slit passes through the centre of the exit window.

(a)   (b)
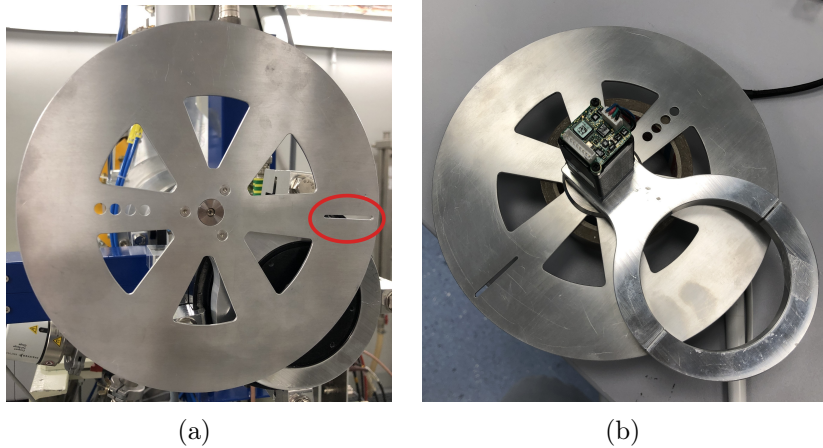
Figure 2.10: The chopper wheel: (a) front view and (b) back view. The wheel is designed to block the beam passage everywhere except within the slit highlighted in red in Figure 2.10a. The wheel is set in motion by the motor attached to its rear, and it can be mounted directly on the beam pipe thanks to the ring shown in Figure 2.10b.

The stepper motor was programmed to deliver a single pulse at various speeds depending on the desired dose rate and total dose. The wheel is first accelerated to reach the required angular velocity before the slit passes in front of the beam (approximately 75% of a full turn). To ensure a uniform exposure of the target, the wheel must rotate at a constant speed while the slit intersects the exit window. After the slit has completely crossed the exit window and the beam pulse has been delivered, the wheel is decelerated in the remaining path before the exit window is intersected once more and stopped, finally returning to its initial position by rotating in reverse. A python code was used to define the angular velocity and acceleration of the wheel according to the required dose rate and total dose within the pulse.

2.5   Beamline optimization

2.5.1   Stopping power simulations

Before proceeding with the alignment of our setup, it was necessary to evaluate the effect of the materials composing the various layers of the apparatus on the proton beam energy. The energy after each layer was simulated using the LISE++ code [51].

The LISE++ code was developed to simulate the production of radioactive ion beams. Based on well-established models, the program can predict the properties of a beam interacting with matter. The program was used with the input settings listed in Table 2.2 to compute the energy of the proton beam produced by the Bern medical cyclotron at the entrance and after the cell layer in the final setup. The starting proton beam energy was set to 17.90 ± 0.20 MeV.

The results are presented in Table 2.2.

Layer	Material	Thickness [µm]	Density [g/cm^3]	Energy [MeV]
Scatterer	Aluminium	3.50E+02	2.702	1.582E+01
Vacuum (pipe)	Air	1.40E+06	3.800E-12	1.582E+01
Exit window	Aluminium	5.00E+01	2.702	1.551E+01
Air gap 1	Air	6.75E+04	1.205E-03	1.528E+01
IC graphite (tot.)	Graphite	1.80E+02	0.440	1.505E+01
IC Al (tot.)	Aluminium	1.00E+01	2.702	1.499E+01
IC kapton 1	Kapton	2.50E+01	1.420	1.488E+01
IC air gap 1	Air	2.50E+03	1.205E-03	1.487E+01
IC kapton 2	Kapton	2.50E+01	1.420	1.476E+01
IC air gap 2	Air	2.50E+03	1.205E-03	1.475E+01
IC kapton 3	Kapton	2.50E+01	1.420	1.464E+01
Air gap 2	Air	6.50E+04	1.205E-03	1.441E+01
Flask wall	Polystyrene	1.50E+03	1.060	7.690E+00
Cells	Liquid water	1.50E+01	1.000	7.603E+00

Table 2.2: Summary of the settings used in the LISE++ simulation to model the propagation of the beam energy through the layers of materials in the experimental setup. The energy in column 4 is the resulting energy after each layer. The entrance energy was 17.90 MeV.

From the simulation, we derived a beam energy at the entrance of the cell layer of 7.69 ± 0.50 MeV. Starting from this, the stopping power was then

calculated using Pstar [52]. The Pstar program, developed by the National Institute of Standards and Technology (NIST), calculates the stopping power for protons of various energies in different materials using Bethe's stopping-power formula [53].

The total stopping power in water for the proton beam at the entrance of the cell layer was evaluated to be 56.34 MeV·cm^2/g. The proton stopping power of liquid water as a function of the beam energy is shown in Figure 2.11.
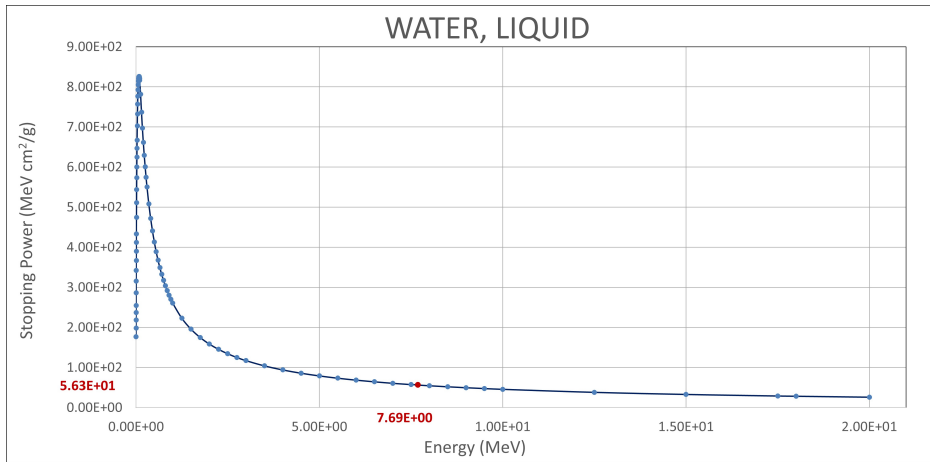
Figure 2.11: Stopping power plot for a proton beam in water, simulated by Pstar. The experimental stopping power derived for the case under analysis is highlighted in red on the vertical axis.

These simulations indicate that the total stopping power is highly sensitive to small variations in the proton energy in this energy range. To limit this effect and reduce uncertainty contributions from variations in stopping power, the position of each element composing the setup was kept consistent for all the measurements and irradiations to ensure constant air gaps.

It is worth noting that the wall of the flask within which the cells are contained has a strong impact on the energy of the protons impinging on the cells. In future work, alternative flask designs will be considered to minimize this effect.

2.5.2   Alignment and uniformity measurement

Before defining the final setup, multiple configurations were evaluated to achieve the optimal properties for the case under analysis listed in Section 2.2.

The first step of the optimization procedure was the achievement of an operating dose rate in the conventional regime. The long beam pipe was a

key element to reduce the proton flux before the extraction of the beam into air and the thickness of the aluminium scatterer and exit window both had a major role in the uniformity of the extracted beam. The total thickness of the scattering material used to obtain a uniform beam spot over the required area was primarily limited by the energy of the proton beam. Multiple configurations were tested, measuring the dose uniformity and simulating the resulting beam energy delivered to the cells using the LISE++ code. The uniformity test involved mounting a Gafchromic film sample on the holder after the ionization chamber. The film was exposed to the beam and subsequently scanned. A python code was employed to analyze the spot on the sample, defining the Gaussian distribution of the beam on the circular region outlined by the spot.

Two key considerations were taken into account when optimizing the layers of aluminum after the collimator aperture and at the exit window. First, the total amount of aluminum that can be used as a scatterer is limited by the beam energy. Additionally, the exit window needs to be thick enough to withstand the vacuum. The scatterer located immediately distal to the collimator position was found to have the greatest impact on uniformity as it is situated before the long beam pipe, allowing scattered protons to spread out over this distance. Consequently, the thickness of the exit window was reduced to the minimum allowed by the vacuum requirements, and the scattering material at the collimator was maximized. The maximum value was chosen taking into account the constraints on the beam energy to ensure that the beam was not stopped too quickly.

The configuration that resulted in the best balance of dose uniformity and remaining beam energy was a scatterer of $350\,\mu m$ at the position of the pinhole collimator and a $50\,\mu m$ layer at the exit window.

The SRIM [54] program was employed for a simulation of the setup to extract the scattering angle. SRIM comprises a set of Monte Carlo - based software packages that compute various aspects of ion transport in materials, like ion trasmission, range and diffusion.
The simulation provides the angular distribution of the proton beam after crossing the scatterer. The root mean square of this angular distribution is 20 mrad (isotropic), from the beam axis at the entrance of the beam pipe. A graphical representation of the simulation is presented in Figure 2.12.

An additional increase of the uniformity was obtained varying the air gaps between the exit window, the ionization chamber and the flasks. Various setups were investigated using the same procedure as above for the uniformity test and at the same time simulating the beam energy with LISE++. The scatter in air was proved to significantly increase the flatness of the beam at the target position, but the energy loss in the layer was significant.
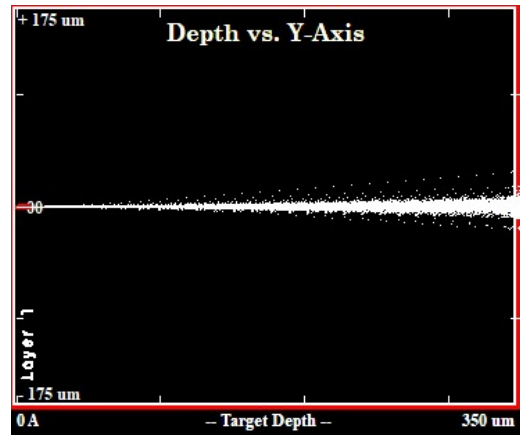
Figure 2.12: Angular distribution of the 18 MeV proton beam inside the 350 μm Al scatterer. The x-axis is the depth in the aluminium target. The root mean square scatter angle that resulted from this simulation is 20 mrad (isotropic).

The final size of the air gaps is presented in Figure 2.13: a constant spacing of 6.7 cm between the exit window and the ionization chamber, and 6.5 cm between the rear face of the ionization chamber and the target was maintained for all the measurements.
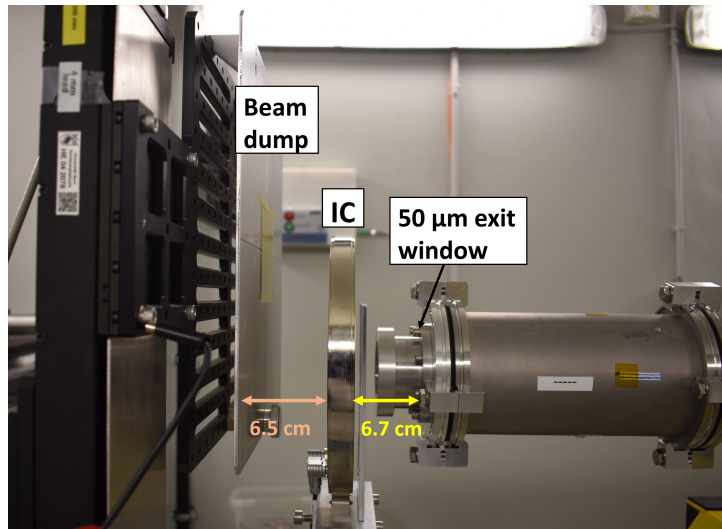
Figure 2.13: Photo of the IC in its reference position. The labeled distances are from the exit window to the frontal face of the IC, and from the back face of the IC to the target, respectively.

These values have been chosen as a compromise to achieve good uniformity without excessively impacting the beam energy and maintaining a safe

distance between the fragile ionization chamber and the nearby instruments.

Once the final components of the apparatus were defined, we proceeded with the alignment of the setup with the proton beam. The BTL bunker is equipped with adjustable lasers calibrated approximately to the centre of the collimator positioned after the UniBeaM. However, the setup used for this project includes a long beam pipe connected to this collimator that constitutes a significant extension from the calibration point. Therefore, after the alignment of the instruments with the external lasers, the positioning of the components with respect to the beam was further investigated. Ensuring that the beam spot is well-centered within the beam pipe is a crucial step in optimizing the uniformity of the delivered beam. The angle of the beam in the BTL is highly dependent on the stripper angle and the current on the steering and focusing magnets, therefore the position of the beam was first verified by irradiating a Gafchromic film. For this preliminary alignment test, the 350 µm aluminium scatterer was removed to improve the visual analysis of the beam spot. A picture of the beam spot is shown in Figure 2.14.
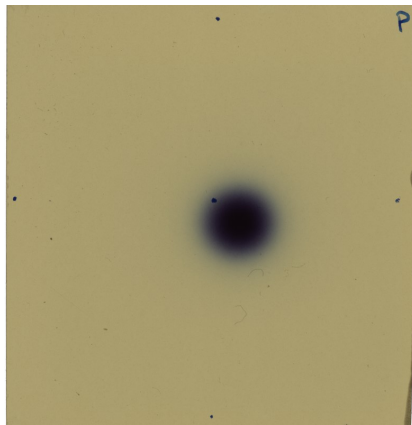
Figure 2.14: Picture of a film irradiated during the beamline alignment optimization. The point at the center of the film represents the center of the beam stopper. For this test no scatterer was used at the pinhole collimator.

The location of the beam spot center was compared with the center of the beam stopper marked on the film. Using this irradiated film as a reference, the position of the beam dump was adjusted so that the unscattered beam was delivered to the centre of the target position, at a well-known reference position relative to the laser alignment system.

Once the unscattered beam spot was aligned with the target, we reinserted the scatterer and verified with the same method the alignment of the beam pipe with the center of the scattered beam. An example of a film irradiated

during this test is shown in Figure 2.15 together with the horizontal and vertical profiles from the ImageJ software [55].
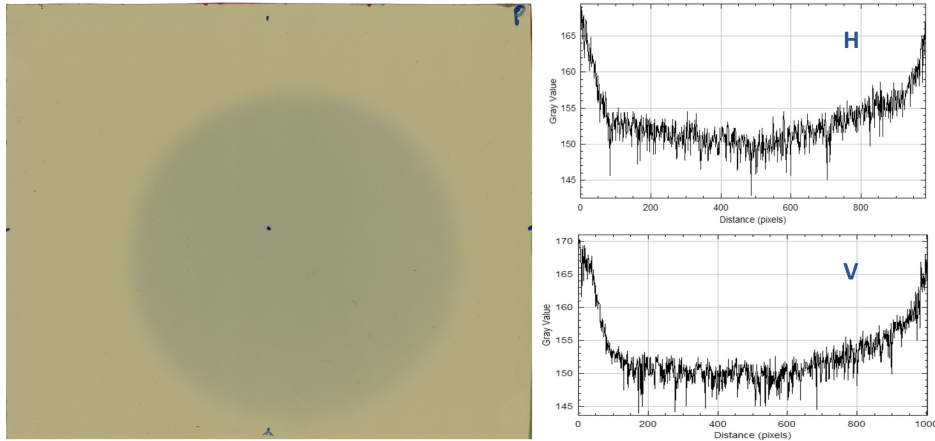
Figure 2.15: Scanned film after the initial alignment test and the horizontal (top) and vertical (bottom) profiles obtained with the ImageJ analysis.
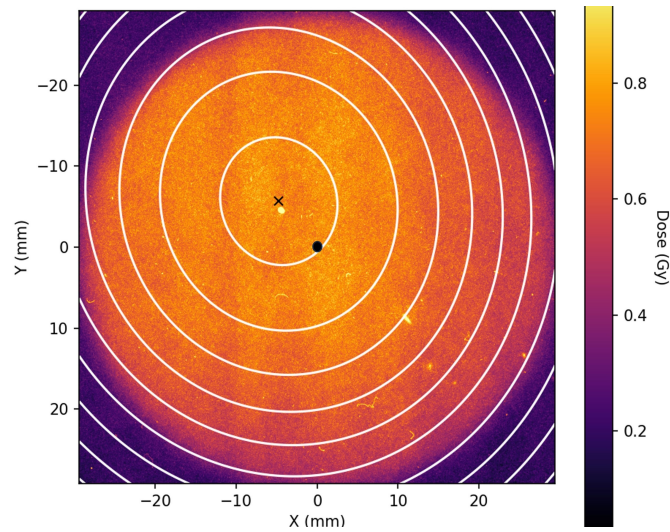
Figure 2.16: Beam distribution over the spot area on the Gafchromic film. The black cross corresponds to the center of the beam, while the yellow point represents the center of the target. A black point outlines the center of the spot, corresponding to the center of the beam pipe.

The bottom plot of Figure 2.15 presents a non-centered vertical distribution of the beam. This outcome indicates that the beam, aligned with the target, was not centered within the beam pipe. The analysis of the

(a) (b)
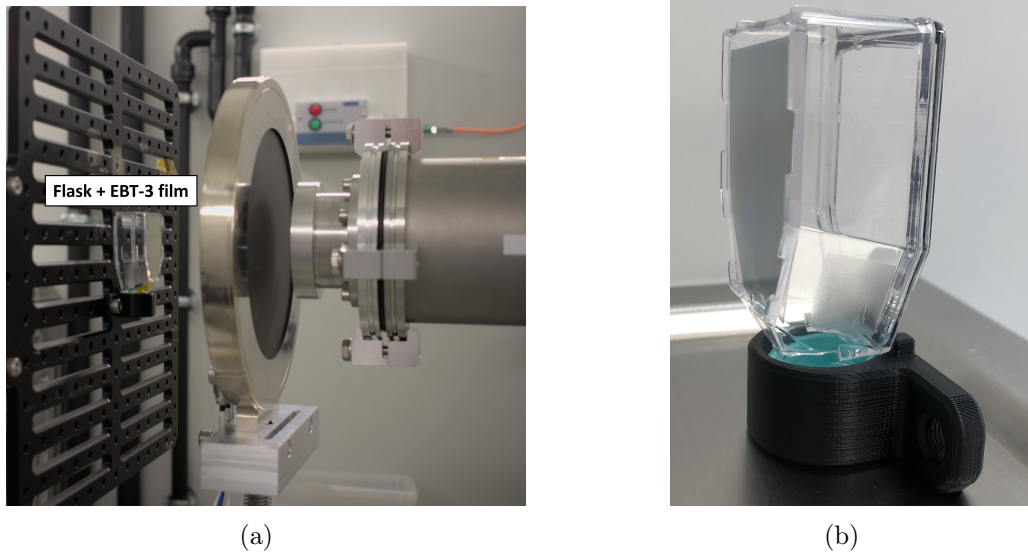
Figure 2.17: Detail of the setup for the tests with the Gafchromic EBT-3 film inside a flask. This system was built to simulate the beam attenuation that occurs during cell irradiations in order to irradiate the Gafchromic film with the same beam expected at the entrance of the cell layer.

beam distribution determined the location of the beam center (black cross in Figure 2.16), which was not corresponding to the spot center (black dot in Figure 2.16) by 3 mm in the horizontal axis and 5 mm in the vertical axis. This minor adjustment to the beam pipe was performed thanks to the supporting table, and a final irradiation allowed to evaluate the resulting uniformity. The resulting beam distribution will be presented in Chapter 4.1.

After achieving the correct alignment, an additional test was performed with a flask in position to determine the beam uniformity at the entrance of the cell layer. For this irradiation, a flask was customized removing the back face and a Gafchromic film was taped on the inside of the frontal face. This flask was positioned on the stage, as shown in Figure 2.17, to measure the exact dose distribution that would be delivered to the cells.

The scanned Gafchromic films were examined with a python code to extract the beam distribution; the result will be presented in Chapter 4.1.

The proton beam, precisely aligned with the target and the setup and optimized for our application, was characterized using the ionization chamber and the previously described scintillating fibers.

Chapter 3

Dose calibration

As the irradiation of cells requires a precise knowledge of the delivered dose, it was essential to develop a robust calibration procedure for our setup. This chapter outlines the techniques and methods employed to calibrate the ionization chamber and the scintillating fibers. The calibration process was performed using Gafchromic films [56], which were irradiated at several independent facilities as a part of this thesis.

3.1 Gafchromic film dose calibration

Radiochromic films are self-developing films insensitive to visible light, which can be used for absolute dosimetry [57]. Gafchromic films are a type of radiochromic film employed in medical radiation dosimetry for dose verification and quality assurance. To obtain an absolute dose measurement, a calibration of the dose deposited in the film as a function of the measured pixel value is needed. The calibration is performed by irradiating several films in a specified dose range, and establishing a relationship between film response and delivered dose.

The procedure followed in the multiple film calibrations performed in the context of this thesis is described and discussed in this chapter.

Radiochromic films feature an active layer composed of a radiation-sensitive material that progressively changes colour as a function of the deposited energy by the ionizing radiation. The interaction with the radiation causes the polymerization of the material through the formation of colored polymer chains. The change in colour is monotonically correlated with the absorbed dose [58].

Before the development and widespread use of radiochromic films, conventional films used in X-ray dosimetry were made of an emulsion of silver
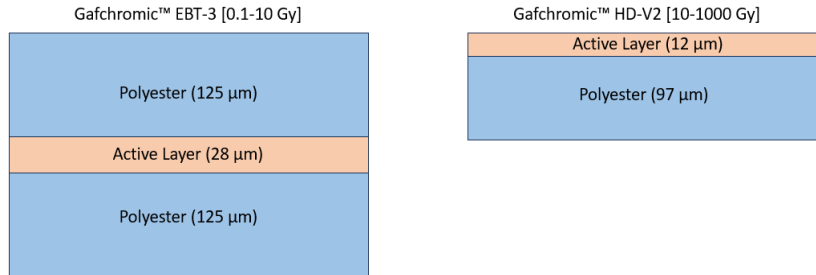
Figure 3.1: Scheme of the Gafchromic EBT-3 film and the Gafchromic HD-V2 film structure.

halide radiation-sensitive crystals. When the emulsion is exposed to radiation, a latent image forms on the surface, then a developing agent and a photographic fixer are used to make the image permanent [59]. In contrast, for radiochromic films, no developing process is required and the primary image is formed almost instantly [60]. The self-developing nature of these films simplifies the readout procedure.

Gafchromic films exhibit almost water-equivalence, which is crucial for their application in dosimetry [61]. Moreover, they show a very small dependence on the energy of the incident radiation, which is essential for comparisons between results obtained from different radiation sources. The dependence on the dose deposit rate is also negligible, allowing us to employ these films at both conventional and FLASH dose rates.

A variety of Gafchromic film types is available. Each film has a different sensitive dynamic range suitable for various applications, from dose verification in medical treatments, to particle beam profile and homogeneity characterization [58]. In this work, two types of Gafchromic films, produced by Ashland Advanced Materials [56], have been used: Gafchromic EBT-3 and HD-V2 films. A scheme of the structure of the EBT-3 and HD-V2 films is presented in Figure 3.1.

The Gafchromic EBT-3 (External Beam Therapy) film is composed of a $28\,\mu m$ thick active layer, sandwiched between two $125\,\mu m$ polyester substrates. Thanks to the symmetric structure of the film, it is not necessary to monitor the side of the film exposed to the light source during the dose readout procedure.

EBT-3 films have an optimum dose range from 0.2 Gy to 10 Gy and a sub-mm spatial resolution, making them a good choice for the majority of our measurements [62].

Gafchromic HD-V2 films were employed for the calibration of the dose

rate delivered by our beamline at FLASH rates, due to their sensitivity to higher doses. Their spatial resolution is approximately 5 μm and the dynamic dose range extends from 10 Gy to 1000 Gy [63], thus allowing to calibrate at dose rates up to 88 Gy/s without causing the films to saturate too quickly.

The HD-V2 structure is asymmetric, meaning that their orientation needs to be carefully considered during the calibration procedure. They are composed of a 12 μm thick layer containing the active element, which is deposited on a 97 μm polyester substrate.

3.1.1 Calibration procedure and methods

The characteristic dose response curve of the films may vary from one batch to another, due to slight variations in manufacturing, so a separate calibration is required for each batch. This calibration must be performed with a well-validated source of ionizing radiation.

Film samples were irradiated with a series of known doses spanning the relevant dynamic range. For most of the calibrations performed within this project, the samples were cut into squares of 3 cm × 3 cm. The only exception was the one for the calibration at the Swiss Federal Institute of Metrology (METAS) where the dimensions of the samples were adapted to the size of the film holder, namely 3.5 cm × 4 cm. To avoid artifacts from skin oils or scratches, the films were always handled carefully, using gloves.
The change of the film coloration has been shown to be slightly dependent on the time interval between the irradiation and the dose readout [64]. To take this effect into account and ensure consistency, we employed a standard 24-hour gap between the end of the irradiation and the scanning procedure.

An Epson Perfection V850 Pro flatbed scanner, and its EPSON SCAN Ver.3.9.3.5 software, were used to analyse all the exposed films used for the calibrations and the following measurements.

A previous work showed that the scanning procedure requires particular care as it can affect the final results [64]. For instance, light scattering by the particles composing the active layer can cause non-uniformities in the response of the scanner. This effect is referred to as the lateral dependence artifact and it varies as a function of the position of the film along the horizontal axis of the scanner. To minimize its impact, the films have been scanned individually and a reference frame has been outlined on the scanner surface to ensure consistent positioning.

Since the scanning procedure induces polarization effects on the film, its orientation on the scanner must be taken into consideration [65]. To keep track of the film direction, its top right corner was marked before the irradiation and the scanning occurred always in the same orientation.

The digitizing procedure was performed ensuring the trimming and color correction options, usually present in the scanner settings, were not selected. The scanning resolution was set to 400 dpi. Images were acquired in transmission mode and landscape orientation, as recommended by the manufacturer, and saved in "TIFF" format.

The digitized pictures were analysed using the ImageJ software [55]. The 8-bit gray-scale Pixel Value (hereafter referred to as PV) was extracted in a circular region of interest (ROI) of 20 mm diameter at the center of the film. The PV was calculated using the weighted RGB conversions described by the following equation [66]:

$$Gray = 0.299 \cdot red + 0.587 \cdot green + 0.114 \cdot blue \tag{3.1}$$

According to a previous work [67], the film darkening trend is well represented by the Green-Saunders equation (3.2):

$$PV = PV_{min} + \frac{(PV_{max} - PV_{min})}{1 + 10^{\beta} \cdot (\log D_0 - \log D)} \tag{3.2}$$

In this equation, PV is the pixel value, PV_{min} and PV_{max} are representative of the minimum and maximum PV, respectively, β is a parameter associated with the slope of the curve and D_0 is the abscissa of the inflection point of the sensitometric curve [67, 68].

The PVs, extracted from ImageJ, and the experimentally measured dose values were plotted against each other. A fit of the curve with the Green-Saunders formula (3.2) was performed using a python script.

The best estimates of the free parameters (PV$_{min}$, PV$_{max}$, β and D$_0$), their uncertainties and the values of the reduced chi-square (χ^2) were evaluated for each batch.

An example of an absolute calibration of Gafchromic EBT-3 films performed with several radiation sources and energies is presented in Figure 3.2.

The reciprocal function of the Green Saunders equation can be written as follows (3.3):

$$D = D_0 \cdot \left(\frac{PV - PV_{min}}{PV_{max} - PV} \right)^{\frac{1}{\beta}} \tag{3.3}$$

Using the parameters obtained from the fit, the unknown absorbed dose distribution in a given irradiated film can be calculated from equation 3.3.
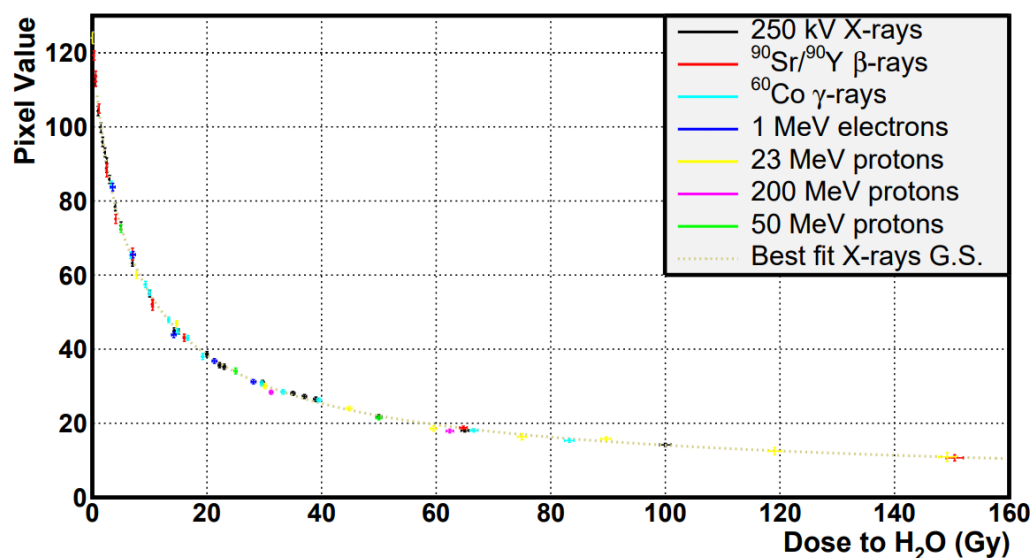
Figure 3.2: Plot of an absolute calibration of Gafchromic EBT-3 films [67]. The different radiation sources and energies are listed in the top right corner. The gray points represent the Green Saunders fit for X-rays.

The uncertainty in the dose value ΔD was calculated using the standard error propagation of the standard deviation of the PV, without considering the uncertainties on the fit parameters.

In the context of this thesis, three independent calibrations were performed at three different facilities:

- At the clinical linear accelerator (linac) of the Radiation oncology clinic at Inselspital, using a photon beam;

- At the Swiss Federal Institute of Metrology (METAS), using a ^{60}Co source;

- At the certified laboratory ISOF (Institute for Organic Synthesis and Photoreactivity) CNR Bologna, using a ^{60}Co source.

The first two calibrations were performed with the Gafchromic EBT-3 films while the third one aimed at characterizing the HD-V2 Gafchromic films.

The results of these calibrations will be presented in Chapter 4.2.

3.1.2 Irradiation with a clinical linac

The Gafchromic EBT-3 films were irradiated with a 6 MV photon beam delivered by the TrueBeam Varian linac [69] at the Radiation oncology clinic

at Inselspital. This linear accelerator is used daily for patient treatment, therefore the dose is precisely known and can be considered as a reference.

The films were exposed to fixed doses spanning the optimal dose range of the batch. Specifically, the targeted doses were 0.1, 0.4, 0.6, 0.8, 1, 2, 4, 6, 8, 10, and 15 Gy. The term "targeted dose" refers to the dose requested by the delivery system, which may vary slightly from the exact delivered dose due to uncertainties intrinsic to the facility.

A calibrated PTW-Freiburg Farmer TM30012-1 ionization chamber [70] was used to monitor the delivered dose. The films and the ionization chamber were arranged as shown in Figure 3.3.
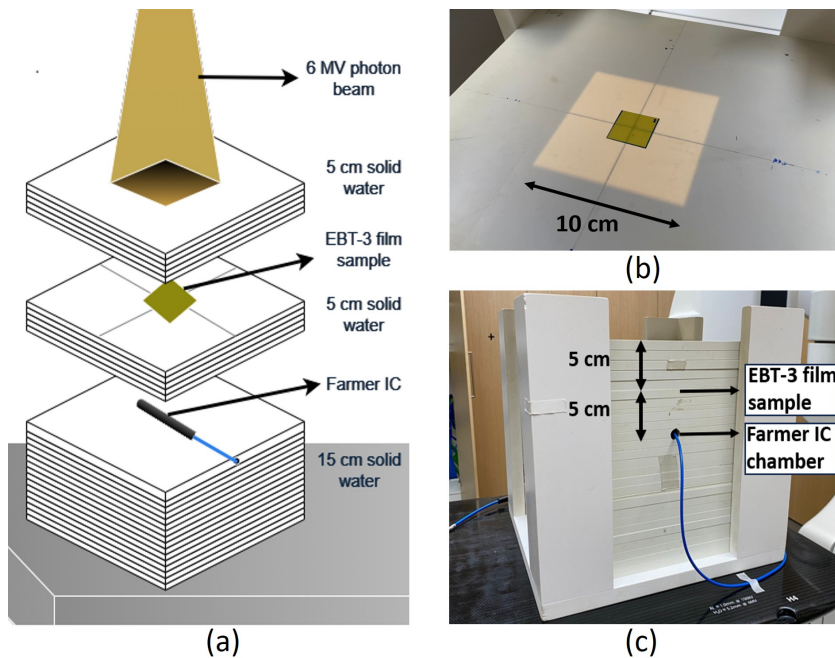
Figure 3.3: (a) Scheme of the setup used for the film calibration with the clinical linac. (b) Photo of the sample film placed at 5 cm depth, centered with the beam. (c) Side view of the assembled phantom; the IC was positioned 5 cm under the sample film, thus the measuring point was fixed at a depth of 10 cm with respect to the phantom surface.

A solid water phantom was placed directly under the linac aperture; the samples were positioned 5 cm below the surface of the phantom, centered in the field size of the beam. The ionization chamber was placed an additional 5 cm below this level. Therefore, the dose measurement point was located at a total depth of 10 cm, while the PV was evaluated at a depth of 5 cm.

The field size was set at 10 cm × 10 cm and the distance from the source

to the surface of the phantom (SSD) was 100 cm.

The ionization chamber used to measure the absorbed dose was "open-air", meaning that it was not sealed and that the sensitive gas volume was in direct contact with the surrounding atmosphere. Because of this, the mass of air inside the sensitive volume varied with the ambient pressure and temperature, affecting the ionization chamber response. To account for this, the pressure was measured with a barometer mounted inside the treatment room, and the temperature was measured at the position of the ionization chamber. These values were used to define the correction factor $K_{T,P}$ in equation 3.4.

The Monitor Unit (MU) is the standard unit of dose delivery for a medical linac. During the commissioning measurements performed upon the machine acceptance, the conversion factor to derive the MU necessary to deliver a precise dose is evaluated. With this conversion, we defined the MUs required for each film sample and we proceeded with the calibration.

The films were scanned and analysed using the method outlined in Section 3.1.1. Figure 3.4 shows the images of scanned films, from which the PV was extracted. The PVs and the delivered doses for each film are presented in Table 3.1.
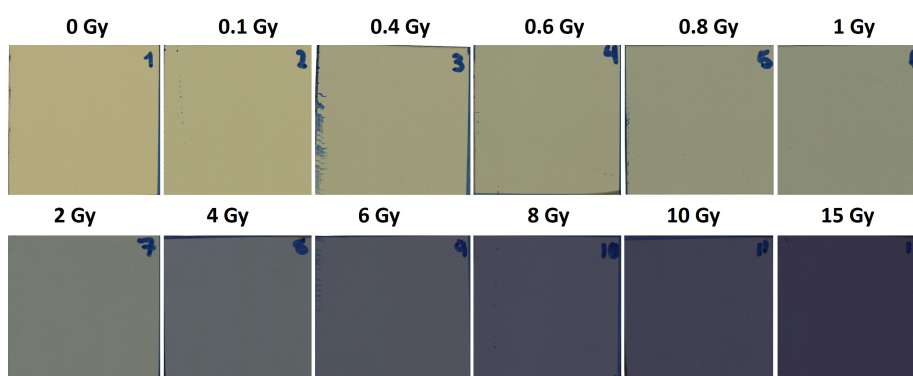
Figure 3.4: Scanned images of the Gafchromic EBT-3 films irradiated with X-rays at the clinical linac. The targeted dose for each sample, in Gy, is also specified. The labels in the top right corner correspond to the film number in Table 3.1 and ensure that the orientation is maintained throughout the calibration.

The exact dose to which each film was exposed was provided by the Radiation oncology clinic. This value is calculated from the ionization chamber output, taking into account different calibration factors derived following the TRS-398 protocol [24].

The equation used by the Radiation oncology group to measure the final dose is:

Film number	Dose to film [Gy]	Dose uncertainty [Gy]	PV	PV uncertainty
1	0.000	0.000	168.54	1.61
2	0.101	0.0007	164.05	1.59
3	0.402	0.0027	153.95	1.50
4	0.603	0.0040	148.06	1.55
5	0.804	0.0054	142.34	1.52
6	1.005	0.0067	137.89	1.47
7	2.011	0.0135	120.04	1.34
8	4.024	0.0270	97.49	1.35
9	6.037	0.0404	84.10	1.43
10	8.051	0.0539	74.01	1.51
11	10.066	0.0674	66.85	1.45
12	15.105	0.1012	54.40	1.38

Table 3.1: Summary of the doses delivered by the facility and the PVs extracted using ImageJ during each film irradiation with the clinical linac. The uncertainties on both values are also included.

$$Dose = M_Q \cdot N_{D,W} \cdot K_Q \cdot K_S \cdot K_{T,P} \tag{3.4}$$

In the formula, M_Q represents the output of the Farmer chamber, $N_{D,W}$ is the calibration factor of the ionization chamber expressed in Gy/nC, K_Q is the quality factor of the beam, K_S is the correction factor to account for ionic recombination, and $K_{T,P}$ is the correction for the measured temperature and pressure. These quantities, except for $K_{T,P}$ which can vary for every exposure, are defined during the commissioning measurements.

3.1.3 Irradiation at the Federal Institute of Metrology (METAS)

The Federal Institute of Metrology (METAS), located in Bern, is the Swiss national metrology institute, and is responsible for all matters relating to measurement, including equipment and procedures [71].

The ^{60}Co source facility at the institute serves as a reference for Switzerland and was used in this project to perform a calibration in water of the Gafchromic EBT-3 films.

The ^{60}Co radioisotope produces gamma rays with energies of 1.173 and 1.332 MeV and has a half-life of 5.27 years.

The Alcyon II teletherapy unit was paired with a water phantom. A gantry mounted directly onto the teletherapy unit allows a target to be precisely aligned with the ^{60}Co source, and the height of the entire unit to be adjusted as a whole. The facility is shown in Figures 3.5 and 3.6.

(a)   (b)
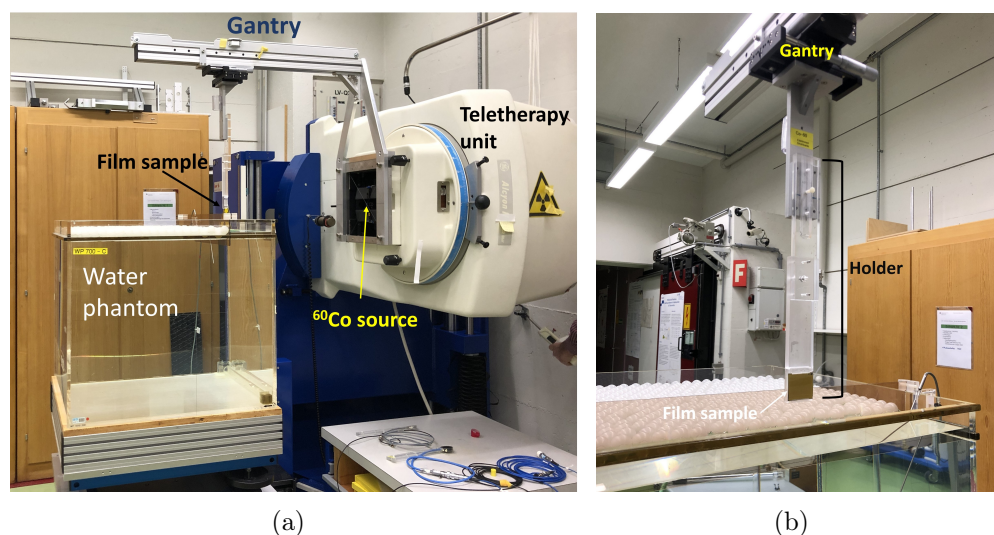
Figure 3.5: Photos of the setup for the irradiation with a ^{60}Co source at METAS. (a) The film sample was placed inside a holder mounted on the gantry. (b) The gantry extends till the teletherapy unit; the height can be adjusted as a whole with a motor implemented in the machine.

The films, cut in samples of 35 mm × 40 mm, were placed inside a holder mounted on the gantry (Figure 3.5b), and lowered to a calibrated position within the water phantom, as shown in Figure 3.6a.

The total distance from the source to the measuring point was 100 cm, including a 5 cm equivalent depth in water. This distance was carefully measured prior to each irradiation using the apparatus shown in Figure 3.6b. The gamma field at the measurement position had dimension of 10 cm × 10 cm.

To compare the results with those extracted from the calibration performed at the clinical linac, the dose points were kept the same as those listed in Section 3.1.2, namely 0.1, 0.4, 0.6, 0.8, 1, 2, 4, 6, 8, 10 and 15 Gy.

The samples were scanned and analysed as described in Section 3.1. The images of the 11 irradiated films and the reference blank are shown in Figure 3.7. In Table 3.2, the delivered doses together with their uncertainties and the PVs are presented.

The uncertainty on the dose was provided by METAS, and considers the uncertainty on the ^{60}Co dose rate delivery and on the film positioning in

<div align="center">(a)   (b)</div>
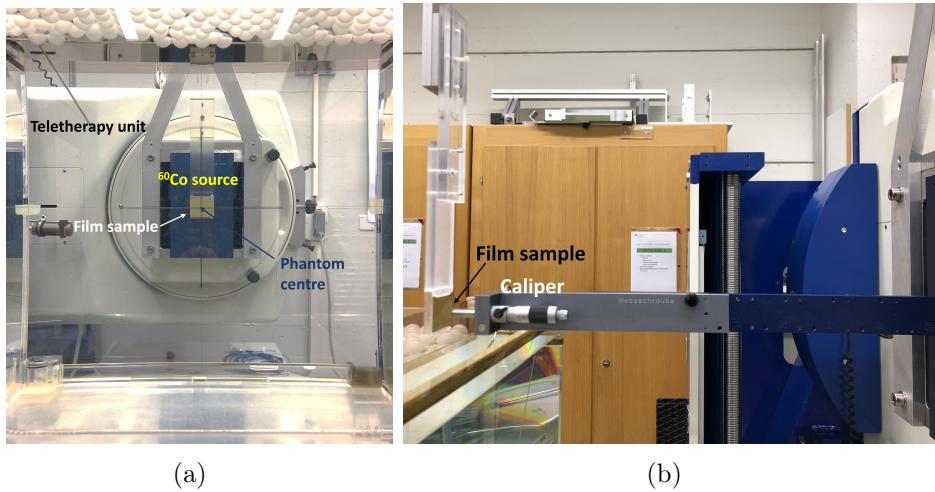
Figure 3.6: Photos of the alignment procedure for the irradiation with a ^{60}Co source at METAS. (a) The film sample was aligned with the center of the water phantom. (b) The SSD was defined using a caliper.
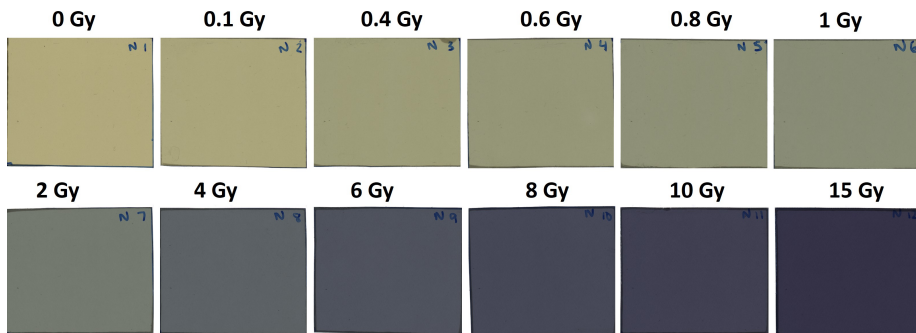
Figure 3.7: Scanned images of the Gafchromic EBT-3 films irradiated at METAS with gamma rays from a ^{60}Co source. The targeted dose for each sample, in Gy, is also specified. The labels in the top right corner correspond to the film number in Table 3.2 and ensure that the orientation is maintained throughout the full calibration.

water.

Samples from a batch of EBT-3 films which had expired at the beginning of the year 2023 were also irradiated. The film holder provided by the facility, presented in Figure 3.5b, is designed to accommodate up to three samples, enabling the simultaneous irradiation of all of them.

The expired films exhibited a slight visual difference in color compared to the new batch, therefore the purpose of the test was to assess and quantify the impact of this color variation on the calibration curve.

Film number	Dose to film [Gy]	Dose uncertainty [Gy]	PV	PV uncertainty
1	0	0.000	166.65	1.69
2	0.10	0.0004	162.58	1.52
3	0.40	0.0016	152.47	1.47
4	0.60	0.0024	146.27	1.47
5	0.80	0.0032	140.81	1.42
6	1.00	0.0040	136.03	1.35
7	2.00	0.0081	118.49	1.35
8	4.00	0.0161	96.91	1.36
9	6.00	0.0242	83.51	1.40
10	7.99	0.0323	72.76	1.44
11	9.99	0.0403	65.76	1.43
12	14.99	0.0605	53.38	1.36

Table 3.2: Summary of the doses delivered by the facility and the PVs extracted using ImageJ during each film irradiation using a ^{60}Co source at METAS. The uncertainties on both values are also included.

The result of this study will be presented in Section 4.2.

3.1.4   Calibration at ISOF CNR Bologna

The Institute for Organic Synthesis and Photoreactivity (ISOF) is one of the 90 institutes of the National Research Council of Italy (CNR) [72].
The centre, located in Bologna, has a Gammacell220 irradiation unit to produce gamma-rays from a ^{60}Co source.
This equipment is capable of delivering high dose rates enabling the calibration of HD-V2 high-dose dosimetry films across a wide range of dose rates, from conventional to FLASH regimes. After characterizing the films, we used them in irradiations for research on FLASH dose rates.

The unit comprises a circular radiation source permanently housed within a lead protective shield, a cylindrical drawer, and a mechanism for vertically displacing the drawer along the centre-line of the source (Figure 3.8).

The following dose points were acquired: 10, 25, 50, 75, 100, 250, 500, 750, 1000 Gy.

From this calibration, with the procedure described in Section 3.1, we derived the factor to convert the ImageJ extracted PV in dose to film.
Figure 3.9 shows the scanned images of the sample films irradiated at ISOF;
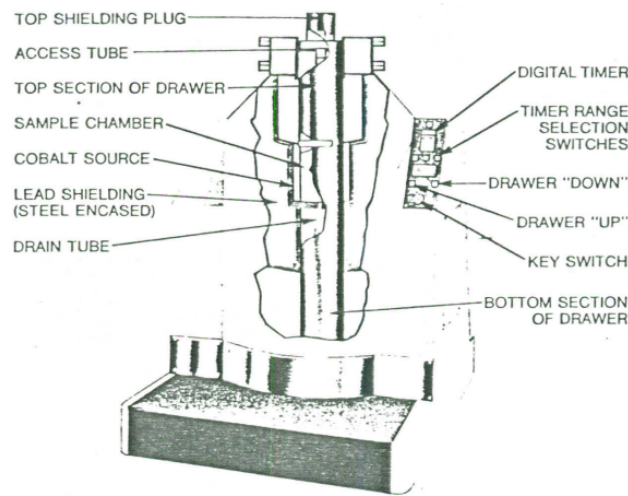
Figure 3.8: Sketch of the Gammacell220 irradiation unit used at ISOF to calibrate HD-V2 films. The sample film is positioned inside the sample chamber connected to the drawer and then lowered to the irradiation position. The ^{60}Co source consists of linear source elements equally spaced in a rack to form a radioactive cylindrical shell. *(Courtesy of Mila D'Angelantonio, ISOF-CNR Bologna)*

the samples PVs, the delivered doses and the uncertainties in both values are presented in Table 3.3.
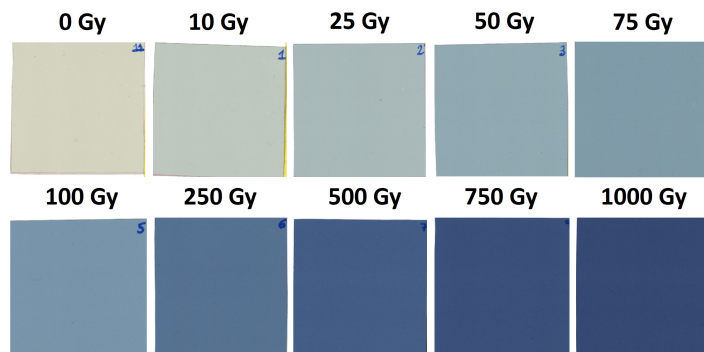
Figure 3.9: Scanned images of the Gafchromic HD-V2 films irradiated at ISOF with gamma rays from a ^{60}Co source. The targeted dose for each sample, in Gy, is also specified. The labels in the top right corner correspond to the film number in Table 3.3 and ensure that the orientation is maintained throughout the full calibration.

Film number	Dose to film [Gy]	Dose uncertainty [Gy]	PV	PV uncertainty
1	0.00	0.00	210.635	1.737
2	10.01	0.06	196.664	1.692
3	25.15	0.16	181.134	1.853
4	50.41	0.33	164.068	2.032
5	74.91	0.48	149.682	2.245
6	99.85	0.65	143.658	2.277
7	249.90	1.62	110.014	2.578
8	499.58	3.23	91.260	2.634
9	749.79	4.85	79.988	2.670
10	1000.21	6.45	73.288	2.699

Table 3.3: Summary of the doses delivered by the facility and the PVs extracted using ImageJ during each film irradiation using a ^{60}Co source at ISOF CNR Bologna. The uncertainties in both values are also included.

3.2 Characterization of the dose rate using a ionization chamber

Ionization chambers are considered the gold standard for dosimetry measurements; in our setup an IC was used as a reference to estimate the delivered dose to the cells.

To calibrate the output of the ionization chamber with respect to the delivered dose, Gafchromic films were exposed to the beam at a variety of proton current densities while recording the ionization chamber signal. To minimize uncertainties, the same dose was delivered to each film.

The irradiation was performed using the proton beam at the Bern medical cyclotron.

As previously mentioned in Section 2.5.1, the plastic flask in which the cells are contained during the irradiation significantly reduces the energy of the beam impinging on the cells. For this reason, two separate calibrations were performed at conventional rates. In the first, the flask was not included. The purpose of this calibration was to establish a basis for the response of the ionization chamber to dose rate, which could be used in a variety of applications. The second calibration took into account the additional energy loss and scattering due to the flask wall, directly measuring the beam expected at the entrance of the dose layer. This calibration was used to determine the dose delivered during the cell irradiations.
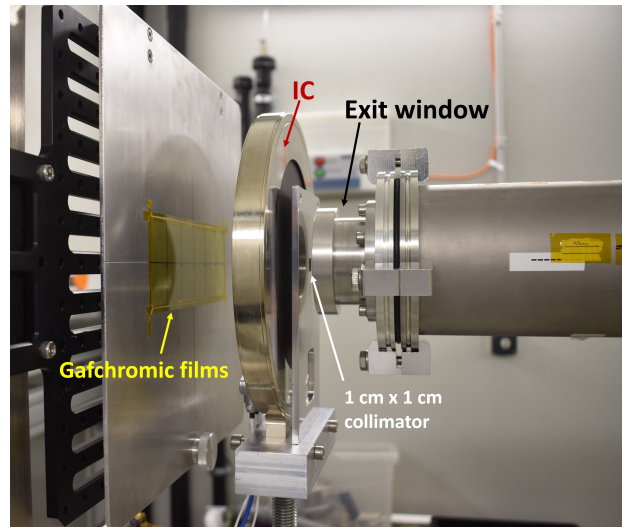
Figure 3.10: Detail of the setup for the IC characterization performed at the Bern medical cyclotron: the 1 cm × 1 cm square collimator is positioned between the exit window and the IC.

These two calibrations were performed with the EBT-3 film.

Another calibration without the flask was performed at FLASH rates using the HD-V2 films.

For the two calibrations performed without a flask, the setup was consistent with the cell irradiation setup, with the inclusion of a 1 cm × 1 cm square aluminum collimator, positioned between the exit window and the ionization chamber, as shown in Figure 3.10. Since the ionization chamber output is proportional to the total proton current while the dose rate is proportional to the proton current density, the area of the beam spot on the detector has to be taken into account when calibrating the ionization chamber. The value of the ionization chamber current was divided by the area of the beam spot on the detector for each irradiation and the parameter used for the calibration was the ionization chamber current density, measured in nA/cm^2. For the calibration in the FLASH regime, the pinhole collimator was replaced by a 4 mm aperture collimator.

Samples of Gafchromic films were mounted on a beam dump at the end of the setup as shown in Figure 3.10. The beam dump was supported by the remotely controlled stage, enabling the execution of the complete calibration procedure without entering the bunker between successive irradiations.
The air gaps between all the components have been kept consistent with those used for cell irradiations.

The dose rate on the Gafchromic films was varied by modifying the current

extracted from the cyclotron and the target delivered dose was maintained constant adjusting the exposure time.

The ionization chamber bias voltage was set at $+400$ V, as recommended by the manufacturer. The signal from the ionization chamber and the current incident on the collimator were read out in real time using electrometers controlled by a LabView program. By plotting the ionization chamber current against the collimator current, we verified the linearity of response between the collimator and the ionization chamber. The ratio of these signals strictly depends on the centering of the beam on the collimator, which can fluctuate throughout the operation of the cyclotron. Therefore, whenever possible, the ionization chamber output was used as a reference for the measurement of the delivered dose, since it represents the current incident on the cells, while the collimator current was only monitored for safety reasons.

Using the ImageJ software, we measured the mean PV value in a circular ROI of 8 mm diameter. With this value, using the inverse Green-Saunders equation (equation 3.3), we extracted the precise delivered dose for each film. This number was then divided by the irradiation time extracted from the ionization chamber signal to obtain the dose rate of each exposure.

The calculated dose rate was plotted as a function of the average ionization chamber current for each film, and fitted to extract the equation that relates the two quantities.

The scanned images of the sample films after the irradiation with conventional and FLASH dose rates are shown respectively in Figures 3.11 and 3.12. The resulting PVs extracted with ImageJ and the ionization chamber current values are presented in Tables 3.4 and 3.5. The variation of the ionization chamber current and the current on the collimator is shown in Figures 3.13 and 3.14.
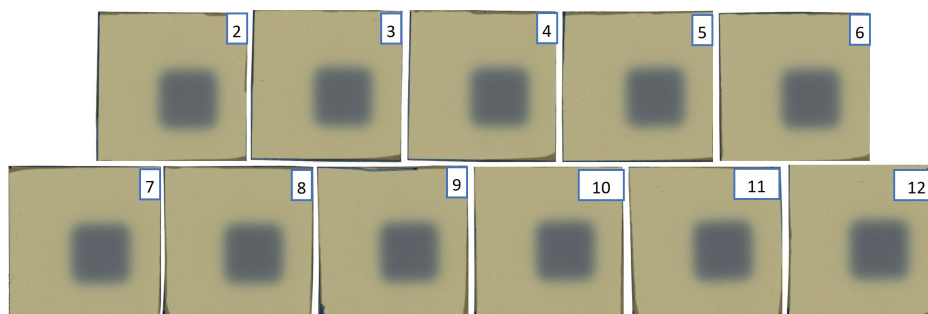
Figure 3.11: Scanned images of the Gafchromic EBT-3 films irradiated at conventional dose rates with protons produced at the Bern medical cyclotron. For this calibration, the targeted dose was approximately 4 Gy and a 1 cm $\times$ 1 cm squared collimator was used.
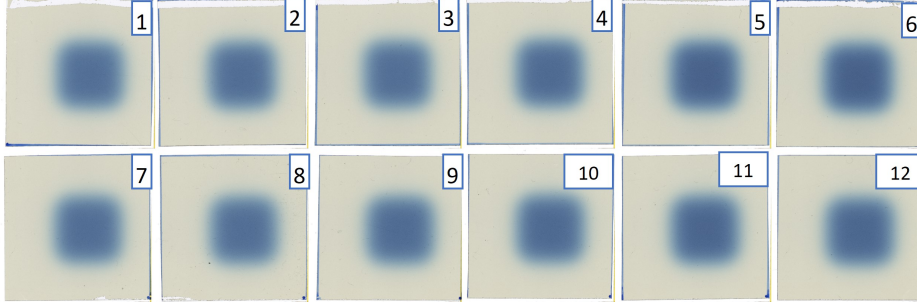
Figure 3.12: Scanned images of the Gafchromic HD-V2 films irradiated at FLASH dose rates with protons produced at the Bern medical cyclotron. For this calibration the targeted dose was approximately 500 Gy, and a 1 cm × 1 cm squared collimator was used.

Film	IC signal [nA/cm²]	PV
2	0.317	100.97
3	0.426	100.38
4	0.521	99.87
5	0.614	99.93
6	0.719	99.58
7	0.973	99.21
8	1.457	98.29
9	1.634	98.41
10	2.186	98.50
11	3.611	97.79
12	5.175	97.85

Table 3.4: Summary of the IC current densities and PVs resulting from the calibration of the IC at conventional dose rates. The film number corresponds to the label number of the films in Figure 3.11.

Film	IC signal [nA/cm²]	PV
1	232.587	113.854
2	364.094	112.453
3	451.529	113.129
4	739.513	109.919
5	1184.456	101.547
6	1482.441	99.610
7	1585.407	112.492
8	199.394	113.329
9	519.095	110.554
10	831.541	108.600
11	1305.316	104.704
12	1505.904	106.059

Table 3.5: Summary of the IC current densities and PVs resulting from the calibration of the IC at FLASH dose rates. The film number corresponds to the label number of the films in Figure 3.12.
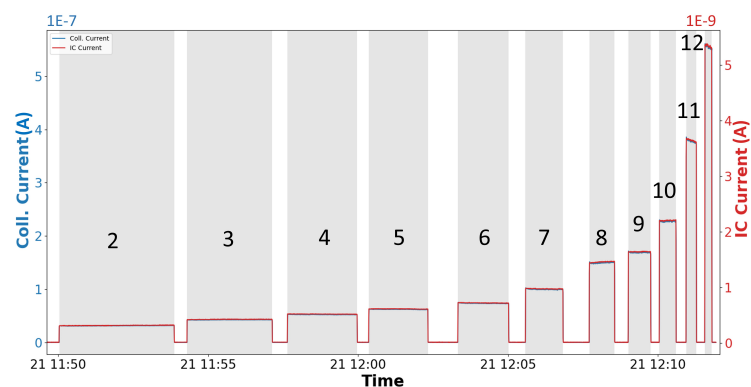
Figure 3.13: Distribution of the pinhole collimator current (in blue) and IC current (in red) over time throughout the calibration of the IC at conventional dose rates. The gray bands correspond to beam on. The number assigned to each peak corresponds to the label of the corresponding film sample in Figure 3.11.
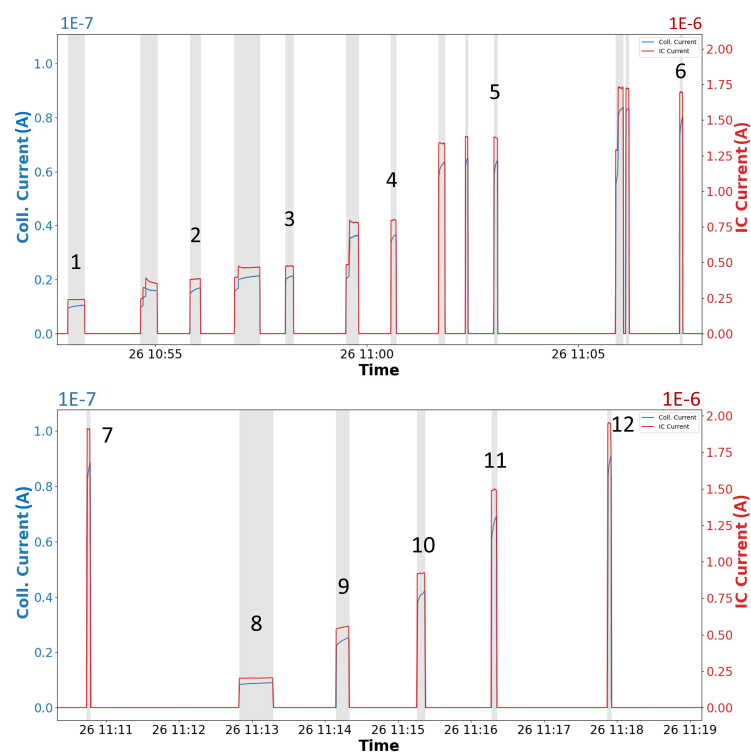
Figure 3.14: Distribution of the 4 mm collimator current (in blue) and IC current (in red) over time throughout the calibration of the IC at FLASH dose rates. The gray bands correspond to beam on. The peaks of interest are numbered with the label of the corresponding irradiated film samples in Figure 3.12.

The calibration at conventional dose rates with the flask was performed using the customized flask with a Gafchromic film taped on the inside of the frontal face, in the exact position of deposition of the cells. The setup used for this calibration is identical to the setup for the alignment check shown in Figure 2.17.

With this solution we managed to irradiate the EBT-3 films using the beam expected at the entrance of the cells layer.

The scanned images of the films irradiated during this calibration are presented in Figure 3.15 while Figure 3.16 shows the ionization chamber and collimator current ramp during the calibration. A python code was employed to extract the PV from the scanned image of the film within a customized area matching the shape of the flask. Table 3.6 reports the ionization chamber current values and the extracted PVs.
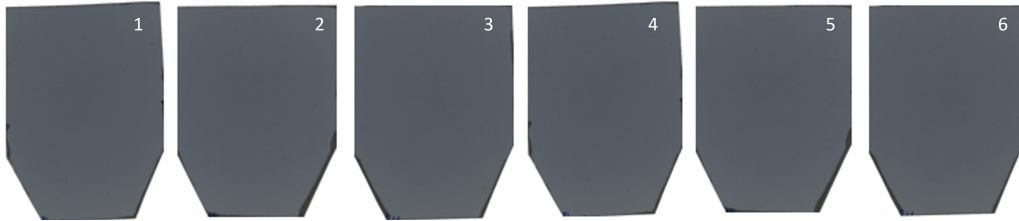
Figure 3.15: Scanned images of the Gafchromic EBT-3 films irradiated at conventional dose rates during the IC calibration with the flask. The films were taped to the inside of a flask as shown in Figure 2.17b. For this calibration, the targeted dose was approximately 4 Gy and no collimator was used in front of the IC.

Film number	IC signal [nA/cm^2]	PV
1	0.245	91.864
2	0.334	91.924
3	0.415	92.402
4	0.505	92.122
5	0.599	92.524
6	0.819	92.500

Table 3.6: Summary of the IC current densities and the PVs resulting from the calibration of the IC at conventional dose rates with the flask. The film number corresponds with the label number in Figure 3.15.
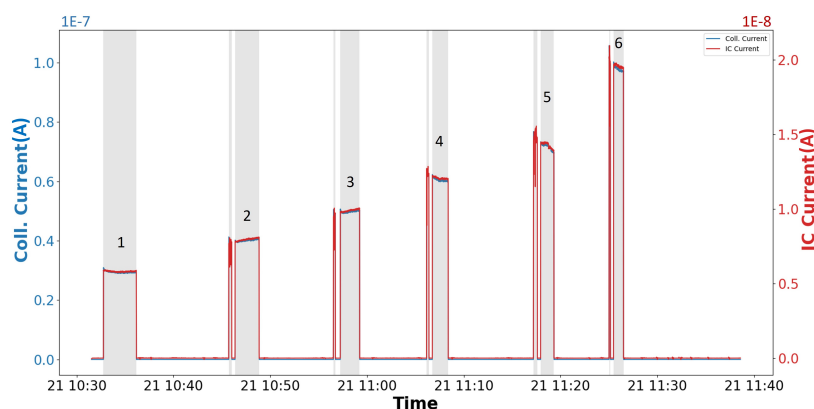
Figure 3.16: Distribution of the pinhole collimator current (in blue) and IC current (in red) over time throughout the calibration of the IC at conventional dose rates with the flask. The gray bands correspond to beam on. The peaks of interest are numbered with the label of the corresponding irradiated film samples shown in Figure 3.15.

3.3 Characterization of the dose rate using scintillating fibers

This section details the procedures and methods applied during the measurements performed at our facility to characterize the scintillating fibers discussed in Section 2.4. Given the linearity of the fibers at high dose rates, they were used to study the dose rate in the FLASH regime and to assess the saturation of the ionization chamber at FLASH rates. The response of both the PS and the GAGG, the current on the ionization chamber and the current on the collimator were recorded, varying the current extracted from the cyclotron to obtain data over a range of dose rates. The fibers signal was correlated with the dose rate of each irradiation.

To switch from conventional rates to FLASH dose rates, the collimator was changed from pinhole to larger aperture sizes. Specifically, to cover the full range of dose rates from conventional to FLASH ones, three setups were tested and the response of the ionization chamber and fibers analyzed in each case.

The three apertures are shown in Figure 3.17; the diameters are 4 mm (Figure 3.17a), 10 mm (Figure 3.17b) and 30 mm (Figure 3.17c), respectively. The scatterer placed after the collimator was the same for each aperture and comprised a $350\,\mu m$ aluminum foil.

The setup was similar to the one previously described for the ionization

(a) *4 mm aperture*   (b) *10 mm aperture*   (c) *35 mm aperture*
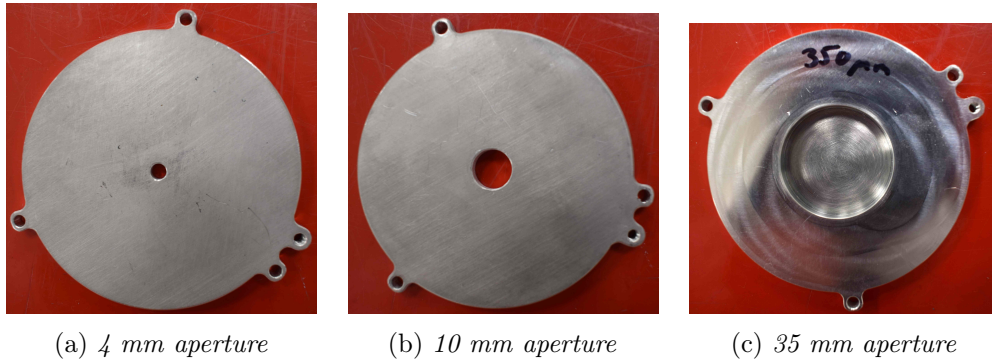
Figure 3.17: Apertures used for the calibrations at FLASH dose rates with the scintillating fibers. The diameters are (a) 4 mm, (b) 10 mm and (c) 30 mm, respectively. For the largest aperture (c), the 350 μm scatterer was implemented directly into the structure.
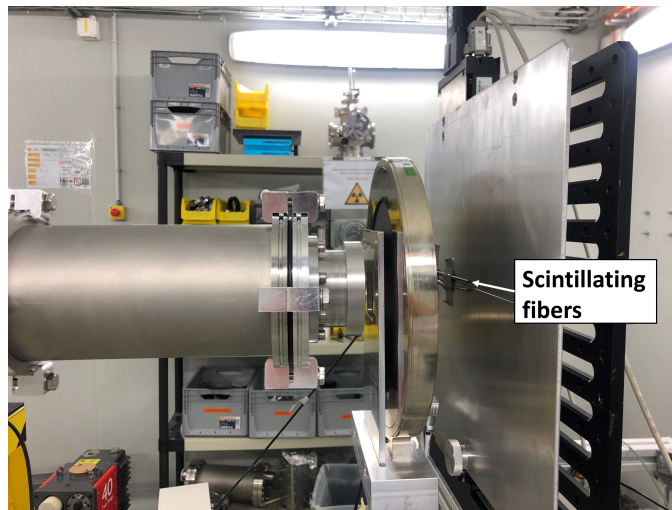
Figure 3.18: Setup for the scintillating fiber dose calibration. Both the fibers were mounted on the beam dump downstream of the IC, centered with the beam.

chamber characterization (Section 3.2). The distances between the exit window, the ionization chamber, and the beam dump were the same as for cell irradiations. Both the PS and GAGG fibers were mounted on the beam dump at the end of the setup, replacing the Gafchromic films (Figure 3.18). A square collimator of 2 cm × 2 cm was positioned before the ionization chamber to define a precise area of irradiation that was large enough to ensure both fibers were in the beam Field of View (FOV).

The optical signal from the scintillator was sent to the SPAD and readout by the Vertilon Analyzer. The very large signal of the GAGG caused the

SPAD, which has a maximum counting rate of 20 MHz [48], to saturate at high dose rates. To limit this effect, two attenuators (5.6 mm and 2.8 mm) were connected in series directly to the optical fiber before the SPAD for the test with the 10 mm aperture. The measurement with the 30 mm aperture consists of three runs acquired consecutively on the same day. In the initial set of measurements, the two attenuators were connected to the GAGG optical fiber, however the output signal of the fiber exhibited an unusual behavior and an exceptionally low signal. Therefore, the 5.6 mm attenuator was removed for the second measurement but no improvement was seen on the signal, which remained extremely low. The last set of irradiations was performed with no attenuators connected to the GAGG fiber.

The dose rate was evaluated from the ionization chamber current data using the calibration factor obtained with the procedure described in Section 3.2. The results of these measurements are analyzed in Section 4.3.2.

This study forms the basis for the future adaptation of the facility to irradiate cells with FLASH dose rates.

Chapter 4

Experimental results

In this chapter, the outcomes of our experiment, which aimed at adapting the Bern medical cyclotron facility for pre-clinical proton therapy studies, will be presented. The achieved beam uniformity and flatness following the optimization of the setup are firstly discussed, to move then to the results of the dose calibration procedure for the Gafchromic films and the characterization of the dose rate using the ionization chamber. The preliminary findings obtained during the FLASH irradiation with the scintillating fiber detectors are also discussed. Finally, the cell irradiation procedure is outlined, reviewing the main results related to the precision of dose delivery. The first preliminary survival curve of the irradiated cells, elaborated in collaboration with the Institute of Anatomy in Bern as part of a work still unpublished, is discussed.

4.1   Proton beam uniformity

One of the main goals of the optimization process, aimed at adapting the Bern medical cyclotron facility for cell irradiation, was to achieve the correct positioning of the apparatus. In particular, it was necessary to maximize the dose uniformity in the 12 cm^3 region to be irradiated (flask) and to ensure a correct alignment on the latter.

   The final setup, optimized for cell irradiation, includes a current measuring device positioned after the UniBEaM monitor. This device comprises a pinhole collimator with a 350 μm aluminum scatterer on the rear face. The instrument was connected to a long beam pipe, sealed by an exit window featuring a 50 μm aluminum scatterer.

   The alignment of the instruments with the beam was performed following

the methodology discussed in Section 2.5.2, involving two main steps. Initially, the unscattered beam was aligned with the center of the stage using Gafchromic films. This step was crucial to ensure the optimal positioning of the beam with the flask during cell irradiations. Subsequently, the scattered beam was centered within the long beam pipe using Gafchromic films until a uniform beam distribution was achieved on the film itself.

The first phase involved removing the aluminium scatter foil from behind the pinhole collimator aperture for a better visualization of the spot position. A Gafchromic film was placed on the beam stopper that was positioned on the movable stage at the end of the setup. Its center, marked with a point, was aligned with the center of the beam stopper. This point was then adjusted to coincide with the center of the cross created by the vertical and horizontal lasers of the BTL bunker.

The lasers of the bunker are aligned with the beam at the position of the collimator located after the UniBEaM. The presence of the beam pipe causes an extension in the setup of almost two meters, therefore this reference alignment position is not valid anymore. A first irradiation of the Gafchromic film (Figure 2.14) provided us with a measurement of the offset of the lasers at the flask position. The displacement of the beam center with respect to the laser center was -1.5 mm in the vertical direction and +3.5 mm on the horizontal axis. This reference position was consistently taken into account when centering the flasks for cell irradiations using the laser system.

The movable stage position was adjusted by these values and another irradiation on a Gafchromic film was performed. The final alignment result is shown in Figure 4.1. In this sample, the beam center and the film center, representing the flask center during cell irradiation, overlap, demonstrating the correct positioning.

After aligning the position of the unscattered beam with the stage, we reinserted the 350 μm thick aluminum foil distal to the pinhole collimator aperture and we proceeded with the alignment of the scattered beam. The beam distribution on a Gafchromic film was analyzed. The beam profile is represented by a 2D Gaussian distribution whose peak coincides with the center of the unscattered beam spot. To center the peak of the Gaussian with the scattered beam spot extracted from the Gafchromic film, we adjusted the position of the pipe. This adjustment was achieved by moving the support of the pipe, shown in Figure 2.5, both in the vertical and horizontal directions. After a series of tests, we achieved the result shown in Figure 4.2. The beam position, whose center is defined by the black cross, aligns perfectly with the center of the pipe (black dot) on the x-axis but is higher by 2 mm on the y-axis. This solution was validated as the final configuration and the 2 mm difference in height was considered acceptable for our application due
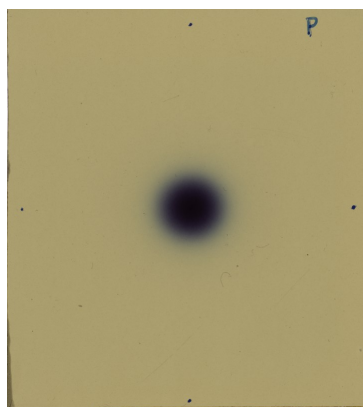
Figure 4.1: Gafchromic film irradiated within the alignment procedure to verify the positioning of the beam with the target (flask). The center of the beam spot overlaps with the target center (represented by the point in the film), indicating that the beam is correctly aligned with it.

to the shape of the flask. During cell irradiations, the flask is positioned as illustrated in Figure 2.17a, with the trapezoidal part of the container pointing downward. The most critical points that can affect the uniformity of the beam distribution on the cell layer are the angles at the top left and top right corners. Since the small vertical displacement of the beam center (Figure 4.2) was in the direction of these critical points, no further adjustments were made.

Figure 4.2, presents both the experimental horizontal (orange) and vertical (blue) beam profiles, along with their fitted curves (colored in red and green).

The resulting standard deviations are 37.35 mm for the horizontal profile, and 35.36 mm for the vertical.

The measurement was repeated for a Gafchromic film irradiated with one of the initial setups tested during the optimization procedure that comprises a $300\,\mu\mathrm{m}$ Al scatterer on the collimator and a $125\,\mu\mathrm{m}$ thick foil of aluminium at the exit window. The σ_X and σ_Y were found to be 23.89 mm and 23.32 mm, respectively.

This result defines the flatness of the profiles, which correlates with the uniformity of the beam on the spot. This study demonstrates the impact of the scatterer on the flatness of the beam. By maximizing the thickness of the scattering material at the rear face of the collimator and consequently reducing the thickness of the exit window to avoid stopping the beam, the flatness increased significantly.

With a python code the relative dose at a specific distance from the center of the distribution with respect to the dose at the center was evaluated. In
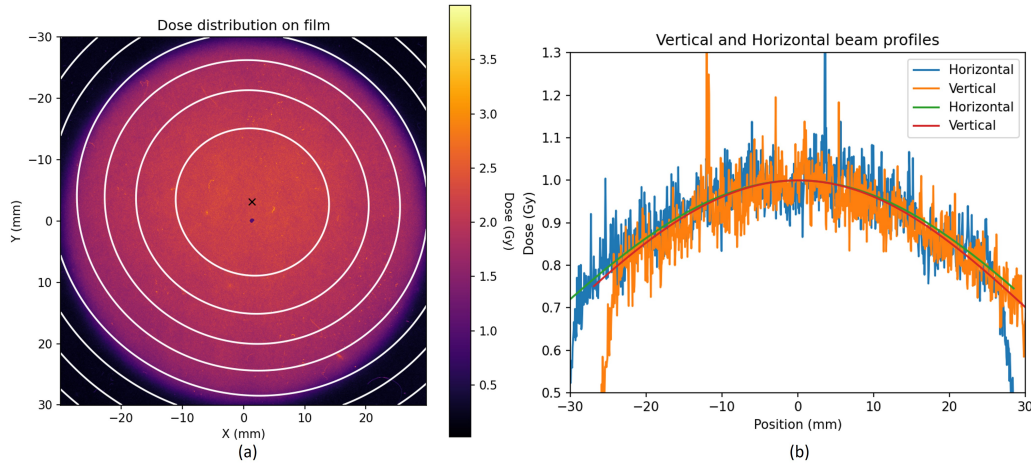
Figure 4.2: Final beam distribution resulting from the uniformity optimization. (a) Heatmap of the beam spot on the film. (b) The vertical and horizontal profiles of the dose distribution were extracted and fitted to a Gaussian.

particular, the relative dose at 20 mm from the center is 87% of the initial value. This marks an improvement over the previous setup, where the relative dose at a 20 mm radius was only 70% of the dose at the center.

This distance (20 mm) was chosen as a reference to identify variations at the boundaries of the flask, which has a dimension of 3 cm × 4 cm. This result once again quantifies the impact of the variation of the thickness of the aluminum layers in the spread of the Gaussian distribution and consequently on the uniformity of the outgoing beam. To ensure statistically valid data, it is crucial that all cells, including those located at the edges of the container, receive the same dose. Therefore, maximizing this relative dose was important.

To verify the final distribution at the cell position, we irradiated a Gafchromic film placed after the wall of the flask in which the cells are plated. The result of this analysis and the histogram of the dose distribution on the flask are presented in Figure 4.3.

The uniformity was evaluated as the ratio between the standard deviation and the mean of the dose distribution, resulting in a value of 9.26(07)%. This result meets the requirement for optimal cell irradiation defined by the Institute of Anatomy in our application, that is a uniformity smaller than 10%.

In conclusion, after multiple configurations tests to optimize the uniformity of the extracted beam, and the establishing of a multi-step alignment procedure to ensure the correct centering of the beam on the target and
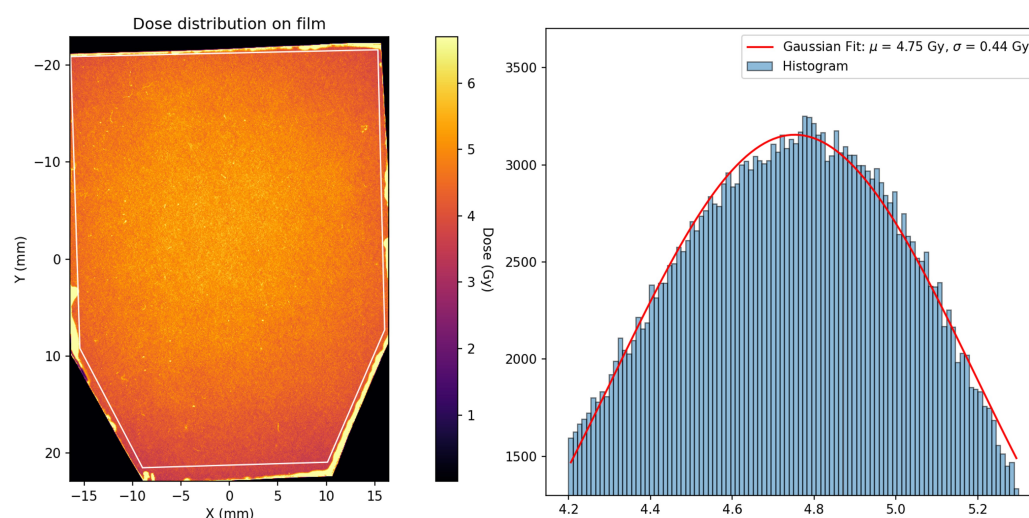
Figure 4.3: Beam distribution on the Gafchromic film positioned at the level of the cells in the flask. (a) Heatmap of the dose distribution delivered to the film. (b) Histogram of the dose distribution depicted in (a), fitted to a Gaussian. The standard deviation and the mean value of the distribution are specified in the top right corner.

within the beam pipe, an acceptable dose uniformity for our application was achieved. This result is probably close to the limit of what can be achieved at this facility.

In future, the dose uniformity could potentially be slightly improved by decreasing the size of the container of the cells thus reducing the area to be irradiated. A different solution has been identified, in particular a 1 cm radius circular flask will be tested. Furthermore, the thickness of the face of the container in which the cells are deposited can be reduced and eventually built with a different material with a smaller impact on the beam energy.

4.2 Gafchromic films dose calibration

As part of this project, Gafchromic EBT-3 and HD-V2 films were calibrated using different radiation sources with a precisely known delivered dose.

The PVs, extracted from the scanned images of the film samples, were graphically correlated to the dose delivered by the facility for each exposure. These calibration curves were then fitted using the Green-Saunders equation (3.2) and the free parameters (D_0, PV_{min}, PV_{max}, β) were extracted. Once the calibration curve of the PV as a function of the dose rate is established, it can be used to extract the dose delivered to any sample film irradiated

within the sensitive dose range by employing the inverse Green Saunders equation (3.3). This calibration curve was used to extract the dose delivered to the Gafchromic films during the irradiations performed for the beam characterization.

In the case of the EBT-3 films, two independent calibrations were performed to ensure consistent results. The first calibration used the photon beam from the clinical linac at Inselspital (described in Section 3.1.2), while the second was carried out using the ^{60}Co source at METAS (described in Section 3.1.3). The parameters derived fitting the calibration curves with equation 3.2 are presented in Table 4.1. The third row presents the parameters derived combining the data extracted from the two calibrations.

In all the following measurements performed in the context of this thesis using EBT-3 films, the combined calibration was taken as a reference to extract the dose from the PV.

In Figure 4.4, the graphical results are presented. The blue curve represents the calibration performed with the clinical linac, the green curve corresponds to the calibration at METAS and the red curve the combination of the two sets of data.

	D_0	PV_{min}	PV_{max}	β	χ^2
linac	4.99 ± 0.16	11.73 ± 2.04	168.79 ± 0.29	-0.88 ± 0.01	1.27
METAS	5.19 ± 0.25	8.45 ± 3.07	167.12 ± 0.41	-0.87 ± 0.02	1.26
combined	5.09 ± 0.32	10.13 ± 4.02	167.96 ± 0.55	-0.88 ± 0.02	2.39

Table 4.1: Parameters extracted from the fit of the calibration curve of the EBT-3 films with the Green Saunders equation (3.2). The D_0 is the abscissa of the inflection point of the sensitometric curve, PV_{min} and PV_{max} are the minimum and maximum PV, and β represents the slope of the curve.

The three curves coincide, demonstrating the accuracy of our data and the robustness of our calibration.

During the calibration at METAS, a set of Gafchromic EBT-3 films, which had expired at the beginning of the year 2023, were also irradiated. The expired films were visually slightly different in color compared to the new ones, therefore the test aimed at quantifying the influence of this change on the conversion of the PV to the delivered dose. The calibration curves for both expired and new EBT-3 films are presented in Figure 4.5.

The curve obtained from the irradiation of the expired films showed a less steep slope compared to the curve of new films, indicating a slightly reduced sensitivity to variations in dose. However, the overall difference is not significative.
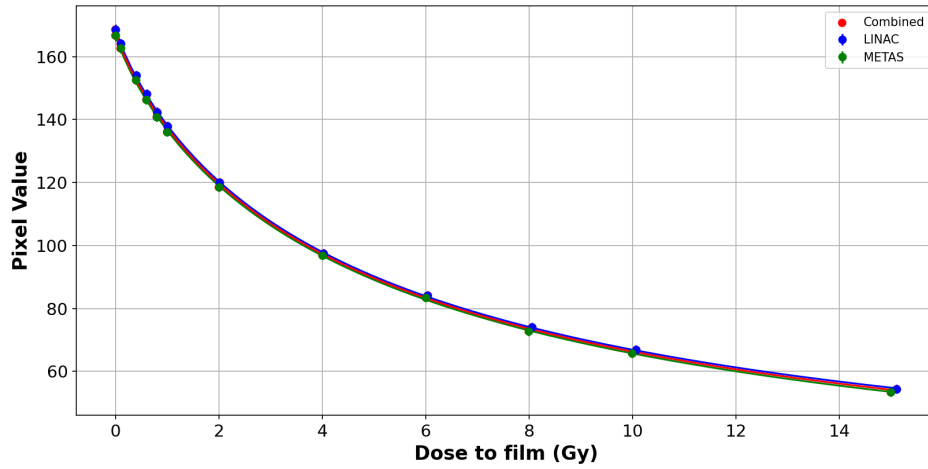
Figure 4.4: Plot of the Green Saunders fit of the calibration data from the irradiation at the clinical linac (blue) and at the METAS Institute (green). The red curve results from the combined fit of the two data sets. The error bars are smaller than the point size.
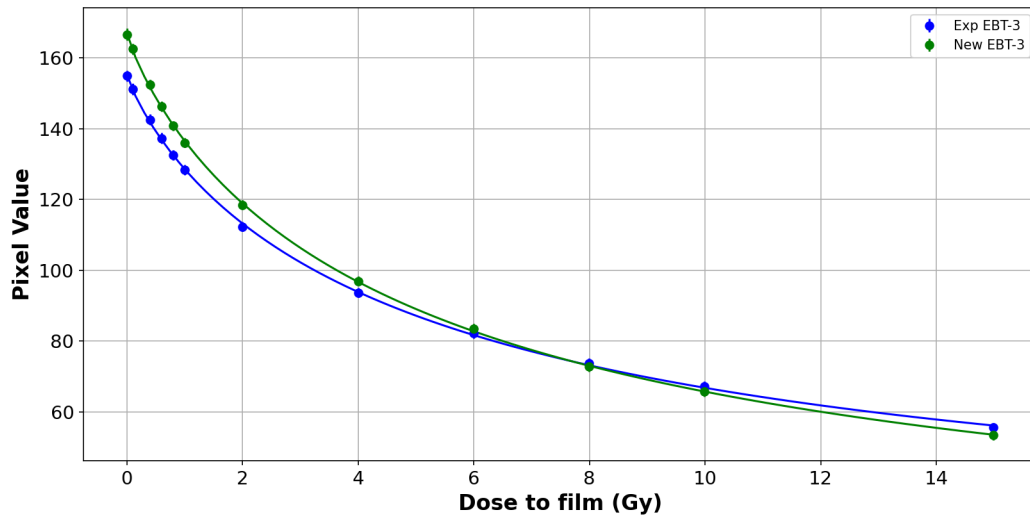
Figure 4.5: Plot of the Green Saunders fit of the calibration data from the irradiation of expired (green) and new (blue) EBT-3 films performed with a ^{60}Co source at METAS. The error bars are smaller than the point size.

The results of this test have demonstrated that the batch of Gafchromic EBT-3 films, which had expired 8 months before, remains reliable with only a slight loss in sensitivity. These films can be used in quantitative applications, but their PV should be evaluated with a recent calibration curve. The calibration of the PV relative to dose performed at METAS with these

expired films was therefore used as the new reference for this batch.

The calibration of the HD-V2 films was performed at ISOF CNR Bologna with a ^{60}Co source. The range of doses used in this calibration spanned from 10 Gy to the maximum value of 1000 Gy. This choice allowed us to employ these films in the calibration of the ionization chamber at the FLASH dose rate as well as in applications that use conventional dose rates with large delivered doses. Table 4.2 summarizes the parameters extracted using the fit.

Parameter	Value	Uncertainty
D_0	144.58	10.81
PV_{min}	47.81	4.26
PV_{max}	211.03	1.24
β	-0.85	0.04
χ^2	1.14	-

Table 4.2: Parameters extracted from the fit of the calibration curve of the HD-V2 films with the Green Saunders Equation (3.2). The irradiation was performed by ISOF-CNR Bologna using a ^{60}Co source.

The plot of the calibration curve fitted with the Green-Saunders equation (3.2) is presented in Figure 4.6.
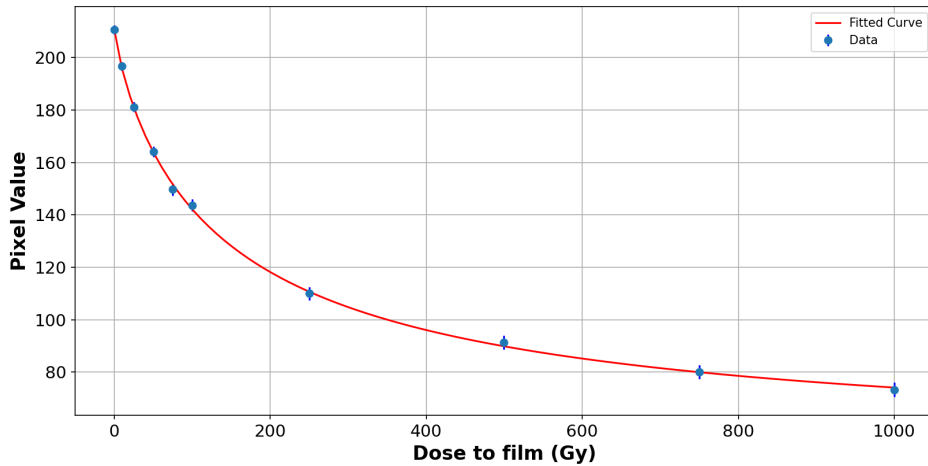
Figure 4.6: Resulting plot from the calibration of the HD-V2 films performed at ISOF CNR Bologna. The fit is performed with the Green Saunders equation (3.2).

The parameters provided above were employed in combination with the inverse Green Saunders formula during the characterization of the dose rate

using the ionization chamber, for extracting the dose delivered to the HD-V2 films (Section 4.3.1).

4.3 Characterization of the dose rate

To meet the requirements for cell irradiations, outlined in Section 2.2, it was necessary to precisely measure the dose rate employed during the irradiations themselves. The dose rate data were characterized in our facility for applications in conventional and FLASH regimes using the ionization chamber and the scintillating fibers.

The current impinging on the collimator, positioned at the beginning of the setup, was also recorded and the linearity between this variable and the ionization chamber signal was investigated.

4.3.1 Dose rate study with the ionization chamber

The current of the ionization chamber type 786 manufactured by PTW (depicted in Figure 2.8) was recorded during multiple irradiations at different dose rates. While the dose delivered to a single point on the target is independent of the area of the proton beam, the current measured by the ionization chamber is directly proportional to the total proton current incident on the detector (as mentioned in Section 3.2). Therefore, the area of the beam spot needs to be measured and taken into consideration when correlating the ionization chamber signal to the dose rate.

For consistency, the parameter used in the analysis is the chamber current density (measured in nA/cm^2); the signal was, in fact, divided by the area of the beam spot on the detector. The beam spot area was defined by the area of the exit window from which the beam exits. In some measurements, a collimator was used in front of the ionization chamber; in these cases, the beam spot area corresponded to the area of the collimator aperture.

The current density was correlated with the dose rate, obtained from the ratio of the total delivered dose and the irradiation time. The dose was extracted from the analysis of the Gafchromic films irradiated during the calibrations, using equation 3.3 with the parameters presented in Section 4.2. The irradiation time was extracted from the ionization chamber output. The uncertainty on the dose rate value was calculated using the standard error propagation, considering the error on the dose (determined by the standard deviation on the PV) and the error on the time (provided by the time resolution of the ionization chamber readout system, which was 0.6 s in our case).

Therefore the uncertainty on the dose rate depends on the irradiation time, which shortens increasing the dose rates leading to higher uncertainties in the calculated value. The uncertainty for the ionization chamber signal was considered negligible because the error on the dose rate was the dominant one.

The dose rate was characterized with the ionization chamber using three different setups. The first calibration was performed in the conventional regime with the setup for cell irradiation but without including the flask, using a 1 cm × 1 cm collimator positioned in front of the ionization chamber. This study was useful to characterize the setup for general applications (unrelated to cell irradiations).

The parameters extracted from these measurements are listed in Table 4.3 while the values of the ionization chamber signal were presented in Table 3.4. These values were used to build the plot presented in Figure 4.7. A weighted linear fit was applied to the plot, using the equation y = m·x + q and the coefficients m and q were determined. The weight of each point was defined by the value (DR error^2)$^{-1}$.

Film number	Irradiation time [s]	D [Gy]	$\dot{D}$ [mGy/s]
2	229.87	3.61 ± 0.18	15.70 ± 0.78
3	170.19	3.67 ± 0.19	21.56 ± 1.12
4	139.59	3.73 ± 0.20	26.72 ± 1.44
5	118.20	3.72 ± 0.19	31.47 ± 1.62
6	101.76	3.76 ± 0.19	36.95 ± 1.88
7	74.99	3.80 ± 0.18	50.67 ± 2.43
8	50.32	3.90 ± 0.20	77.50 ± 4.08
9	44.84	3.90 ± 0.20	86.99 ± 4.61
10	33.41	3.88 ± 0.20	116.15 ± 6.34
11	20.49	3.96 ± 0.20	193.30 ± 11.29
12	14.11	3.95 ± 0.22	279.88 ± 19.61

Table 4.3: Measured doses delivered to the films and calculated dose rates with their respective uncertainties for the calibration of the IC at conventional dose rates. The error in the irradiation time is constant (± 0.60 s), defined by the time resolution of the ionization chamber readout system.

The values of the linear fit parameters are reported in Figure 4.7. The slope is denoted by the letter 'm', and the intercept is denoted by the letter 'q'. The reduced Chi-squared ($\tilde{\chi}^2$) was found to be 2.14 × 10^{-2}, indicating a good fit of the experimental data to the theoretical model.
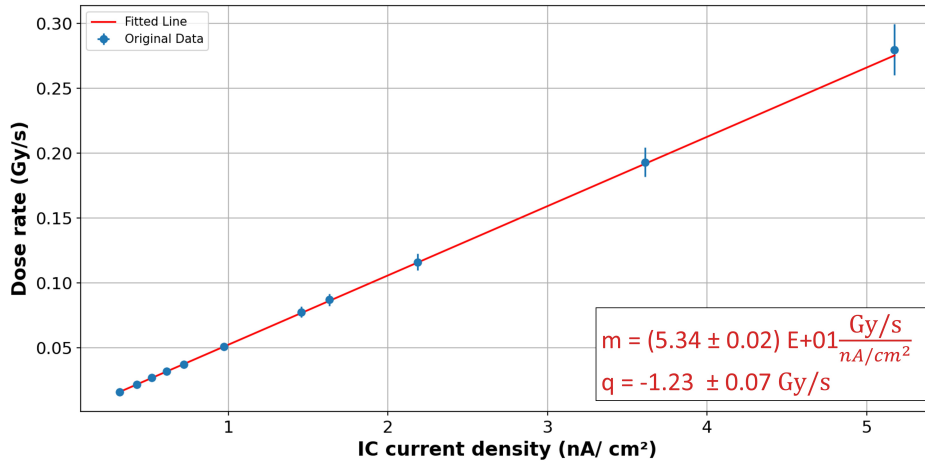
Figure 4.7: Plot illustrating a weighted linear fit applied to the data of IC current density vs dose rate. The data are derived from the calibration of the IC at conventional dose rates (Table 4.3).

In the second set of measurements, the flask was added at the end of our setup in the reference position for cell irradiations. In this study, no collimator was used at the ionization chamber, and the size of the beam spot on the surface of the detector was defined by the area of the exit window, namely 23.75 cm^2. The ionization chamber current density, shown in Table 3.6, was calculated using the ratio of the current to the area of 23.75 cm^2. The parameters extracted with this test are presented in Table 4.4. The plot in Figure 4.8 shows a weighted linear fit applied to the experimental data; the weights were evaluated as (DR error^2)$^{-1}$.

Film number	Irradiation time [s]	D [Gy]	$\dot{D}$ [mGy/s]
1	203.70	4.69 $\pm$ 0.44	23.04 $\pm$ 2.16
2	149.18	4.69 $\pm$ 0.43	31.41 $\pm$ 2.89
3	119.68	4.62 $\pm$ 0.45	38.62 $\pm$ 3.77
4	98.44	4.66 $\pm$ 0.43	47.33 $\pm$ 4.38
5	81.75	4.61 $\pm$ 0.44	56.34 $\pm$ 5.40
6	61.39	4.61 $\pm$ 0.39	75.07 $\pm$ 6.40

Table 4.4: Measured doses delivered to the films and calculated dose rates with their respective uncertainties for the calibration of the IC at conventional dose rates with the flask. The error in the irradiation time is constant ($\pm$ 0.60 s) and is defined by the time resolution of the ionization chamber readout system.
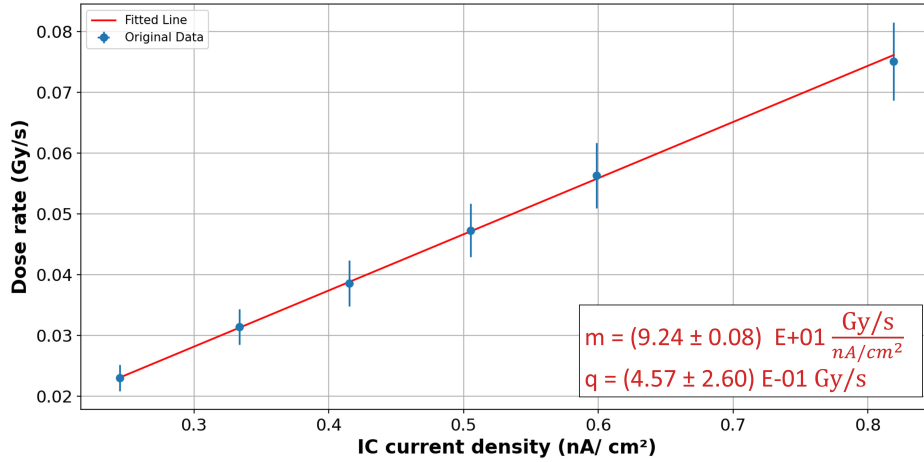
Figure 4.8: Plot illustrating a weighted linear fit applied to the data of IC current density vs dose rate. The data are derived from the calibration of the IC at conventional dose rates with the flask (Table 4.4).

The fitting parameters are presented in Figure 4.8; the $\tilde{\chi}^2$ is 1.15×10^{-2} demonstrating a good agreement between the experimental data and the theoretical ones. The equation defining this line was used in this project to determine, based on the current density, the value of the dose rate provided during the irradiation of cells.

In both Figures 4.7 and 4.8, the errors on the data increase with the dose rate. This is attributed to the dependence of the uncertainty on the irradiation time, which decreases as the dose rate increases.

As described in Section 2.3, our setup comprises a current measuring device composed of a collimator electrically isolated from the beam pipe thanks to a plastic ring. The collimator can be connected to a wire to measure the current that is deposited into it. Since the structure is not actively cooled, the signal from the collimator had to be recorded for safety reasons, to ensure that the radiation did not cause damage to the plastic part.

The ionization chamber works as an in-beam monitoring device, directly measuring the total current of the incident proton beam on the target. In contrast, the current on the collimator indicates the rate of protons that do not pass through the collimator aperture. The recorded collimator current was correlated with the ionization chamber current density and fitted linearly. This second analysis aimed at establishing a reliable dose rate readout system based on the collimator current, suitable for applications that are incompatible with the characteristics of the ionization chamber. An example of such a case is represented by the irradiations performed with dose rates

that cause the saturation of this detector.

The plot in Figure 4.9 shows a weighted linear fit applied to the values of the ionization chamber current density as a function of the pinhole collimator current, recorded during the irradiations at conventional dose rates. The weights were evaluated as (Coll. current error^2)$^{-1}$. A constant uncertainty of ± 1.10 was assigned to the collimator current, which is representative of the standard deviation of the measured current while the beam is on. This value was extracted from the collimator current measurements in Figures 3.13 and 3.16 and was applied to all points in the calibrations.

The line in blue is representative of the calibration performed without the flask, while the yellow line is the irradiation with the flask included in the setup. The fitting parameters that define the two lines, the slope m and the intercept q, are presented in the inset of the figure.
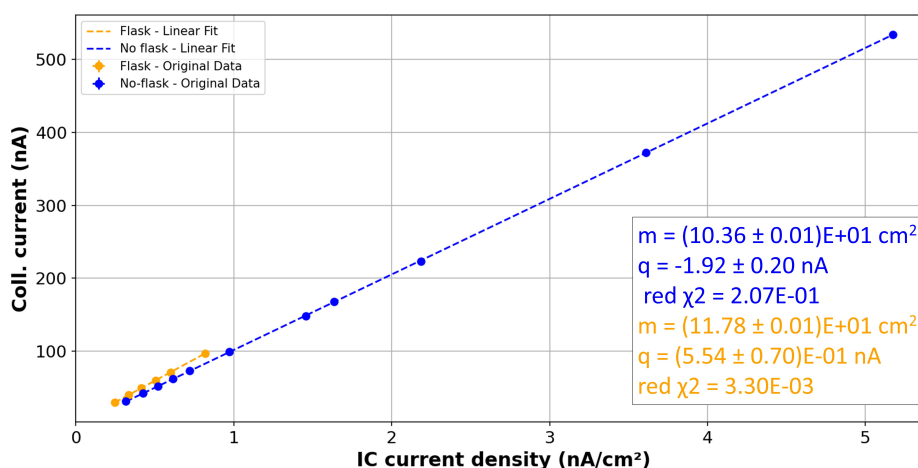
Figure 4.9: Plot illustrating a weighted linear fit applied to the data of IC current density vs pinhole collimator current. The data are derived from the calibration of the IC at conventional dose rates without the flask (blue) and with the flask (yellow). The error bars are smaller than the point size.

The 1 cm^2 collimator at the ionization chamber was removed for the calibration with the flask and the difference in the beam spot area was taken into account when calculating the current density. Since the collimator and the ionization chamber had undergone no other changes during the two irradiations, the lines were expected to coincide.

The current on the collimator is directly proportional to the dose rate as long as the position and shape of the beam do not change. In fact, this change would cause a variation in the portion of the beam that is absorbed in the collimator. Therefore the current is significantly influenced by the geometry of the proton beam emerging from the cyclotron. For instance, the bending

magnet parameters, which can be slightly different between irradiations, can affect this value. The slight variation in slope between the two lines may be a result of this effect.

This finding demonstrates that the relationship between the current density in the ionization chamber and the current on the collimator, constituting the current measuring device, is linear, but it may not be constant during different sets of exposures. Due to these reasons, whenever possible the ionization chamber current density is used as a reference for dose rate rather than the collimator current.

An additional calibration was performed at high dose rates to study the linearity of the ionization chamber in this regime. The ionization chamber exhibits a relatively slow response and tends to saturate at elevated dose rates, and this characteristics precludes its use as a detector for FLASH irradiations without any correction [22].

The irradiation was performed using a 1 cm × 1 cm collimator in front of the ionization chamber, defining the area of the spot on the detector. The time and dose values extracted from the calibration are presented in Table 4.5; the ionization chamber current density was described in the previous chapter in Table 3.5.

Film number	Irradiation time [s]	D [Gy]	$\dot{\text{D}}$ [Gy/s]
1	24.44	256.02 ± 25.00	10.48 ± 0.96
2	15.34	263.23 ± 25.44	17.16 ± 1.05
3	11.91	257.25 ± 24.46	21.60 ± 1.79
4	7.79	287.99 ± 28.97	36.97 ± 2.32
5	5.80	372.82 ± 38.79	64.26 ± 2.97
6	4.64	394.94 ± 41.93	85.10 ± 4.68
7	3.14	262.68 ± 26.40	83.74 ± 5.65
8	27.97	258.96 ± 26.15	9.26 ± 9.43
9	10.91	280.12 ± 28.50	25.68 ± 11.85
10	6.93	297.26 ± 29.53	42.89 ± 18.09
11	4.66	335.81 ± 34.39	72.03 ± 14.24
12	3.64	320.92 ± 32.29	88.29 ± 17.07

Table 4.5: Measured doses delivered to the films and calculated dose rates with their respective uncertainties for the calibration of the IC at higher dose rates. The error in the irradiation time is constant (± 0.60 s) and is defined by the time resolution of the ionization chamber readout system.

In the last three points acquired with the higher dose rate, the irradiation

lasted for a shorter time. The uncertainty in time significantly contributes to the error in these last points, making it difficult to determine whether the ionization chamber is saturating or not. Since the ionization chamber was expected to saturate in this irradiation, a weighted second order polynomial fit with the equation $y = a \cdot x^2 + b \cdot x + c$ was applied to the experimental data. The resulting plot is shown in Figure 4.10; the weight of the points was defined as $(DR\ error^2)^{-1}$.
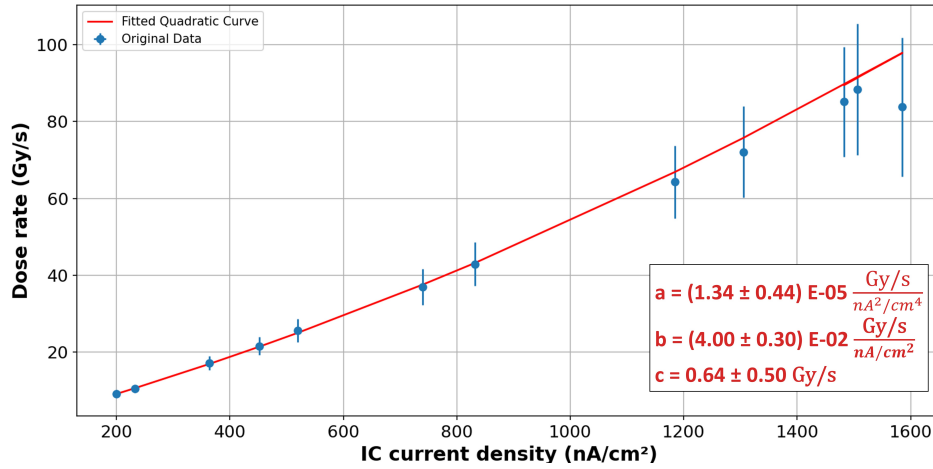
Figure 4.10: Plot illustrating a weighted second order polynomial fit applied to the data of the IC current density vs the dose rate. The data are derived from the calibration of the IC at high dose rates (Table 4.5).

The coefficients a, b, and c defining the curve of the fit are displayed in the lower right corner of Figure 4.10; the parameter $\tilde{\chi}^2$ for the curve is 1.15×10^{-1}.

In the irradiation performed at higher dose rates, a 4 mm collimator replaced the pinhole collimator. The linearity of the ionization chamber signal as a function of the collimator current was measured; a weighted linear fit of the experimental data is shown in Figure 4.11. The weights were evaluated as $(Coll.\ current\ error^2)^{-1}$. A consistent uncertainty of ± 1.66 was attributed to the collimator current, that is representative of the standard deviation of the measured current during beam operation. This value was derived from the measurement presented in Figure 3.14 and was applied to all the calibration points.

Due to the larger aperture of the collimator, a smaller portion of the beam is stopped by the instrument compared to the portion that passes through. This solution was implemented to achieve higher dose rates. As a result, the current recorded by the current measuring device, generated by

the beam absorbed by the collimator, is smaller than the current measured by the ionization chamber that corresponds to the portion of the beam that emerges from the beam pipe.
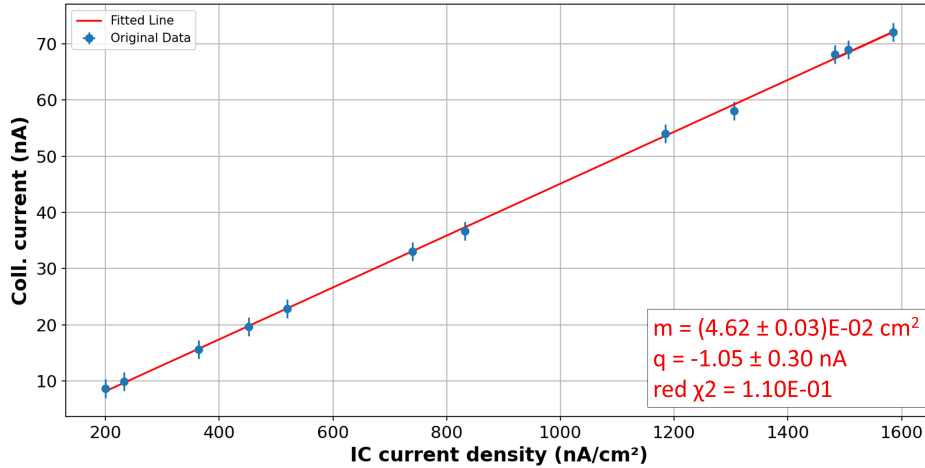
Figure 4.11: Plot illustrating a weighted linear fit applied to the data of IC current density vs 4 mm collimator current. The data are derived from the calibration of the IC at high dose rates.

The plot in Figure 4.11 demonstrates that the ionization chamber is linear in the whole range tested. The ionization chamber current density values coincide with those used in the plot presented in Figure 4.10. This outcome provides crucial information; the points on the plot are well represented by a linear model. This information contradicts the idea of the ionization chamber saturation deriving from the analysis of the experimental points in Figure 4.10.

This second analysis confirmed that the detector accurately recorded signals at dose rates up to 88 Gy/s. For future applications, a data acquisition system with an improved temporal resolution will be employed to determine the behavior of the ionization chamber, in order to minimize the uncertainty in the detector signal.

In order to define a single equation for the dose rate calculation, the two sets of data presented in Table 4.3 and Table 4.5, acquired using conventional and FLASH dose rates, were analysed together.

A weighted linear fit and a weighted second order polynomial fit were applied to the same experimental data to determine the most suitable model. The weighted linear fit used the equation $y = m \cdot x + q$ with weights determined by the value $(\text{DR error}^2)^{-1}$. In the case of the polynomial fit the equation $y = a \cdot x^2 + b \cdot x + c$ was used and the weight of each point was

calculated as $(\text{DR error})^{-1/2}$.

At first the weight in the polynomial fit was measured following the same procedure used for the linear fit using the value $(\text{DR error}^2)^{-1}$. However in this measurement, the large dataset and the significant variation in the errors from the initial to the final experimental point resulted in the fit being extremely influenced by conventional data with a very small uncertainty.

To improve the accuracy of the fit in order to correctly represent the values at higher dose rates, the weighting of the error was adjusted and the square root of the error was used.

In Figure 4.12, the second order polynomial fit (red) and the linear fit (orange) applied to the experimental data are presented. In the top left corner of the figure, a detailed view is shown, focusing only on the data from the calibration at the conventional dose rates. This image provides information about the approximation of the two models in the first set of measurements. Observing the plot in Figure 4.12, it is evident that the orange line adequately covers most of the points, while the red curve does not correctly represent the points at conventional dose rates.
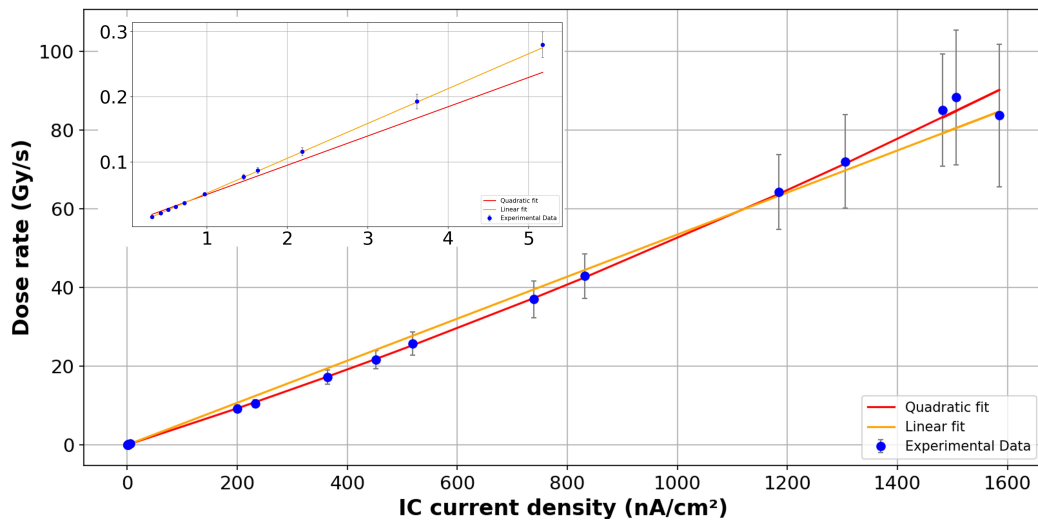
Figure 4.12: Comparison of the results obtained applying a weighted second-order polynomial fit (red) and a weighted linear fit (orange) to the experimental data for both conventional and high dose rate calibrations of the IC. The conventional points condense in just one point therefore a zoom of this region is shown on the top left corner.

The data were better fitted with the linear fit, yielding a $\tilde{\chi}^2$ of 0.47, rather than with the polynomial fit, which produced a $\tilde{\chi}^2$ of 2.78. Therefore, the linear fit was selected as the preferred model to fit these experimental data.

The equation that defines the line is:

$$y = (5.34 \pm 0.10)\mathrm{E}{-}02 \cdot x - (-1.23 \pm 0.05)\mathrm{E}{-}03 \qquad (4.1)$$

This formula was used as a reference for all the irradiations performed at our facility using the ionization chamber. This relationship was used throughout the project to characterize the fiber signal as a function of the dose rate.

For future applications, an additional characterization will be performed in the interval between 0.3 Gy/s and 9 Gy/s to accurately complete the plot by including the missing points.

4.3.2 Dose rate study with the scintillating fibers

The detection system based on scintillating fibers, described in Section 2.4, was tested at our facility to characterize the dose rate from the conventional to the FLASH regime. Two fibers were tested in our laboratory, one was based on a plastic scintillator (PS) while the other was a Gadolinium Aluminium Gallium Garnet fiber doped with Cerium (GAGG).

In this experiment we chose to derive the dose rate value from the ionization chamber current density using the calibration curve established in Section 4.3.1, instead of irradiating Gafchromic films. This decision was influenced by the need to position the fibers on the stage instead of the films, replicating the flask position during the cell irradiations. The characterization aimed at defining a relationship between the signal of the scintillating fibers and the dose rate in the FLASH regime for the specific application of pre-clinical studies with the cells. Therefore, the dose rate has to be characterized according to the tested apparatus and to the specific location of the cells.

The signal of the fibers, expressed in counts per second, was initially correlated with the ionization chamber current density to ensure linearity in the response to the delivered beam. The ionization chamber was calibrated with a 1 cm × 1 cm collimator in front of the detector while the irradiation of the fibers was performed with a 2 cm × 2 cm collimator. To account for the effective area used in this study with the fibers, the ionization chamber current had to be scaled accordingly.

Once the linearity of the fibers response was verified, the dose rate was further correlated with the signals from the PS and the GAGG. The value of the dose rate was extracted from the ionization chamber current density using equation 4.1.

Three sets of data were acquired with three different setups employing various collimator apertures (4 mm, 10 mm and 30 mm).

The parameters resulting from the primary experiments with the three different collimator apertures have been analysed as a whole. The signal from the fibers, recorded by the Vertilon readout system, and the dose rate for each irradiation are presented in Table 4.6.

N°	IC signal [nA/cm^2]	PS counts/s	GAGG counts/s	$\dot{D}$ [Gy/s]
1	1.27	6.01E+03 $\pm$ 6.22E+01	8.78E+05 $\pm$ 8.47E+02	0.07 $\pm$ 0.00
2	1.39	5.83E+03 $\pm$ 6.78E+01	9.29E+05 $\pm$ 1.03E+03	0.07 $\pm$ 0.00
3	2.78	6.10E+03 $\pm$ 7.33E+01	1.83E+06 $\pm$ 1.51E+03	0.15 $\pm$ 0.00
4	4.91	6.38E+03 $\pm$ 6.78E+01	3.26E+06 $\pm$ 1.87E+03	0.26 $\pm$ 0.00
5	29.89	9.85E+03 $\pm$ 1.37E+02	1.74E+07 $\pm$ 6.70E+03	1.60 $\pm$ 0.01
6	54.05	1.37E+04 $\pm$ 1.59E+02	-	2.89 $\pm$ 0.12
1	10.20	7.10E+03 $\pm$ 7.00E+01	1.34E+04 $\pm$ 9.89E+01	0.54 $\pm$ 0.00
2	18.79	8.01E+03 $\pm$ 8.44E+01	1.98E+04 $\pm$ 1.30E+02	1.00 $\pm$ 0.00
3	48.59	1.10E+04 $\pm$ 8.33E+01	4.29E+04 $\pm$ 1.67E+02	2.60 $\pm$ 0.01
4	160.22	2.47E+04 $\pm$ 2.19E+02	1.38E+05 $\pm$ 5.43E+02	8.56 $\pm$ 0.02
5	411.75	5.10E+04 $\pm$ 2.54E+02	3.37E+05 $\pm$ 6.60E+02	22.00 $\pm$ 0.05
6	700.63	8.11E+04 $\pm$ 4.12E+02	5.55E+05 $\pm$ 1.11E+03	37.44 $\pm$ 0.08
1	1.15E+03	2.84E+06 $\pm$ 1.06E+04	1.50E+05 $\pm$ 1.17E+03	61.36 $\pm$ 0.13
2	1.74E+03	4.26E+06 $\pm$ 9.88E+03	2.25E+05 $\pm$ 1.68E+03	93.20 $\pm$ 0.20
3	2.01E+03	4.80E+06 $\pm$ 1.91E+04	2.50E+05 $\pm$ 1.93E+03	107.22 $\pm$ 0.23
4	2.77E+03	6.61E+06 $\pm$ 9.76E+03	3.43E+05 $\pm$ 2.11E+03	148.15 $\pm$ 0.32
5	3.77E+03	8.98E+06 $\pm$ 9.35E+03	4.63E+05 $\pm$ 1.99E+03	201.50 $\pm$ 0.44
6	4.74E+03	1.11E+07 $\pm$ 1.52E+04	5.73E+05 $\pm$ 2.55E+03	253.24 $\pm$ 0.55
7	5.94E+03	1.37E+07 $\pm$ 6.87E+04	7.09E+05 $\pm$ 4.76E+03	317.69 $\pm$ 0.69

Table 4.6: Parameters extracted from the calibration of the fibers using the (top) 4 mm aperture collimator, (middle) the 10 mm aperture collimator, (bottom) the 30 mm aperture collimator. In the sixth irradiation of the first set, the GAGG large signal caused the saturation of the SPAD, therefore no value of the count rate is reported.

In the sixth row of the first set, the GAGG count rate is not reported due to a saturation issue with the SPAD caused by the large signal from the GAGG fiber. This initial saturation case provided us with information about the need for an attenuator to proceed with higher dose rates. After a series of tests to find the best solution, 5.6 mm and 2.8 mm attenuators were used for the second set of measurements with the 10 mm aperture.

In the study with the 30 mm collimator aperture, three sets of data were

acquired consecutively using different attenuators. In the first run, both the 5.6 mm and 2.8 mm attenuators were connected to the GAGG optical fibers, following the procedure used in the previous measurement with the 10 mm aperture. However, the GAGG signal resulted extremely low. Consequently, for the second measurement, the 5.6 mm attenuator was removed. Since there was no improvement in the fiber output, the third set of measurements was performed with no attenuators. The section that refers to the 30 mm collimator measurement only displays the third set of data within the dose rate range where the signal from both fibers was linear.

The extracted dose rate was graphically correlated with the fiber count rate. A linear fit was applied to the experimental data and the equation of the resulting line was derived. Figure 4.13 shows the plots of the fibers output for the irradiations performed with the three different collimators along with the linear fit.

The signal of both fibers is linear in all the different experiments, from conventional to FLASH rates. The parameters extracted from the linear fit of the experimental data, namely the slope, the intercept and the R^2, are presented for both the fibers in Table 4.7.

PS			
SET	Slope [Gy^{-}1]	Intercept [s^{-}1]	R^2
4 mm	2.74E+03 $\pm$ 5.75E+01	5.68E+03 $\pm$ 7.70E+01	0.9983
10 mm	2.01E+03 $\pm$ 2.25E+01	6.29E+03 $\pm$ 4.07E+02	0.9995
30 mm	4.25E+04 $\pm$ 3.89E+02	2.89E+05 $\pm$ 7.37E+04	0.9996
GAGG			
SET	Slope [Gy^{-}1]	Intercept [s^{-}1]	R^2
4 mm	1.07E+07 $\pm$ 1.12E+05	2.47E+05 $\pm$ 8.17E+04	0.9968
10 mm	1.48E+04 $\pm$ 1.33E+02	6.96E+03 $\pm$ 2.42E+03	0.9997
30 mm	2.18E+03 $\pm$ 1.37E+01	1.84E+04 $\pm$ 2.59E+03	0.9998

Table 4.7: Parameters resulting from the linear fit applied to the data of the PS and GAGG count rate as a function of the dose rate for the calibrations performed with the 4 mm aperture, 10 mm aperture and 30 mm aperture.

The PS signal is significantly lower with respect to the GAGG signal in plot (a) and plot (b) of Figure 4.13. This behaviour is due to the smaller light yield of the plastic scintillator, previously mentioned in Section 2.4.

In the case of the 30 mm measurement, looking at the Table 4.6, it is possible to see that the PS counts/s increase significantly compared to the
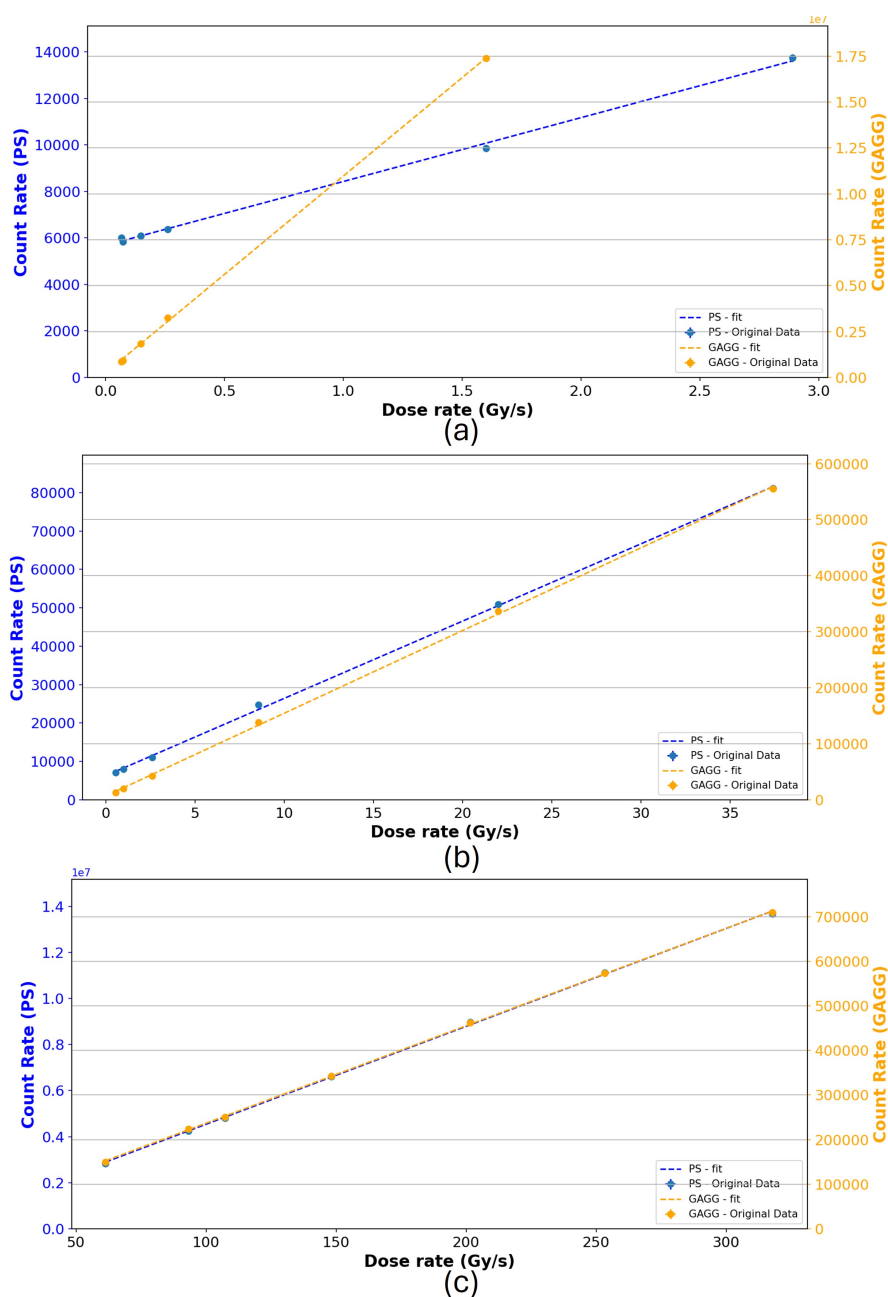
Figure 4.13: Linear fit of the PS (blue) and GAGG (yellow) count rates as a function of the dose rate for the three data acquisition performed with the (a) 4 mm aperture collimator, (b) the 10 mm aperture collimator and (c) the 30 mm aperture collimator. The x-axis is the dose rate expressed in Gy/s. The error bars are smaller than the point size.

previous measurements. In particular, when compared to the previous set of measurements, doubling the dose rate increases the signal by two orders of magnitude. This evidence suggests that the detection system might be reaching its maximum capacity to accurately measure and process signals at higher dose rates.

Regarding the GAGG fiber, the difference in the order of magnitude of the counts/s when going from plot (a) to (b) is due to the attenuators added to the setup. In the case of the third plot, no attenuators were used, but the signal is of the same order of magnitude as the previous set of measurements. Since the dose rate used in this last measurement was significantly higher, the signal was expected to grow accordingly. This outcome suggests that the fiber might have been damaged before this measurement.

In the case of the 30 mm aperture, three consecutive irradiations at FLASH dose rates were performed. In the first and in the second irradiation, the GAGG extremely low signal was comparable to the noise in the no beam condition. Since it was not possible to correlate the signal to any specific trend, these measurements were not considered reliable for the analysis. The third set of irradiations, performed without the attenuators, registered the signal presented in the last section of Table 4.6.

A final test was performed using the same setup, aimed at testing the GAGG fiber at really high dose rates up to 2500 Gy/s. In Table 4.8 the dose rates and the GAGG signal recorded with this measurement are presented. The two sets of measurements for the GAGG fiber calibration with the 30 mm aperture collimator have been analysed as a whole and a plot of the fiber count rate as a function of the dose rate is presented in Figure 4.14. The experimental data were correlated to a second order polynomial fit and a linear fit. The extracted parameters for both models are presented in the inset of the figure.

As previously mentioned, the GAGG fiber was suspected to have been damaged during this last set of irradiations due to an extremely low signal. However, the response of the fiber was found to be linear even in the last irradiation (Figure 4.13(c)). Given this evidence, the data have been analyzed for a qualitative measurement to investigate the saturation of the ionization chamber.

The experimental data align well with the linear model only in the range from 60 Gy/s to 1000 Gy/s. Beyond this threshold, the dose rate growth starts to decrease, while the signal from the fiber continues to increase. As the dose rate is extracted from the ionization chamber, we suspected that this detector was losing its linearity. To confirm that the curve was indeed due to the saturation of the ionization chamber, an additional polynomial fit was applied to the plot of the fiber count rate against the ionization chamber

N°	IC signal [nA/cm^2]	GAGG counts/s	$\dot{D}$ [Gy/s]
1	9.11E+03	1.08E+06 ± 4.08E+03	486.84 ± 1.06
2	1.25E+04	1.54E+06 ± 4.38E+03	667.51 ± 1.45
3	1.59E+04	1.96E+06 ± 4.85E+03	851.34 ± 1.85
4	1.56E+04	1.90E+06 ± 5.41E+03	833.27 ± 1.81
5	1.85E+04	2.27E+06 ± 5.55E+03	987.79 ± 2.14
6	3.03E+04	3.98E+06 ± 9.28E+03	1621.13 ± 3.52
7	4.61E+04	6.40E+06 ± 1.15E+04	2464.23 ± 5.34

Table 4.8: Parameters extracted from the calibration of the GAGG fiber with the 30 mm aperture collimator.
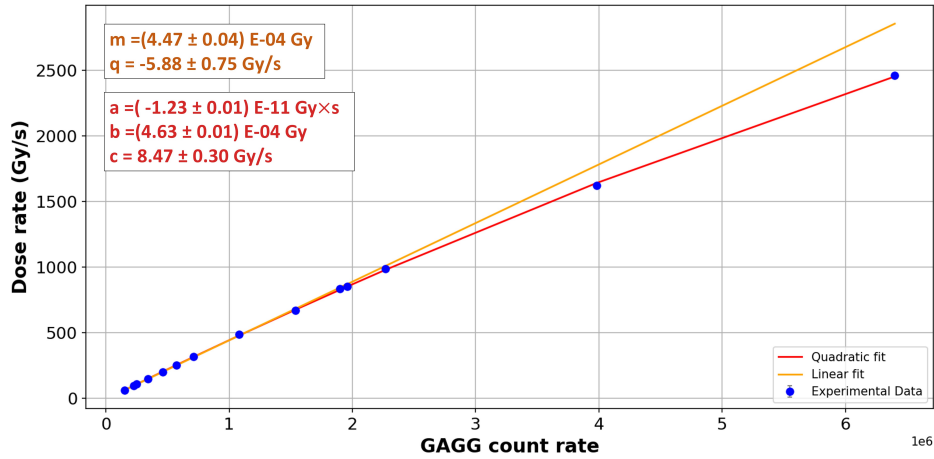
Figure 4.14: Plot illustrating a second order polynomial fit and a linear fit applied to the data of the GAGG count rates as a function of the dose rate for the 30 mm collimator calibration. The parameters extracted from the two models are presented in the upper left corner of the figure. The error bars are smaller than the point size.

current density (Figure 4.15). The plot in Figure 4.15 shows a behavior similar to that of the dose rate, confirming the saturation of the ionization chamber.

Additional experiments with a new set of fibers are required to validate the accuracy of the obtained results.

The unusual behavior of the GAGG fiber observed during the tests with the 30 mm aperture was suspected to result from radiation damage. Previous works showed that the scintillator is resistant enough to radiation: a loss of trasmission of 3.6% can be seen after an irradiation of the GAGG fiber of
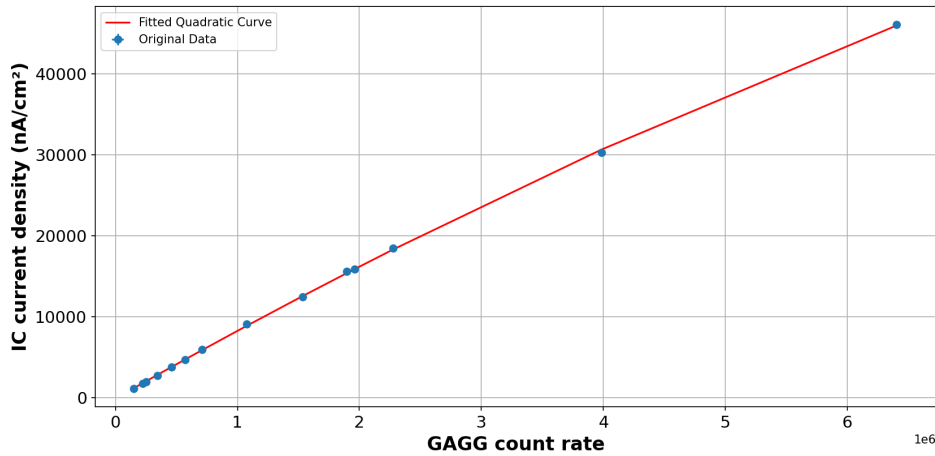
Figure 4.15: Plot of the ionization chamber current density as a function of the GAGG count rate for the full set of data acquired with the 30 mm aperture collimator. A weighted polynomial fit was applied to the experimental data, the error bars are smaller than the point size.

900 kGy [73], [74]. Given that the GAGG detector was employed in several measurements at high dose rates, the delivered dose to the fiber is expected to be comparable or even higher than this threshold.

However, radiation damage alone may account for only a minor change in the signal, suggesting additional factors. Two potential causes for this signal reduction were identified: physical damage to the fiber or signal loss in the mechanical connection between the scintillator and the optical fiber itself, or a combination of both. In future, new set of fibers will undergo radiation hardness tests so that the resistance to radiation of the scintillator, the optical fiber and the optical glue will be assessed. Once these features are defined, the calibration at higher dose rates will be repeated with a new GAGG detector.

For the reasons previously presented, the PS count rate was the only result considered for all the three data acquisitions with the 30 mm aperture collimator. With these measurements, in addition to verifying the linearity of the plastic fiber count rate as a function of the dose rate, we assessed any signal variations in the case of multiple consecutive irradiations at high dose rates. The values extracted from the first and the second data acquisitions are collected in Table 4.9. The third set of data was presented in Table 4.6 together with the results of the calibrations with the 4 mm and 10 mm collimators in which both the PS and GAGG fibers showed a reliable signal.

In Figure 4.16 the count rate of the PS during the whole calibration performed with the 30 mm aperture collimator is presented. The first data set

N°	IC signal [nA/cm^2]	PS counts/s	$\dot{D}$ [Gy/s]
1	8.87E+02	1.82E+06 ± 3.12E+03	47.41 ± 0.10
2	1.37E+03	2.77E+06 ± 3.90E+03	73.15 ± 0.16
3	1.68E+03	3.42E+06 ± 5.87E+03	89.97 ± 0.20
4	2.36E+03	4.83E+06 ± 8.40E+03	126.19 ± 0.27
5	2.86E+03	5.82E+06 ± 9.00E+03	152.95 ± 0.33
6	6.46E+03	1.29E+07 ± 1.70E+04	345.08 ± 0.75
1	2.39E+03	5.26E+06 ± 9.46E+03	127.77 ± 0.28
2	3.32E+03	7.21E+06 ± 8.84E+03	177.35 ± 0.38
3	4.84E+03	1.06E+07 ± 1.08E+04	258.54 ± 0.56
4	6.11E+03	1.32E+07 ± 1.19E+04	326.78 ± 0.71
5	7.56E+03	1.60E+07 ± 1.58E+04	403.97 ± 0.88

Table 4.9: Parameters extracted from the first two data acquisitions during the calibration of the fibers with the 30 mm aperture collimator. In this two sets of measurements the GAGG signal showed an unusual behaviour, therefore its count rate is not presented.

is colored in blue, the second one in orange and the third in green.
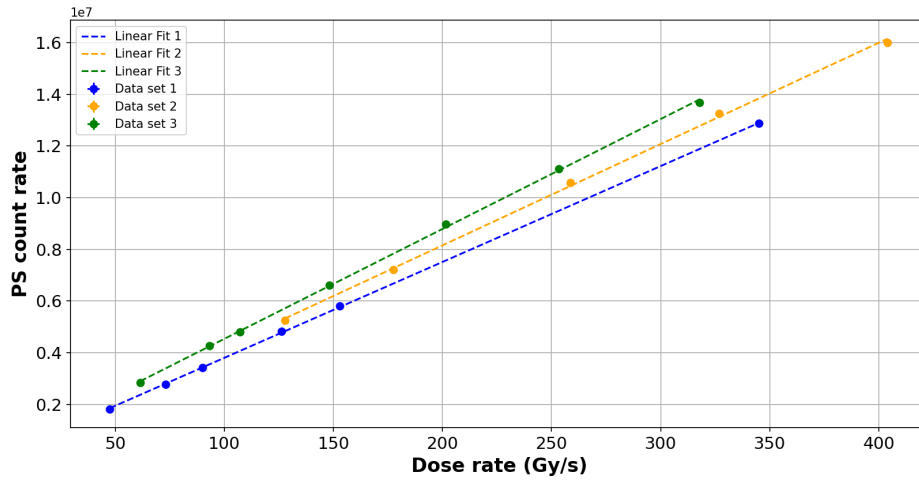
Figure 4.16: Linear fit of the PS count rates as a function of the dose rate for the three data acquisitions performed with the 30 mm aperture collimator. The error bars are smaller than the point size.

The plots in Figure 4.16 show a linear response of the fiber signal with the dose rate. Given the fact that the three measurements were performed

SET	Slope [Gy^{-1}]	Intercept [s^{-1}]	R^2
1 (blue)	3.71E+04 $\pm$ 1.95E+02	9.49E+04 $\pm$ 3.32E+04	0.9999
2 (yellow)	3.91E+04 $\pm$ 6.44E+02	3.18E+05 $\pm$ 1.79E+05	0.9992
3 (green)	4.25E+04 $\pm$ 3.89E+02	2.89E+05 $\pm$ 7.37E+04	0.9996

Table 4.10: Parameters resulting from the linear fit applied to the three sets of data of the PS count rate for the measurement with the 30 mm aperture.

using the same setup, the lines were expected to coincide. In this case however, three different lines have been obtained, described by the coefficients in Table 4.10.

The slope of the lines slightly increased in subsequent irradiations performed within the same dose rate range. The background signal, referring to the signal in the absence of the beam, was initially examined. This increase could not be attributed to the accumulation of background radiation due to the activation of the setup because the fiber signal in between beam pulses remained consistent throughout all the three irradiations. This is expected because most of the setup elements are built from natural aluminium, whose proton-induced reaction products in this energy range decay with a half life of the order of a few seconds or less.

Based on the current results, an explanation for the observed behavior of the plastic scintillator could not be determined. Many factors are known to influence the light output of the scintillator such as dose, dose rate, type of radiation, humidity and temperature [75]. Temperature is particularly difficult to control when irradiating within high dose rate ranges and can affect the response of the scintillator [76].

In order to find a cause for this behaviour, new plastic scintillators will be characterized to investigate the dependence of the signal on the previously mentioned factors and a radiation hardness and temperature test will be performed. For this purpose, a temperature measuring device for this specific application is currently under study.

The analysis of the data acquired during this dose rate study with the fibers demonstrates the difficulties related to adapting a 18 MeV proton beam medical cyclotron to deliver FLASH rates.

The need to fragment the experiment into multiple data acquisitions, due to the necessity of different setups for various dose rate ranges, can influence the reproducibility of the results. The use of different collimator apertures might change the geometry and uniformity of the beam, and the position of each element in the setup might vary slightly. A step forward in these measurements could involve the inclusion of a variable-size collimator that

can be remotely controlled to adjust the dimension of its aperture. This feature could enable us to perform a full dose rate characterization from conventional to flash regimes using a single setup.

Another improvement will be to use the GAGG scintillator at FLASH rates without attenuating the signal. The GAGG fiber was primarily chosen for this application due to its high light yield, from which a significant signal-to-noise ratio and excellent statistics derive. The SPAD was the limiting factor in this setup: the GAGG signal had to be attenuated, resulting in the loss of this important feature. To address this, a faster data acquisition system may be employed for future applications. One possibility could be to replace the SPAD with a fast PMT compatible with the GAGG fiber.

The behaviour of the fiber detectors and their features will be investigated and the possible aspects influencing their signal will be precisely defined and measured. With this knowledge, the characterization will be repeated and a reliable conversion of the count rates as a function of the dose rate will be established for our facility.

4.4   First cell irradiation experiments

The goal of the study performed in collaboration with the Institute of Anatomy of the University of Bern was to asses the survival of batches of cells irradiated with different radiation sources, including X-rays and protons.

For this project, three cell lines possessing different radiation sensitivity were chosen:

- HaCat: human skin, radiosensitive;

- B16-F10: mouse melanoma, radioresistant;

- HTB-140: human melanoma, radioresistant.

All the three cell lines were given identical doses, maintaining a consistent dose rate. To achieve comparable results, the dose rate was set to a similar value to the one used in the irradiations performed at the Institute of Anatomy with X-rays, namely 0.03 Gy/s.

For each dose, six flasks were irradiated one at a time in order to collect statistically valid data. The flasks were positioned inside customized holders on the remotely movable stage. Once the position of each target was precisely defined, we had the possibility to move the holder and center the beam with each of the flasks from outside the bunker. Therefore, the irradiations were performed consecutively without the need to enter the BTL bunker after each exposure.

The first challenge associated with using conventional dose rates was the relatively short survival time of cells outside the incubation system. In order not to compromise the survival of cells, the flasks must be kept outside the incubator for no more than 15 minutes. To address this issue, all the irradiations, except the one with the lowest dose, were split into two separate runs of three flasks each. This division was necessary because of the fixed dose rate, that caused the time of the full procedure for these points to extend over the limit of 15 minutes.

The LabView program used to read the current from the collimator device and the ionization chamber was modified by incorporating a dose rate calculator. The ionization chamber current was read in real time and normalized to the area of the beam spot. Then, thanks to the equation extracted from the fit in Figure 4.8, this current density was converted into the dose rate of the irradiation. This specific equation was used because it simulates the dose rate in case of cell irradiations, as the characterization was performed with the same setup and with the inclusion of a flask before the Gafchromic film for the dose readout.
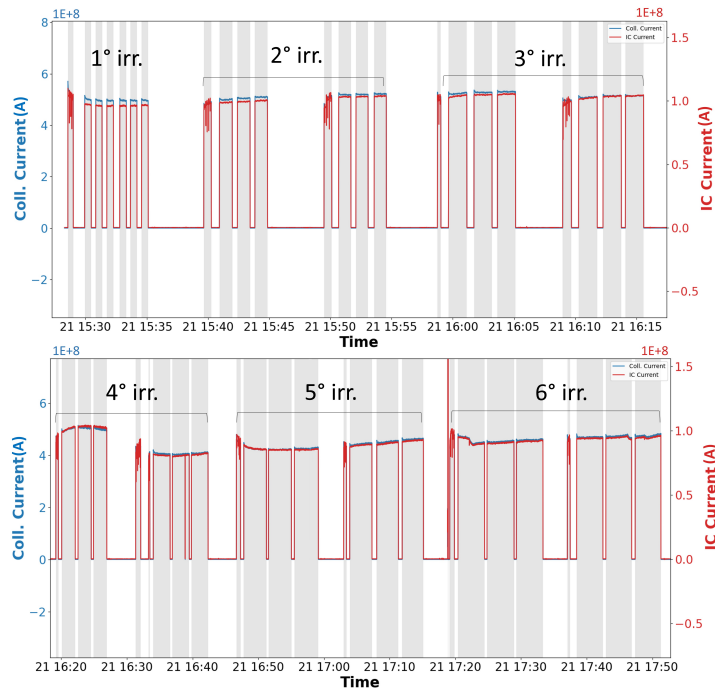
Figure 4.17: Distribution of the pinhole collimator current (in blue) and IC current (in red) over time throughout the cell irradiation. The gray bands correspond to beam on. Prior to each set of irradiations, the beam position was checked with the UniBEam, therefore an additional peak precedes each run.

The accumulated dose was also determined in real time by multiplying the dose rate by the time window from the beginning of each irradiation.

The plot in Figure 4.17 shows the current on both the collimator and the ionization chamber during the cell irradiations.

The signal of both devices is constant around a certain level for the entire set of irradiations, demonstrating that the dose rate at which the facility is working is stable. The gray bands, which indicate the intervals in which the beam is on, extend as the delivered dose increases demonstrating the longer irradiation time.

After the exposure, the cells are capable of proliferating depending on the damage caused by the irradiation. The survival curve is measured in terms of the capacity to create a new cell colony. The colonies created by the irradiated cells are measured by the Institute of Anatomy using the Clonogenic Cell Survival Assay techniques [31]. The analysis was performed one week after the irradiation to let the cells grow.
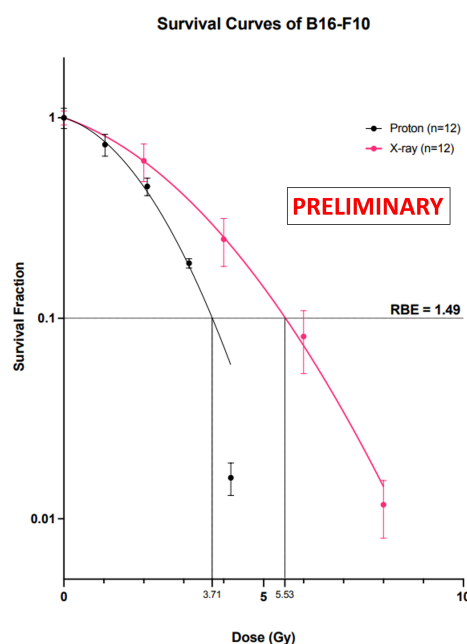
Figure 4.18: Preliminary survival curve resulting from the irradiation of cells at the Bern Medical Cyclotron and at the photon irradiation facility at the Institute of Anatomy [77]. The black curve represents the impact of protons, showing a greater effect on the cell survival capability compared to the red curve, which corresponds to photons.

A preliminary analysis of the cell lines irradiated during this thesis project provided the cell survival curve presented in Figure 4.18 [77].

The experimental data points presented in Figure 4.18 were acquired irradiating the cells with protons to the doses of 1 Gy, 2 Gy, 3 Gy and 4 Gy. Two more data sets, not included in this preliminary result, have been acquired at 6 Gy and 8 Gy.

The figure demonstrates a smaller capability to reproduce for cells irradiated with protons, as expected. The batches that were irradiated to the same doses using a similar dose rate, have an enhanced probability of growing a colony if irradiated with photons rather than with protons.

This preliminary result confirms the trend expected for photons and protons. As defined in Section 1.1, the second radiation source has a higher LET. Therefore, it is capable of depositing more energy in the cell layer, causing a larger damage.

This very promising outcome proves the capability of the Bern medical cyclotron and the BTL to perform pre-clinical studies on cells using protons. The upcoming phase of the project involves adapting the apparatus for cell irradiations at FLASH dose rates. This future step requires the signal of the new detection system based on scintillating fibers to be further studied and correlated to the dose rate of the facility. Once this will be done, the cell survival curve obtained from the same batches of cells using photons and protons at FLASH dose rates will be compared to the one at conventional dose rates. This analysis will give us the opportunity to evaluate the effect of FLASH regime irradiations on cells.

Conclusions and outlook

This master thesis work is focused on an original project aimed at establishing a cell irradiation beamline for pre-clinical studies at the Bern medical cyclotron. These developments, performed in collaboration with the University of Bern Institute of Anatomy, aim at irradiating batches of cells with different radiosensitivity using both conventional and FLASH dose rates. This work allowed extracting the survival curve of some specific cells for the first time at the cyclotron laboratory in Bern. This preliminary result represents the validation of all the software and hardware developments as well as of the whole procedure.

The facility at the Bern University Hospital comprises a medical cyclotron producing 18 MeV proton beams, regularly used for radioisotope production. Thanks to a Beam Transfer Line, connected directly to the cyclotron, the proton beam can be transferred to a separate bunker and used for research activities. While for the radioisotope production the cyclotron typically operates at high beam currents (larger than $10\,\mu A$), the accelerator operates with typical beam currents in the nA range for several scientific applications. This feature is fundamental since stable beams in the nA range are crucial to perform cell irradiations.

This project started with a study of the appropriate setup for irradiation at conventional dose rates that could ensure a maximum beam energy and uniformity at the cell level. The optimized setup resulted in a beam uniformity of 9.26(07)% and the relative dose at a radius of 20 mm from the center of the beam, representative of the boundaries of the flask on which the cells are plated, was evaluated to be 87% of the initial value. These two results meet the requirements for cell irradiations.

The beam energy at the cell position was simulated using the LISE++ code and resulted in 7.69 ± 0.50 MeV with a corresponding stopping power of 56.34 MeV·cm^2/g, calculated using Pstar.

Another crucial requirement for performing pre-clinical studies at the Bern medical cyclotron was the development of a robust calculation method to determine the precise dose delivered to each cell sample. To achieve this goal,

the dose rate of the facility was characterized at conventional and FLASH dose rates with a ionization chamber, using Gafchromic films for the dose readout.

The batches of Gafchromic EBT-3 and HD-V2 films used for this purpose were properly calibrated during this project at different facilities.

With these measurements, the ionization chamber was proved to be able to accurately record signals within the dose rates range from 0.02 Gy/s to 88.29 Gy/s. The experimental points were adapted to a linear fit and the conversion of the ionization chamber current density to dose rate was established.

The three cell lines (HaCat, B16-F10 and HTB-140) were irradiated with this novel setup. Preliminary results from the analysis performed by the Institute of Anatomy indicate that irradiation with protons induces more damage compared to similar irradiation performed with a photon beam. This conclusion is in alignment with what reported in literature and confirms the accurate delivery of the dose by the proton beam.

Together with the cell irradiation work, a novel dosimeter for FLASH irradiation was tested at our facility. The detector is based on a scintillator connected to an optical fiber. In our case a plastic scintillator based detector and a GAGG-based detector were tested. The fibers response with the dose rates was found to be linear in several irradiations performed from the conventional to the FLASH regime. However the fibers exhibited a different behavior for each set of irradiations, making the overall interpretation of the experiment challenging. Since the output of the scintillator is known to be influenced by a multitude of parameters, the fibers signal will be characterized in our laboratory in future experiments. New batches of the innovative detection systems will undergo radiation hardness and temperature tests to assess any potential damage caused by these variables to the detector.

The future developments of this work include performing irradiations in the FLASH regime to investigate the "FLASH effect". Additionally, these experiments will investigate the use of the novel scintillator-based dosimeter in pre-clinical applications.

This master thesis project has contributed to establish the basis of a novel facility to perform in-vitro pre-clinical studies with a medical cyclotron. The obtained results suggest the possibility to adapt the facility for pre-clinical in-vivo studies involving animals. Although the energy of the proton beam is limited to 18 MeV, it would be possible to irradiate tumors implanted in the ears of mice.

This project has proven that it is possible to integrate pre-clinical proton therapy research in the framework of a facility based on a medical cyclotron for the production of radioisotopes.

List of Acronyms

AEC Albert Einstein Center for fundamental physics

BTL Beam Transport Line

CNR National Research Council

EBRT External Beam Radiation Therapy

EBT External Beam Therapy

FOV Field of View

GAGG Gadolinium Aluminum Gallium Garnet

GMP Good Manufacturing Practice

IC Ionization Chamber

Inselspital Bern University Hospital

IRT Internal Radiation Therapy

ISOF Institute for Organic Synthesis and Photoreactivity

LET Linear Energy Transfer

LHEP Laboratory of High Energy Physics

linac linear accelerator

MAPP Medical Application of Particle Physics

MCPC Multi Channel Pulse Counting system

METAS Swiss Federal Institute of Metrology

MU Monitor Unit

NTCP Normal Tissue Complication Probability

OSLD Optically Stimulated Luminescent Dosimeter

PET Positron Emission Tomography

PMT PhotoMultiplier Tube

PROOF PRecision dOsimetry in FLASH radiotherapy with Optical Fibers

PS Plastic Scintillator

PV Pixel Value

RBE Relative Biological Effectiveness

RF RadioFrequency

ROI Region Of Interest

RT Radiation Therapy

SPAD Single Photon Avalanche Diode

SSD Source-Surface Distance

TCP Tumor Control Probability

TIFF Tag Image File Format

TLD ThermoLuminescent Dosimeter

TRT Targeted Radionuclide Therapy

List of Figures

List of Tables

Bibliography

[1] AIOM – Associazione Italiana di Oncologia Medica. *I numeri del cancro in Italia*. URL: https://www.aiom.it/i-numeri-del-cancro-in-italia/.

[2] A. Urruticoechea et al. "Recent advances in cancer therapy: an overview". In: *Current pharmaceutical design* 16.1 (2010), pp. 3–10.

[3] M. Goitein. *Radiation Oncology: A Physicist's-Eye View*. Biological and Medical Physics, Biomedical Engineering. Springer New York, 2007. ISBN: 9780387726458.

[4] D. A. Jaffray and M. K. Gospodarowicz. "Radiation therapy for cancer". In: *Cancer: disease control priorities* 3 (2015), pp. 239–248.

[5] R. Baskar et al. "Cancer and radiation therapy: current advances and future directions". In: *International journal of medical sciences* 9.3 (2012), p. 193.

[6] G. Sgouros et al. "Radiopharmaceutical therapy in cancer: clinical advances and challenges". In: *Nature reviews Drug discovery* 19.9 (2020), pp. 589–608.

[7] M. Sadeghi, M. Enferadi, and A. Shirazi. "External and internal radiation therapy: past and future directions". In: *Journal of cancer research and therapeutics* 6.3 (2010), pp. 239–248.

[8] T. De Laney and H. Kooy. *Proton and Charged Particle Radiotherapy*. LWW medical book collection. Lippincott Williams & Wilkins, 2008. ISBN: 9780781765527.

[9] A. Kaiser et al. "Proton therapy delivery and its clinical application in select solid tumor malignancies". In: *JoVE (Journal of Visualized Experiments)* 144 (2019), e58372.

[10] S. B. Jia et al. "Designing a range modulator wheel to spread-out the Bragg peak for a passive proton therapy facility". In: *Nuclear Instruments and Methods in Physics Research Section A: Accelerators, Spectrometers, Detectors and Associated Equipment* 806 (2016), pp. 101–108. ISSN: 0168-9002. DOI: `https://doi.org/10.1016/j.nima.2015.10.006`.

[11] S. Yajnik. *Proton beam therapy: how protons are revolutionizing cancer treatment.* Springer Science & Business Media, 2012.

[12] S. Yan et al. "Global democratisation of proton radiotherapy". In: *The Lancet Oncology* 24.6 (2023), e245–e254.

[13] A. Degiovanni and U. Amaldi. "History of hadron therapy accelerators". In: *Physica medica* 31.4 (2015), pp. 322–332.

[14] F. M. Khan. *The physics of radiation therapy.* Lippincott Williams & Wilkins, 2010.

[15] OncologyMedicalPhysics.com. *Cyclotrons.* URL: `https://oncologymedicalphysics.com/cyclotron-particle-accelerators/`.

[16] B. Lin et al. "FLASH radiotherapy: history and future". In: *Frontiers in oncology* (2021), p. 1890.

[17] A. A. Friedl et al. "Radiobiology of the FLASH effect". In: *Medical Physics* 49.3 (2022), pp. 1993–2013.

[18] M. C. Vozenin, J. Bourhis, and M. Durante. "Towards clinical translation of FLASH radiotherapy". In: *Nature Reviews Clinical Oncology* 19.12 (2022), pp. 791–803.

[19] D. Dewey and J. Boag. "Modification of the oxygen effect when bacteria are given large pulses of radiation". In: *Nature* 183.4673 (1959), pp. 1450–1451.

[20] V. Favaudon et al. "Ultrahigh dose-rate FLASH irradiation increases the differential response between normal and tumor tissue in mice". In: *Science translational medicine* 6.245 (2014), 245ra93–245ra93.

[21] J. Bourhis et al. "Treatment of a first patient with FLASH-radiotherapy". In: *Radiotherapy and oncology* 139 (2019), pp. 18–22.

[22] F. Romano et al. "Ultra-high dose rate dosimetry: Challenges and opportunities for FLASH radiation therapy". In: *Medical Physics* 49 (Apr. 2022). DOI: `10.1002/mp.15649`.

[23] V. Vanreusel et al. "Point scintillator dosimetry in ultra-high dose rate electron "FLASH" radiation therapy: A first characterization". In: *Physica Medica* 103 (2022), pp. 127–137.

[24] IAEA. *Absorbed Dose Determination in External Beam Radiotherapy.* Technical Reports Series 398. Vienna: INTERNATIONAL ATOMIC ENERGY AGENCY, 2001. ISBN: 92-0-102200-X. URL: `https://www.iaea.org/publications/5954/absorbed-dose-determination-in-external-beam-radiotherapy`.

[25] A. Darafsheh. *Radiation Therapy Dosimetry: A Practical Handbook.* CRC Press, 2021.

[26] F. Gómez et al. "Development of an ultra-thin parallel plate ionization chamber for dosimetry in FLASH radiotherapy". In: *Medical Physics* 49.7 (Apr. 2022), 4705–4714. ISSN: 2473-4209. DOI: `10.1002/mp.15668`. URL: `http://dx.doi.org/10.1002/mp.15668`.

[27] G. Blasse. "Scintillator materials". In: *Chemistry of Materials* 6.9 (1994), pp. 1465–1475.

[28] Y. Hu et al. "Characterization of fiber radiation dosimeters with different embedded scintillator materials for radiotherapy applications". In: *Sensors and Actuators A: Physical* 269 (2018), pp. 188–195.

[29] P. Casolaro. "Fiber-coupled GAGG scintillators for real-time small-field dosimetry in FLASH proton therapy". In: *IEEE TRANSACTIONS ON NUCLEAR SCIENCE* (). DOI: `unpublished`.

[30] P. Casolaro et al. "Time-Resolved Proton Beam Dosimetry for Ultra-High Dose-Rate Cancer Therapy (FLASH)". In: *Proceedings of the 11th International Beam Instrumentation Conference* IBIC2022 (2022), Poland. DOI: `10.18429/JACOW-IBIC2022-WE3C2`. URL: `https://jacow.org/ibic2022/doi/JACoW-IBIC2022-WE3C2.html`.

[31] A. Munshi, M. Hobbs, and R. E. Meyn. "Clonogenic cell survival assay". In: *Chemosensitivity: Volume 1 In Vitro Assays* (2005), pp. 21–28.

[32] SWAN Isotopen AG. *SWAN Isotopen AG: commercial radiopharmaceuticals production facility on the campus of the University Hospital Bern.* URL: `https://www.swanisotopen.ch/en/`.

[33] Laboratory for High Energy Physics (LHEP). *University of Bern Albert Einstein Center for Fundamental Physics - LHEP.* URL: `https://www.lhep.unibe.ch/`.

[34] J. Anders et al. "A facility for radiation hardness studies based on a medical cyclotron". In: *Journal of Instrumentation* 17.04 (Apr. 2022), P04021. DOI: `10.1088/1748-0221/17/04/P04021`. URL: `https://dx.doi.org/10.1088/1748-0221/17/04/P04021`.

[35] G. Dellepiane et al. "New methods for theranostic radioisotope pro-
      duction with solid targets at the Bern medical cyclotron". In: *EPJ Web
      Conf.* 261 (2022), p. 05006. DOI: 10.1051/epjconf/202226105006.
      URL: https://doi.org/10.1051/epjconf/202226105006.

[36] S. Braccini. *Particle Accelerators and Detectors for medical Diagnostics
      and Therapy*. 2016. arXiv: 1601.06820 [physics.med-ph].

[37] L. Campajola et al. "Measurement of the proton beam energy of a
      medical cyclotron based on Rutherford Back-scattering Analysis". In:
      *Nuclear Instruments and Methods in Physics Research Section B: Beam
      Interactions with Materials and Atoms* 440 (2019), pp. 114–117. ISSN:
      0168-583X. DOI: https://doi.org/10.1016/j.nimb.2018.12.017.
      URL: https://www.sciencedirect.com/science/article/pii/S01
      68583X18307274.

[38] P. Häffner et al. "Study of the Extracted Beam Energy as a Function of
      Operational Parameters of a Medical Cyclotron". In: *Instruments* 3.4
      (2019). ISSN: 2410-390X. DOI: 10.3390/instruments3040063. URL:
      https://www.mdpi.com/2410-390X/3/4/63.

[39] K. P. Nesteruk et al. "Measurement of the Beam Energy Distribution of
      a Medical Cyclotron with a Multi-Leaf Faraday Cup". In: *Instruments*
      3.1 (2019). ISSN: 2410-390X. DOI: 10.3390/instruments3010004. URL:
      https://www.mdpi.com/2410-390X/3/1/4.

[40] S Braccini et al. "A beam monitor detector based on doped silica and
      optical fibres". In: *Journal of Instrumentation* 7.02 (Feb. 2012), T02001.
      DOI: 10.1088/1748-0221/7/02/T02001. URL: https://dx.doi.org
      /10.1088/1748-0221/7/02/T02001.

[41] G. Dellepiane. "Novel Radionuclides for Theranostics at the Bern Medi-
      cal Cyclotron." Doctoral thesis. Albert Einstein Center for Fundamen-
      tal Physics Laboratory for High Energy Physics University of Bern.
      2023.

[42] PTW dosimetry Freiburg. *Monitor Ionization Chamber 786*. URL: htt
      ps://www.ptwdosimetry.com/en/products/monitor-ionization-c
      hambers-34014-786.

[43] Epic Crystal Co. *PS Crystal*. URL: https://www.epic-crystal.com
      /data/upload/20230823/64e582d58cbbb.pdf.

[44] Epic Crystal Co. *GAGG(Ce) Crystal*. URL: https://www.epic-crys
      tal.com/scintillation-crystals/gaggce-crystal.html.

[45] S. Yamamoto et al. "Development of an Ultrahigh Resolution Block Detector Based on 0.4 mm Pixel Ce:GAGG Scintillators and a Silicon Photomultiplier Array". In: *IEEE Transactions on Nuclear Science* 60.6 (2013), pp. 4582–4587. DOI: 10.1109/TNS.2013.2282294.

[46] NORLAND PRODUCTS INCORPORATED. *Norland Optical Adhesive 68*. URL: https://www.norlandprod.com/literature/68tds.pdf.

[47] NORLAND PRODUCTS INCORPORATED. *Norland Optical Adhesive 63*. URL: https://www.norlandprod.com/literature/63tds.pdf.

[48] ID QUANTIQUE SA. *ID100 Visible Single Photon Detector*. Available at https://marketing.idquantique.com/acton/attachment/11868/f-0236/1/-/-/-/-/ID100_Brochure.pdf. Rue Eugène-Marziano 25 1227 Acacias/Geneva Switzerland, 2023.

[49] Vertilon Corporation. *MCPC618 Multichannel Pulse Counting System*. URL: https://www.vertilon.com/pdf/PS2720.pdf.

[50] Analog Devices, Inc. (ADI). *PD-x-1021 Stepper Motor*. URL: https://www.trinamic.com/products/drives/details/pd28-x-1021/.

[51] LISE++ group. *LISE++: Rare Isotope Beam Production*. URL: https://lise.nscl.msu.edu/documentation.html.

[52] NIST National Institute of Standards and Technology. *Pstar*. URL: https://physics.nist.gov/PhysRefData/Star/Text/PSTAR.html.

[53] H. Bethe. "Zur Theorie des Durchgangs schneller Korpuskularstrahlen durch Materie". In: *Annalen der Physik* 397.3 (1930), pp. 325–400. DOI: https://doi.org/10.1002/andp.19303970303. eprint: https://onlinelibrary.wiley.com/doi/pdf/10.1002/andp.19303970303. URL: https://onlinelibrary.wiley.com/doi/abs/10.1002/andp.19303970303.

[54] J. F. Ziegler. *SRIM - The Stopping and Range of Ions in Matter*. URL: http://www.srim.org/.

[55] National Institutes of Health. *Image Processing and Analisys in Java*. URL: https://imagej.net/ij/index.html.

[56] Ashland Advanced Materials. *GAFCHROMIC DOSIMETRY FILMS*. URL: http://www.gafchromic.com/gafchromic-film/index.asp.

[57] S. Devic. "Radiochromic film dosimetry: Past, present, and future". In: *Physica medica : PM : an international journal devoted to the applications of physics to medicine and biology : official journal of the Italian Association of Biomedical Physics (AIFB)* 27 (Nov. 2010), pp. 122–34. DOI: `10.1016/j.ejmp.2010.10.001`.

[58] P. Casolaro. "Radiochromic Films for the Two-Dimensional Dose Distribution Assessment". In: *Applied Sciences* 11.5 (Feb. 2021), p. 2132. DOI: `10.3390/app11052132`. URL: `https://doi.org/10.3390/app11052132`.

[59] K. Keller et al. "Photography". In: *Ullmann's Encyclopedia of Industrial Chemistry*. John Wiley and Sons, Ltd, 2000. ISBN: 9783527306732. DOI: `https://doi.org/10.1002/14356007.a20_001`. eprint: `https://onlinelibrary.wiley.com/doi/pdf/10.1002/14356007.a20_001`. URL: `https://onlinelibrary.wiley.com/doi/abs/10.1002/14356007.a20_001`.

[60] S. Devic, N. Tomic, and D. Lewis. "Reference radiochromic film dosimetry: Review of technical aspects". In: *Physica Medica* 32.4 (Apr. 2016), pp. 541–556. DOI: `10.1016/j.ejmp.2016.02.008`. URL: `https://doi.org/10.1016/j.ejmp.2016.02.008`.

[61] S. Karthikeyan and E. Samuel. "Water equivalent radiological properties of Gafchromic external beam therapy and external beam therapy 2 film dosimeters". In: *Journal of Cancer Research and Therapeutics* 15 (Jan. 2018). DOI: `10.4103/jcrt.JCRT_965_16`.

[62] Ashland Advanced Materials. *EBT-3 FILM SPECIFICATION AND USER GUIDE*. Available at `http://www.gafchromic.com/documents/EBT3_Specifications.pdf`. Wilmington, 8145 Blazer Dr, United States, 2023.

[63] Ashland Advanced Materials. *HD-V2 FILM SPECIFICATION AND USER GUIDE*. Available at `http://www.gafchromic.com/documents/EBT3_Specifications.pdf`. Wilmington, 8145 Blazer Dr, United States, 2023.

[64] V. C. Borca et al. "Dosimetric characterization and use of GAFCHROMIC EBT3 film for IMRT dose verification". In: *Journal of Applied Clinical Medical Physics* 14.2 (Mar. 2013), pp. 158–171. DOI: `10.1120/jacmp.v14i2.4111`. URL: `https://doi.org/10.1120/jacmp.v14i2.4111`.

[65] M. J. Butson et al. "Polarization effects on a high-sensitivity radiochromic film". In: *Phys. Med. Biol.* 48.15 (Aug. 2003), N207–11.

[66] IMAGEJ. *Image Menu ImageJ*. URL: `https://imagej.net/ij/docs/menus/image.html`.

[67] L. Campajola, P. Casolaro, and F. D. Capua. "Absolute dose calibration of EBT3 Gafchromic films". In: *Journal of Instrumentation* 12.08 (Aug. 2017), P08015–P08015. DOI: `10.1088/1748-0221/12/08/p08015`. URL: `https://doi.org/10.1088/1748-0221/12/08/p08015`.

[68] H. Lee. *Introduction to Color Imaging Science*. Cambridge University Press, 2005. ISBN: 9781139444552. URL: `https://books.google.ch/books?id=rN3kOMOPMmEC`.

[69] Varian Medical Systems, Inc., Palo Alto, California. *TrueBeam | Varian*. URL: `https://www.varian.com/products/radiotherapy/treatment-delivery/truebeam`.

[70] PTW Freiburg. *PTW THE DOSIMETRY COMPANY*. URL: `https://www.ptwdosimetry.com/en/`.

[71] METAS. *The Federal Institute of Metrology (METAS)*. URL: `https://www.metas.ch/metas/en/home/metas/institut.html`.

[72] ISOF CNR. *Institute for Organic Synthesis and Photoreactivity, National Research Council of Italy*. URL: `https://www.isof.cnr.it/`.

[73] V. Alenkov et al. "Irradiation studies of a multi-doped Gd3Al2Ga3O12 scintillator". In: *Nuclear Instruments and Methods in Physics Research Section A: Accelerators, Spectrometers, Detectors and Associated Equipment* 916 (2019), pp. 226–229. ISSN: 0168-9002. DOI: `https://doi.org/10.1016/j.nima.2018.11.101`.

[74] M. Yoneyama et al. "Evaluation of GAGG:Ce scintillators for future space applications". In: *Journal of Instrumentation* 13.02 (Feb. 2018), P02023. DOI: `10.1088/1748-0221/13/02/P02023`.

[75] Y. N. Kharzheev. "Radiation hardness of scintillation detectors based on organic plastic scintillators and optical fibers". In: *Physics of Particles and Nuclei* 50 (2019), pp. 42–76.

[76] K. Johnson and H. Whitaker. "Temperature treatment of plastic scintillator affects radiation hardness". In: *Nuclear Instruments and Methods in Physics Research Section A: Accelerators, Spectrometers, Detectors and Associated Equipment* 301.2 (1991), pp. 372–375.

[77] G. Jan and C. Fernandez-Palomo. *Cell survival of B16-F10 mouse melanoma to protons and x-rays*. Version 2023.11.20. Jan. 2024. DOI: `10.5281/zenodo.10478639`. URL: `https://doi.org/10.5281/zenodo.10478639`.